Final Report

# Numerical Investigation of 3-D Separation: DNS, LES and URANS

Office of Naval Research
Contract number: N00014-07-1-0401
Program manager: Dr. Ronald Joslin

H.F. Fasel, A. Gross, R. Jacobi, A. Kremheller
University of Arizona

May 2010

20100518007

| REPORT DOCUMENTATION PAGE | *Form Approved*<br>*OMB No. 0704-0188* |
|---|---|

The public reporting burden for this collection of information is estimated to average 1 hour per response, including the time for reviewing instructions, searching existing data sources, gathering and maintaining the data needed, and completing and reviewing the collection of information. Send comments regarding this burden estimate or any other aspect of this collection of information, including suggestions for reducing the burden, to Department of Defense, Washington Headquarters Services, Directorate for Information Operations and Reports (0704-0188), 1215 Jefferson Davis Highway, Suite 1204, Arlington, VA 22202-4302. Respondents should be aware that notwithstanding any other provision of law, no person shall be subject to any penalty for failing to comply with a collection of information if it does not display a currently valid OMB control number.
**PLEASE DO NOT RETURN YOUR FORM TO THE ABOVE ADDRESS.**

**1. REPORT DATE** *(DD-MM-YYYY)* 05/14/2010

**2. REPORT TYPE** Final Technical Report

**3. DATES COVERED** *(From - To)* 12/11/2006 - 12/31/2009

**4. TITLE AND SUBTITLE**
Numerical Investigation of 3-D Separation: DNS, LES and URANS

**5a. CONTRACT NUMBER** N00014-07-1-0401

**5b. GRANT NUMBER** N00014-07-1-0401

**5c. PROGRAM ELEMENT NUMBER**

**6. AUTHOR(S)**
H.F. Fasel, A. Gross, R. Jacobi, A. Kremheller

**5d. PROJECT NUMBER**

**5e. TASK NUMBER**

**5f. WORK UNIT NUMBER**

**7. PERFORMING ORGANIZATION NAME(S) AND ADDRESS(ES)**
Department of Aerospace and Mechanical Engineering
University of Arizona
1130 N Mountain Ave
Tucson, AZ 85716

**8. PERFORMING ORGANIZATION REPORT NUMBER**

**9. SPONSORING/MONITORING AGENCY NAME(S) AND ADDRESS(ES)**
Office of Naval Research
875 North Randolph Street
Arlington, VA 22203-1995

**10. SPONSOR/MONITOR'S ACRONYM(S)** ONR

**11. SPONSOR/MONITOR'S REPORT NUMBER(S)**

**12. DISTRIBUTION/AVAILABILITY STATEMENT**

Approved for Public release; distribution is Unlimited.

**13. SUPPLEMENTARY NOTES**

**14. ABSTRACT**

For Navy relevant geometries, separation of wall bounded flows is a highly complex phenomenon. The combination of three-dimensionality and unsteadiness results in a highly complex time-dependent topology of the separated region. In a combined numerical/experimental effort we investigated laminar separation bubbles in external flows. We employed highly-resolved direct numerical simulations to obtain a deeper understanding of the various physical mechanism governing separation, transition, and reattachment. We also carried out and hybrid RANS/LES simulations for a turbulent square-duct and the Stanford University asymmetric diffuser.

**15. SUBJECT TERMS**

| **16. SECURITY CLASSIFICATION OF:** | | | **17. LIMITATION OF ABSTRACT** | **18. NUMBER OF PAGES** | **19a. NAME OF RESPONSIBLE PERSON** |
|---|---|---|---|---|---|
| **a. REPORT** | **b. ABSTRACT** | **c. THIS PAGE** | | | Prof. Hermann F. Fasel |
| | | | | | **19b. TELEPHONE NUMBER** *(Include area code)* |
| U | U | U | UU | 76 | (520) 481-0819 |

# Abstract

For Navy relevant geometries, separation of wall bounded flows is a highly complex phenomenon. Because of the relatively high Reynolds numbers involved, separation is always associated with considerable unsteadiness. This unsteadiness is caused by large coherent structures that are a consequence of hydrodynamic instability mechanisms of the mean flow. In addition, due to the shape of underwater vehicles (submarines, torpedoes, low aspect ratio lifting or control surfaces) the separation is three-dimensional (3-D). The combination of three-dimensionality and unsteadiness results in a highly complex time-dependent topology of the separated region. In a combined numerical/experimental effort we investigated laminar separation bubbles in external flows. For the simulations we employed highly-resolved direct numerical simulations (DNS) to obtain a deeper understanding of the various physical mechanism governing separation, transition, and reattachment of 3-D bubbles. Ultimately, such understanding may pave the way for the development of effective and efficient strategies for preventing separation for practical applications. We also evaluated hybrid turbulence models for high Reynolds number flows. In particular, we carried out DNS, RANS, and hybrid simulations of a turbulent square-duct flow. Based on these simulations we decided on two hybrid strategies for simulating the asymmetric diffuser experiments that were conducted at Stanford University by J. Eaton and co-workers.

## TABLE OF CONTENTS

1. INTRODUCTION. ....................3

2. SCOPE OF INVESTIGATIONS ....................6
  2.1 Geometry 1: Axisymmetric Displacement Body over Flat Plate ....................7
  2.2 Geometry 2: Stanford Asymmetric Diffuser ....................7
  2.3 Geometry 3: Square-Duct. ....................8

3. COMPUTATIONAL AND EXPERIMENTAL APPROACH ....................9
  3.1 Computational Methods ....................9
    3.1.1 Method 1: Higher-Order-Accurate Incompressible Finite Difference Code ....................9
      3.1.1.1 Governing Equations ....................9
      3.1.1.2 Discretization ....................9
      3.1.1.3 Computational Setup ....................10
      3.1.1.4 Disturbance Generation ....................11
    3.1.2 Method 2: Higher-Order-Accurate Compressible Multi-Domain Finite Volume Code ....................11
      3.1.2.1 Governing Equations ....................11
      3.1.2.2 Discretization ....................14
      3.1.2.3 Inflow and Outflow Conditions ....................15
      3.1.2.4 Non-Dimensionalization ....................15
    3.1.3 Post-Processing Tools ....................16
      3.1.3.1 Vortex Identification ....................16
      3.1.3.2 Auto-Correlation ....................16
      3.1.3.3 Energy Spectrum ....................16
  3.2 Experimental Facility ....................18
      3.2.1 Water Tunnel ....................18
      3.2.2 Flow Diagnostics ....................19

4. SEPARATION BUBBLE: DIRECT NUMERICAL SIMULATIONS ....................21
  4.1 Precursor Calculations ....................21
  4.2 Simulation Setup ....................22
  4.3 Results ....................23
    4.3.1 Effect of Domain Width ....................23
    4.3.2 Effect of Displacement Body Distance from Flat Plate ....................25
    4.3.3 Effect of Reynolds Number ....................29
    4.3.4 Flow Topology ....................33
    4.3.5 Unsteady Separation Phenomena ....................35
    4.3.6 Comparison to Two-Dimensional Separation Bubbles ....................39
    4.3.7 Comparison to Flow over Hemisphere-Cylinder ....................39

5. SEPARATION BUBBLE: WATER TUNNEL EXPERIMENTS ....................41
  5.1 Experimental Setup ....................41
    5.1.1 Exploratory Experiments ....................41
    5.1.2 Axisymmetric Displacement Body ....................42
    5.1.3 Flat Plate ....................43
  5.2 Results from Dye Flow Visualization ....................43
  5.3 PIV Measurements ....................46

6. SQUARE-DUCT FLOW SIMULATIONS ........ 49
  6.1 Computational Grid ........ 49
  6.2 Domain Length ........ 50
  6.3 Direct Numerical Simulation (DNS) ........ 51
  6.4 Reynolds-Averaged Navier-Stokes (RANS) Calculations ........ 54
  6.5 Hybrid RANS/LES Simulations ........ 56
  6.6 Rectangular Duct Flow ........ 63

7. DIFFUSER FLOW SIMULATIONS ........ 65
  7.1 Computational Grid ........ 65
  7.2 Simulation Results ........ 65

8. SUMMARY AND CONCLUSIONS ........ 71
  8.1 3-D Separation Bubble on Flat Plate: Simulations and Experiments ........ 71
  8.2 Simulations of Square-Duct Flow and Asymmetric Diffuser ........ 71

REFERENCES ........ 73

PUBLICATIONS RESULTING FROM GRANT ........ 76

# 1. INTRODUCTION

Separation for Navy relevant geometries (submarines, torpedoes, fins, low aspect ratio lifting or control surfaces) is often three-dimensional (3-D) and associated with considerable unsteadiness. Strong unsteadiness can be introduced by coherent flow structures which can be characterized as areas of organized fluid motion within a turbulent flow. These structures are a consequence of hydrodynamic instabilities and originate in the separated shear layer. They impact the separation and reattachment behavior and thereby affect size and shape of the separated region or separation bubble. This can cause considerable unsteady hydrodynamic loads and ultimately a change in the lift and drag characteristics of the vehicle. An improved understanding of the flow physics governing 3-D separation in general and the dynamics of such structures in particular is desirable as it may lead to techniques that allow for the prediction of unsteady loads which would in turn enable the development of geometries with more favorable hydrodynamic properties. An improved understanding may also point out possibilities for novel devices or strategies that may help prevent or control separation by influencing the unsteady flow structures.

The topology of 3-D separation bubbles can be analyzed by considering the limiting skin friction lines [Tobak and Peake, 1982]. Saddle points are points where two skin friction lines cross each other. Points to which an infinite number of skin friction lines converge are known as nodes and foci. Similar structures can be identified in wall normal planes, such as the symmetry plane. Three-dimensional flow separation cannot be universally characterized by the vanishing of wall shear. Rather, as Lighthill [1963] pointed out, it is characterized by the convergence of the limiting skin friction lines onto one separation skin friction line. The dividing stream-surface originating from this line is called the separation stream-surface. Focal points, around which skin friction lines spiral, are the roots of wall-normal vortices, often referred to as "horn vortices

Because of the 3-D nature of the flow the underlying physics are very complex. For separated flows hydrodynamic instability mechanisms of the mean flow can lead to coherent structures. The instability mechanisms may be 3-D and the resultant structures and their interaction can be very complicated. Progress in modeling and understanding of the underlying physical mechanisms will more likely be made if the problem is broken down into various sub-aspects rather than if all issues are addressed simultaneously. We decided to advance simulation methodologies and understanding for related simplified model problems that exclude certain aspects of the overall scenario. In particular, using both water tunnel experiments and direct numerical simulations (DNS), we investigated 3-D separation bubbles on a flat plate. Separation was induced by a displacement body that was located in close proximity to the plate.

The flow around naval vessels is also characterized by high Reynolds numbers. Simulations of such flows are challenging for many reasons: The spectrum of turbulent length scales spans several orders of magnitude. Even with the most powerful supercomputers it is impossible to resolve all turbulence length scales. This motivates the development of turbulence models that capture as much resolved motion as permitted by the grid resolution and model all remaining smaller scale turbulent motion. For a variety of engineering problems that involve large-scale unsteadiness, Reynolds-averaged Navier-Stokes (RANS) does not yield accurate results and large eddy simulation (LES) is often not computationally feasible. In particular, LES suffers from a very restrictive grid resolution requirement near walls. An idea pursued by many researchers is to switch or gradually blend to RANS near walls. Speziale was among the first to propose a hybrid turbulence modeling approach that combines the advantages of RANS, LES, and DNS [Speziale 1997]. Ideally, hybrid models blend DNS, LES, and RANS such that optimal use is made of the available computational assets. This requires that the filter width is related to the spatial and temporal resolution and the employed turbulence models are state-of-the-art. In Speziale's approach the "feedback" from the turbulence model equations to the Navier-Stokes equations is scaled by a contribution function which is dependent on the local ratio of grid line spacing and Kolmogorov length scale. This approach was later called flow simulation methodology (FSM) [Fasel et al. 2002, Israel 2005, Zhang et al. 2000]. Another example of a hybrid model with a fixed filter width is the filter-based RANS (FBR) approach by Johansen et al. [2004]. This model was designed such that a one-equation sub-grid stress (SGS) model is recovered in the fine grid limit. Because the fixed filter width has to be chosen such that it is always larger than the local grid spacing, the spatial and temporal resolution will not always be optimal. This motivated Hajjawi et al. [2008] to employ the FBR with a local filter width. A simulation of a turbulent channel flow using a hybrid turbulence model, where a Smagorinsky model was switched to a RANS model was carried out by Hamba [2003]. A mismatch in the velocity profiles was observed at the interface region between the two approaches. Turbulent channel flow simulations by Piomelli et al. [2003] address this difficulty. The discontinuity at the interface is attributed to a mismatch of scales between RANS and LES. While the turbulence model supports most of the Reynolds shear stress in the RANS region, the resolved eddies must supply the dominant contribution in the LES region. In the transition region the eddy-viscosity contribution to the mean shear is too low while the energy-carrying eddies have not yet been generated. The problem can be partially remedied through the introduction of a "backscatter" model based on stochastic forcing. For example, Batten et al. [2004] introduced random velocity fluctuations obtained from a synthetic turbulence model for seeding turbulence in their hybrid turbulence model simulations of a turbulent channel flow.

Turbulent channel and diffuser flows are good test cases for such models. In particular, low Reynolds number duct flows are frequently chosen for DNS, RANS, and hybrid model validation efforts. The turbulent asymmetric diffuser flow experiment at Stanford University is a particularly well documented experiment [Cherry et al. 2008]. In this experiment the approach channel flow transitions fully before reaching the diffuser inlet. The approach flow Reynolds number was 15,380 based on hydraulic diameter and bulk velocity and 10,000 based on channel height and bulk velocity. Earlier 2-D diffuser experiments suffered from the fact that an infinite span cannot be realized in the laboratory. This issue is avoided for the 3-D diffuser because of the side walls. Using various different hybrid turbulence models we simulated the flow through the so-called baseline diffuser geometry for which full flow field experimental data is available [Cherry et al. 2008]. As these simulations are very compute time intensive we decided to modify and validate candidate hybrid RANS/LES models for a turbulent square-duct flow at a bulk Reynolds number of 10,000, because for this Reynolds number reference data for validation are available in the literature. Models that fail to predict the channel flow will likely also fail to predict the turbulent separation in the diffuser.

Turbulent duct flows such as the square-duct flow occur in many technical applications such as air ducts in buildings or ducts in aerospace and marine applications. In square-duct flows, an imbalance of the Reynolds-stresses near the corners results in a secondary flow which transports fluid into the corners [Nikuradse 1926]. With linear RANS models the Reynolds-stress imbalance cannot be captured and the secondary flow does not develop. Predictions of the secondary flow require non-linear Reynolds stress or full Reynolds-stress models. The low-Reynolds number square-duct flow is accessible by DNS. Huser and Biringen [1993] carried out a DNS of a square-duct flow for a Reynolds number based on bulk velocity and hydraulic diameter of Re = 10,320 (which corresponds to a Reynolds number based on mean friction velocity and hydraulic diameter of $Re_\tau = 600$). The computational grid had 96×101×101 points (streamwise × cross-flow directions) and dimensions 6.4h×h×h (length × width × height), where h is the channel height. The convective terms were discretized with fifth-order-accurate upwind biased finite-differences and the viscous terms were discretized with fourth-order-accurate central finite-differences. The minimum correlation in the streamwise direction was at $\Delta x = 3.2h$, indicating that the streamwise domain extent of $L_x = 6.4h$ was sufficient. The comparison with a RANS calculation based on Speziale's non-linear k-ε model revealed some significant differences between the model behavior and the DNS results, such as for example, an under-prediction of the intensity of the secondary flow [Huser at al. 1994]. Gavrilakis [1992] simulated a square-duct flow at $Re_\tau = 300$. The computational domain for this DNS had dimensions 5πh×h×h with 1000×127×127 points. The code was second-order-accurate in both, space and time. In LES sub-grid turbulence is modeled thus allowing for a lower grid resolution compared to DNS. Madabhushi and Vanka [1991] carried out a LES with the Smagorinsky SGS model of a square-duct flow at $Re_\tau = 360$ (Re = 5,810). The grid resolution was 65×65 in the cross-flow plane with 32 Fourier modes in the streamwise direction. The dimensions of the computational domain were 2πh×h×h. The discretization was second-order-accurate. We employed DNS and RANS as well as hybrid RANS/LES for simulating the square-duct flow with different grid resolutions. For the hybrid simulations, we utilized both the FSM and FBR based on different versions of the k-ω model by Wilcox [2006].

This report is organized as follows: In Section 2 the scope of investigations is introduced. Section 3 provides details on the simulation strategies and water tunnel experiments. Results are provided in Sections 4-7. Finally, in Section 8 the results are summarized and conclusions are drawn.

## 2. SCOPE OF INVESTIGATIONS

The main objective of our numerical investigations and water tunnel experiments was to gain insight into the physical mechanisms governing 3-D separation. Of particular interest were the development, dynamics, and interaction of energetic vortical structures (spanwise/streamwise) that develop from the different hydrodynamic instabilities that are present in 3-D separated flows.

We also investigated the flow through the Stanford asymmetric diffuser by J. Eaton and co-workers [Cherry et al. 2008], which is a challenging benchmark for evaluating the performance of different turbulence modeling approaches such as 3-D RANS and hybrid RANS/LES. Of particular interest here was the development of improved turbulence models for complex, non-equilibrium turbulent shear flows. As a reference, and for validation of our simulation codes, we also considered the turbulent square-duct flow. This flow is less challenging but better documented than the diffuser flow and thus served as an additional test case for the various turbulence models.

In summary, our approach consisted of:

1) High-resolution DNS of 3-D separation bubbles on a flat plate (§4)
2) Water tunnel experiments of 3-D separation bubbles on a flat plate (§5)
3) Turbulent square-duct flow simulations (§6)
4) Simulations of the turbulent flow through the Stanford baseline asymmetric diffuser (§7)

We considered three different geometries:

1) We carried out simulations and experiments where we investigated 3-D separation bubbles on a flat plate. Separation was induced through the close vicinity of an asymmetric displacement body.
2) For turbulence model validation we simulated the turbulent flow through a square-duct.
3) We simulated the turbulent flow through the Stanford asymmetric diffuser which was designed and tested by J. Eaton and co-workers at Stanford University.

## 2.1 Geometry 1: Axisymmetric Displacement Body over Flat Plate

In the water tunnel experiments, an axisymmetric cone-shaped displacement body of diameter D with a spherical front end was placed in close proximity above a flat plate to generate a separation bubble on the flat plate (see Fig. 2.1). Suction was applied through holes in the displacement body in order to prevent separation at the aft section of the displacement body.
All measurements and computations are for a body diameter of D=0.1m and a half-opening angle of 20°. By adjusting the distance H of the displacement body from the flat plate, the non-dimensional pressure distribution can be altered. The boundary layer thickness at separation can be varied by either moving the body in the streamwise direction or by changing the approach flow velocity $U_\infty$. For both simulations and experiments the distance to the leading edge of the flat plate was kept constant at s = 0.25m.

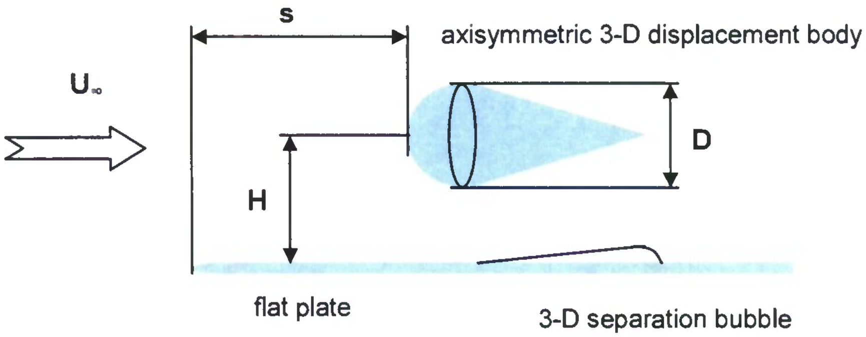

*Fig 2.1: Axisymmetric displacement body over flat plate.*

## 2.2 Geometry 2: Stanford Asymmetric Diffuser

We simulated the flow through the asymmetric 3-D diffuser by Eaton and co-workers (Fig. 2.2) for which high resolution velocity volume data is available [Cherry et al. 2008]. The rectangular duct approach flow has cross-flow dimensions h×3.33h (height × width) and a length that is sufficient to guarantee fully turbulent flow at the diffuser inlet. The approach flow Reynolds number is 10,000 based on duct height and bulk velocity and 15,380 based on hydraulic diameter and bulk velocity. The diffuser opening angles are atan(4−1)/15=11.3deg and atan(4−3.33)/15=2.56deg. The cross-sectional area at the diffuser exit is 4×4=16. The experimental data shows turbulent separation in the diffuser.

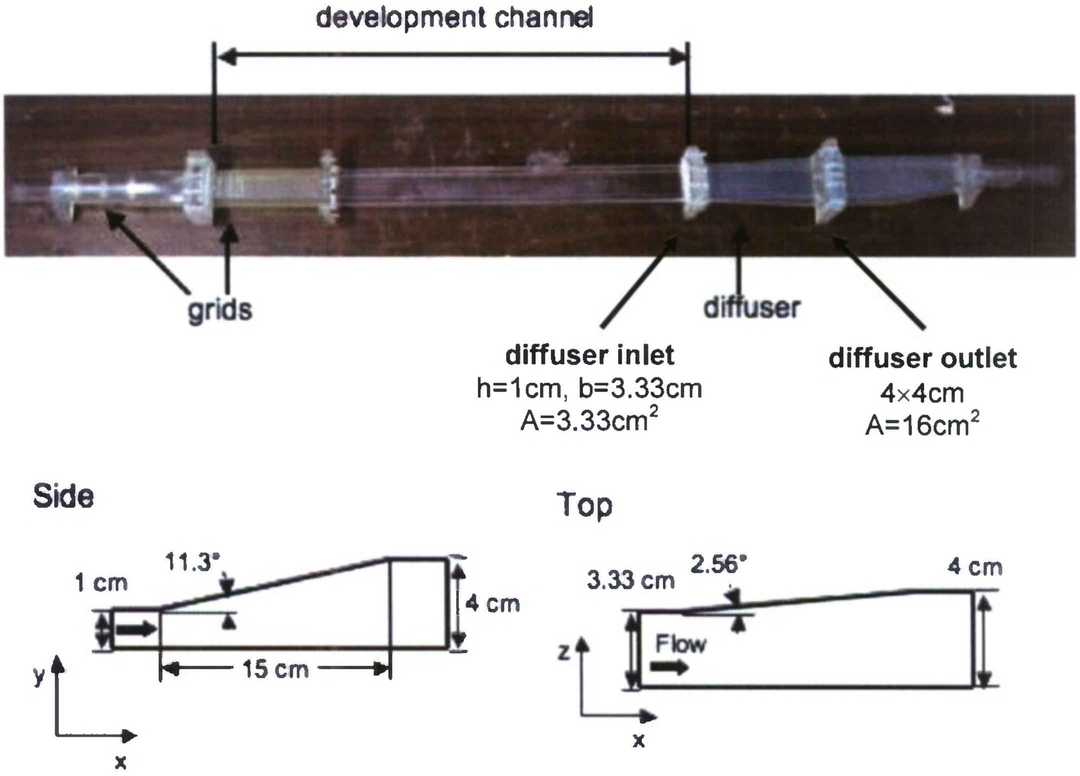
development channel
grids
diffuser
diffuser inlet
h=1cm, b=3.33cm
A=3.33cm²
diffuser outlet
4×4cm
A=16cm²
Side
1 cm
11.3°
4 cm
15 cm
y
x
Top
3.33 cm
2.56°
4 cm
Flow
z
x

*Fig. 2.2: Stanford baseline diffuser.*

### 2.3 Geometry 3: Square-Duct

In addition, we investigated the turbulent flow through a square-duct at a Reynolds number based on hydraulic diameter and bulk velocity of 10,000. Because this Reynolds number is close to the Reynolds number of the diffuser approach flow we were confident that turbulence modeling strategies that were successful for the square-duct flow would also likely be adequate for diffuser flow simulations.

# 3. COMPUTATIONAL AND EXPERIMENTAL APPROACH

## 3.1 Computational Methods

For our simulations we employed two different numerical methods:
(1) A high-order-accurate incompressible DNS code (for geometry 1)
(2) A high-order-accurate compressible multi-domain finite volume code (for geometries 2 & 3)

### 3.1.1 Method 1: Higher-Order-Accurate Incompressible Finite Difference Code

For our Direct Numerical Simulations (DNS) of 3-D separation bubbles on a flat plate we employed a highly efficient and accurate incompressible Navier–Stokes code originally developed for flat-plate boundary layer transition simulations [Meitz 2000] and later extended to generalized curvilinear orthogonal coordinates [Postl 2006].

#### *3.1.1.1 Governing Equations*

In this code, the 3-D incompressible Navier–Stokes equations are solved in vorticity-velocity formulation. The equations are non-dimensionalized using a reference velocity $U_{ref}$ (e.g. the freestream velocity) and a reference length $L_{ref}$. By taking the curl of the momentum equations, which eliminates the pressure terms, the transport equation for the vorticity (in vector form) is obtained,

$$\frac{\partial \vec{\omega}}{\partial t} + \nabla \times \left(\vec{\omega} \times \vec{V}\right) = \frac{1}{\mathrm{Re}} \nabla^2 \vec{\omega} + \nabla \times \vec{F}, \tag{3.1}$$

with the vorticity defined as

$$\vec{\omega} = -\nabla \times \vec{V}. \tag{3.2}$$

A volume force $\vec{F}$, can be added to the right-hand-side to introduce disturbances into the flow. From the vorticity $\vec{\omega}$, the velocity field $\vec{V}$ is obtained by solving a vector Poisson equation,

$$\nabla^2 \vec{V} = \nabla \times \vec{\omega}. \tag{3.3}$$

The velocity vector $\vec{V}$ has components in the streamwise, wall-normal, and spanwise direction ($u$, $v$, and $w$), and the components of the vorticity vector $\vec{\omega}$ are defined as

$$\omega_x = \frac{\partial v}{\partial z} - \frac{\partial w}{\partial y}, \qquad \omega_y = \frac{\partial w}{\partial x} - \frac{\partial u}{\partial z}, \qquad \text{and} \qquad \omega_z = \frac{\partial u}{\partial y} - \frac{\partial v}{\partial x}. \tag{3.4}$$

#### *3.1.1.2 Discretization*

For the time-integration of the vorticity-transport equations, a four-stage explicit Runge–Kutta scheme with fourth-order accuracy is employed. For the spatial discretization, fourth-order accurate compact finite differences are used in the streamwise and in the wall-normal direction. Assuming periodicity in the spanwise direction, a pseudo-spectral approach in $z$ is used with a Fourier decomposition of the velocity and vorticity into finite sine and cosine series with $k = [0 \ldots K]$ Fourier components. For the flow variables u, v, and $\omega_z$ the Fourier series has the form

$$d(x, y, z, t) = D^{k=0}(x, y, t) + \sum_{k=1}^{K} D^{k}(x, y, t)\cos(\gamma^{k} z) - \sum_{k=-1}^{-K} D^{k}(x, y, t)\sin(\gamma^{k} z), \tag{3.5}$$

with $d = u$, $v$, $\omega_z$ and $D^k = U^k, V^k, \Omega_z^k$. For the flow variables $w$, $\omega_x$, and $\omega_y$ the Fourier series has the form

$$d(x, y, z, t) = D^{k=0}(x, y, t) + \sum_{k=1}^{K} D^{k}(x, y, t)\sin(\gamma^{k} z) + \sum_{k=-1}^{-K} D^{k}(x, y, t)\cos(\gamma^{k} z), \tag{3.6}$$

with $d = w$, $\omega_x$, $\omega_y$ and $D^k = W^k, \Omega_x^k, \Omega_y^k$. The spanwise wave number, $\gamma^k$, is defined as

$$\gamma^k = 2\pi k \, \lambda_z^{k=1}, \tag{3.7}$$

where $\lambda_z^{k=1}$ is the spanwise wavelength of the lowest spanwise Fourier mode, which effectively is the domain width, $L_z$, of the computational domain. In the Fourier sine and cosine expansions Eqs. (3.5) and (3.6), the two-dimensional flow component is represented by mode $k = 0$. The symmetric part of the three-dimensional flow field is represented by modes $1 \leq k \leq K$, the asymmetric part by modes $-K \leq k \leq -1$. In all our present simulations we assumed spanwise symmetry, which halves the number of spanwise modes required but introduces slip walls at $z = L_z$ and $L_{z/2}$ where $w$, $\omega_x$, $\omega_y = 0$. This confines the movement of streamwise structures in the flow by preventing them from meandering across the symmetry plane.

A key component of the present code is a fast and parallelized multi-grid solver for computing the velocity-Poisson equations. At every computational step, disturbances at grid level in the vorticity components are filtered out using a fourth-order compact filter. This allows for simulations on grids that cannot resolve turbulent structures all the way down to the Kolmogorov length scale.

### *3.1.1.3 Computational Setup*

At the inflow boundary, steady velocity and vorticity profiles are imposed. To prevent reflections from the outflow boundary at $x_{out}$, the flow is relaminarized in a buffer domain starting at $x_{buff}$ using an approach similar to that proposed by Kloker et al. [Kloker 1993]. At the free stream boundary, $y_{max}$, the flow is assumed to be irrotational and all vorticity components and their derivatives are set to zero. Also, a Dirichlet boundary condition is applied for the wall-normal velocity. The wall-normal velocity was obtained from precursor calculations that are described in Section 4.1. At the wall, $y = 0$, no-slip and no-penetration conditions are imposed. Numerous simulations with different domain sizes, grid resolutions, baseflow and forcing parameters, etc., have been performed over the course of the present research project. Details on the computational parameters for the different simulations are provided in Section 4.

#### *3.1.1.4 Disturbance Generation*

Disturbances are introduced through a blowing and suction slot on the flat plate. The slot is modeled by prescribing a wall-normal velocity distribution

$$v_{bs}^{(k)} = A_{bs}^{(k)} \sin(\pi \frac{\xi - x_{s1}}{x_{s2} - x_{s1}})^3 \tag{3.8}$$

on the wall for each spanwise mode k. The time-dependent amplitudes $A_{bs}^{(k)}$ of the spanwise modes are defined as

$$A_{bs}^{(k)}(t) = A_{bs}^{(k)} \sin(2\pi f_{bs}^{(k)} t + \theta_{bs}^{(k)}), \tag{3.12}$$

with frequency, $f^k$, and phase angle, $\theta^k$. The freestream effect of the slot forcing was modeled assuming potential flow over an infinitely long flat plate with a velocity distribution at the wall that corresponds to the blowing and suction slot. Using a Green's function, the potential is given by

$$\Theta(x,y) = \frac{1}{2\pi} \int_{x_{s1}}^{x_{s2}} v_w(\xi) \log[\xi - x)^2 + y^2] d\xi, \tag{3.9}$$

where $x_{s1}$ and $x_{s2}$ are the downstream and upstream boundaries of the blowing and suction slot, respectively. The change in the freestream velocity and its derivative then become

$$v(x,y) = \frac{1}{2\pi} \int_{x_{s1}}^{x_{s2}} v_w(\xi) \frac{2y}{(\xi - x)^2 + y^2} d\xi \quad \text{and} \quad \frac{dv}{dy}(x,y) = \frac{1}{2\pi} \int_{x_{s1}}^{x_{s2}} v_w(\xi) \frac{2(\xi - x)^2 - 2y^2}{[(\xi - x)^2 + y^2]^2} d\xi. \tag{3.10}$$

With this method, symmetric or asymmetric disturbances can be introduced at any downstream location.

### 3.1.2 Method 2: Higher-Order-Accurate Compressible Multi-Domain Finite Volume Code

#### *3.1.2.1 Governing Equations*

The Favre-averaged compressible Navier–Stokes equations are solved in conservative form on structured grids. A variety of turbulence models was implemented for Reynolds-Averaged Navier–Stokes (RANS) calculations of turbulent flows. For the current investigations [Gross and Fasel 2008b, 2009a, 2010], the 1988, 1998, and 2006 versions of the *k*–ω model by Wilcox [Wilcox 2006] were employed. The 1998 and 2006 versions allow for improved predictions of shear layers. The Menter shear-stress transport (SST) model [Menter 1994] which removes the $k$–$\omega$ models sensitivity to the free-stream value of the turbulence specific dissipation [Menter 1992], the $k$–$\varepsilon$ model [Jones, 1972], the Lam-Bremhorst low-Reynolds number *k*–ε model [Lam 1981], and the Spalart–Allmaras one-equation turbulence model [Spalart 1992] were considered as well. In the original formulations of the various turbulence models addressed above, the Boussinesq-approximation (in the following referred to as B-A) is employed for computing the Reynolds stresses,

$$\tau_{ij}^{T} = -\frac{2}{3}\rho k \delta_{ij} + 2\mu_T \left( S_{ij} - \frac{1}{3} v_{k,k} \delta_{ij} \right) \tag{3.11}$$

where $k$ is the turbulence kinetic energy, $S_{ij}=1/2(u_{i,j}+u_{j,i})$ and $W_{ij}=1/2(u_{i,j}-u_{j,i})$ are the strain and shear rate tensor, and $\delta_{ij}$ is the Kronecker symbol. Repeated indices indicate summations while commas in the subscript denote partial derivatives. The B-A assumes a linear relation between the strain tensor and the Reynolds stress tensor. The B-A can therefore be categorized as a linear eddy viscosity model (LEVM). Alternatively, a second-moment closure, the explicit algebraic stress model (EASM) in the form proposed by Rumsey and Gatski [Rumsey 2001],

$$\tau_{ij}^{T} = -\frac{2}{3}\rho k\delta_{ij} + 2\mu_T\left[\left(S_{ij} - \frac{1}{3}v_{k,k}\delta_{ij}\right) + a_2a_4\left(S_{ik}W_{kj} + S_{jk}W_{ki}\right) - 2a_3a_4\left(S_{ik}S_{kj} - \frac{1}{3}S_{kl}S_{kl}\delta_{ij}\right)\right] \quad (3.12)$$

can be employed.

A large number of different hybrid RANS/LES models were proposed for closing the gap between RANS and LES. We considered the flow simulation methodology (FSM) [Speziale 1997, Fasel et al. 2002] and the filter-based RANS (FBR) approach [Johansen et al. 2004]. For the flow simulation methodology (FSM) the turbulence model contribution is scaled by a "contribution function", f, which in the original formulation by Speziale is a function of the local grid spacing, $\Delta=\max(\Delta x,\Delta y,\Delta z)$, and the Kolmogorov length scale (the characteristic length scale of the dissipating eddies),

$$L_k = \left(\frac{\upsilon^3}{\varepsilon}\right)^{\frac{1}{4}}. \quad (3.13)$$

Israel [2005] suggested that a third length scale, the "dissipation length scale" (the typical length scale of the stress-bearing motion),

$$L_\varepsilon = \frac{k^{3/2}}{\varepsilon} \quad (3.14)$$

which is larger than the integral length scale, $c_\mu k^{3/2}/\varepsilon$, should be considered. For $f = 0$ all scales of motion are resolved and the model contribution is zero; In the RANS limit for $f = 1$ the model contribution is 100% and all unsteady turbulent motion is modeled. Effectively, FSM simulations can be considered to be locally DNS, large eddy simulation (LES), or RANS depending on the local and instantaneous ratio of $\Delta/L_k$.

Two alternatives were suggested: (1) Only the terms that "feed back" into the Navier-Stokes equations are scaled. The turbulence model is "dragged along" and influenced only indirectly since, as a result of the scaling, either the mean flow is changed or the flow becomes unsteady. (2) All turbulence model terms including those that feed back into the turbulence model equations itself are scaled. For the present results we employed approach (2).

Different variants of the contribution function are available. For example, Zhang et al. [2000] proposed a modified Speziale contribution function,

$$f = 1 - \exp\left[-0.001\max\left(0, \frac{\Delta}{L_k} - 2\right)\right] \quad (3.15)$$

Alternatively, and this is the approach that we employed for the results shown here, the contribution function can be computed from the turbulence energy spectrum (Fig. 3.1).

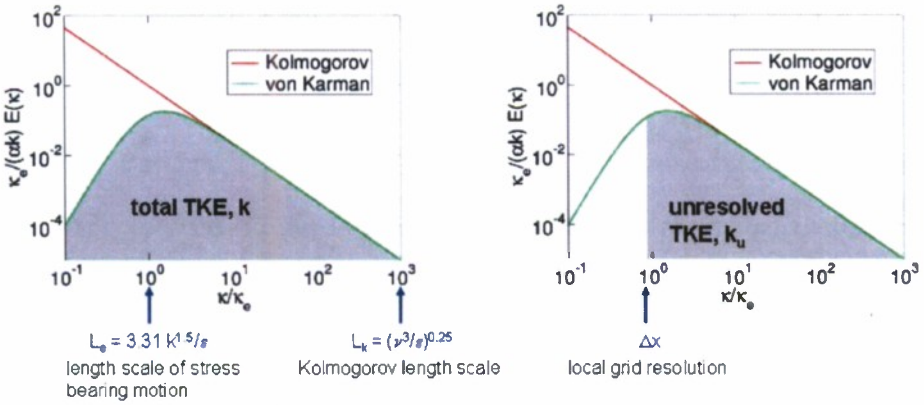

*Fig. 3.1: Turbulence energy spectra.*

Estimates for the unresolved, $k_u$, and total, k, turbulence kinetic energy can be obtained by integrating the turbulence energy spectrum, $E(\kappa)$, from $L_k$ to $L_\Delta$ and $L_k$ to $L_\varepsilon$, e.g.

$$k = \int_{2\pi/L_\varepsilon}^{2\pi/L_k} E(\kappa)d\kappa\,. \tag{3.16}$$

The ratio of $k_u$ and k gives the contribution function,

$$f = \frac{k_u}{k}\,. \tag{3.17}$$

For $L_\varepsilon < L_k$, f is set to 1. As $E(\kappa)$ we chose the von Kármán [1948] energy spectrum. The length scales were computed as $L_\varepsilon = f^{-1/2} L_{\varepsilon u}$ and $L_k = f^{1/4} L_{ku}$.

For filter-based RANS (FBR) [Johansen et al. 2004] the RANS eddy viscosity is multiplied by

$$f = \min\left(1, C_3 \frac{L_\Delta \varepsilon}{k^{3/2}}\right) \tag{3.18}$$

where the filter width, $L_\Delta$, is fixed in the original formulation. Similar to Hajjawi et al. [2008] we decided to use a local filter width identical to the local grid line spacing. We also set $C_3$ to 1.

For both approaches, FSM and FBR, which are described in more detail in [Gross and Fasel 2009a,b] we attempt to capture "backscatter". The term

$$\frac{\rho k_u}{f}\left(\frac{\partial f}{\partial t}+u\frac{\partial f}{\partial x}+v\frac{\partial f}{\partial y}+w\frac{\partial f}{\partial z}\right) \tag{3.19}$$

is added to the RHS of the ρk-equation and subtracted from the RHS of the ρe-equation. In addition, $-\rho u_i'(f_{,t}+u_j f_{,j})$ is added to the RHS of the momentum equations for $f_{,t} + u_j f_{,j} < 0$. Artificial velocity fluctuations, $u_i'$, are obtained from the synthetic turbulence model proposed by Batten et al. [2004]

For the channel flow simulations the term,

$$\frac{1}{2}\rho u_b^2 f \frac{1}{D_h} = \frac{4}{D_h}\rho \bar{u}_\tau \tag{3.20}$$

was added to the RHS of the x-momentum equation to compensate for the streamwise pressure drop. Here, $u_b$ is the bulk velocity (mass flux divided by density and cross-sectional area). The hydraulic diameter, $D_h = 4A/U$, is computed from the channel cross-section, A, and circumference, U. For turbulent channel flow, the friction factor, f, can be obtained from empirical relations, such as the one given by Petukhov,

$$f = (0.79 \ln \mathrm{Re}_b - 1.64)^{-2}, \tag{3.21}$$

where the Reynolds number is based on bulk velocity and hydraulic diameter. The relationship between bulk velocity and mean friction velocity is,

$$f = \left(\frac{\bar{u}_\tau}{u_b}\right)^2. \tag{3.22}$$

We also added volume forcing terms to the continuity and energy equations

$$\rho_t + \ldots = \alpha(\rho_{ref} - \rho) \tag{3.23}$$

$$(\rho e)_t + \ldots = \alpha \rho c_v (T_{ref} - T) \tag{3.24}$$

with $\alpha = 10^{-4}$ to stabilize density and temperature for the channel flow simulations (we employed a compressible code).

#### *3.1.2.2 Discretization*

The governing equations are solved in curvilinear coordinates. For robustness (especially on highly distorted grids) a finite volume method is employed. The convective terms of the Navier-Stokes equations are discretized with a ninth-order-accurate upwind scheme based on a weighted essentially non-oscillatory extrapolation of the characteristic variables and the Roe scheme [Gross and Fasel 2002, 2008a]. We also considered the second-order-accurate symmetric total variation diminishing (TVD) scheme by Yee [1987]. This choice was made since according to Margolin and Rider [2002] certain second-order-accurate upwind schemes have similar properties as standard LES sub-grid models. The convective terms of the turbulence model equations are discretized with a second-order-accurate discretization analogous to the symmetric TVD scheme by Yee [1987]. Fourth- and second-order-accurate discretizations, respectively, are employed for computing the Navier-Stokes viscous terms and the turbulence equations diffusion terms. An implicit second-order-accurate Adams-Moulton method is used for advancing the governing equations in time. The resulting system of equations is solved iteratively by a Newton iteration based on a line Gauss-Seidel algorithm. The convergence of the implicit method is monitored by considering the root mean square (RMS) of the residuals of all cells for each individual equation. For the time dependent results shown in this paper the equations were advanced to the next time step when all RMS residuals dropped below 0.05. The code was parallelized using the message passing interface (MPI) library.

### *3.1.2.3 Inflow and OutflowCconditions*

We considered walls to be adiabatic. The turbulence kinetic energy, k, was set to zero at walls. For the k-ω models the smooth wall boundary condition [Wilcox 2006],

$$\omega = \frac{1}{\mathrm{Re}^2}\frac{N\mu}{\rho\Delta y^2} \tag{3.25}$$

was applied for ω, where Δy is the distance from the wall to the center of the first cell away from the wall. The parameter N was set to 1600. This value guarantees that for near wall grid resolutions (in wall units) of $y^+ = 1$ the effective surface roughness $k^+$ is less than 5, which corresponds to a hydraulically smooth surface. For the channel flow simulations periodicity conditions were applied in the streamwise direction. For the diffuser simulations, at the diffuser inflow the pressure was extrapolated and all other primitive variables were taken from a channel flow simulation. At the diffuser outflow a non-reflecting boundary condition [Gross and Fasel 2007] was applied.

### *3.1.2.4 Non-Dimensionalization*

All length scales were non-dimensionalized with the channel height, h, which for the square-duct is identical to the hydraulic diameter, $D_h = 4A/U = 4h^2/4h = h$. Velocities were non-dimensionalized with the bulk velocity, $u_b$, based on the nominal given bulk Reynolds number, hydraulic diameter, and kinematic viscosity. Alternatively, the average friction velocity, $\overline{u_\tau}$, can be employed for non-dimensionalization. The desired bulk velocity in our square-duct flow simulations was $Re_b = 10{,}000$. From Petukhov's relationship a friction factor of f = 0.031479 is obtained. The average friction velocity then becomes

$$\overline{u_\tau} = \sqrt{\frac{f}{8}}u_b = 0.06273u_b \tag{3.26}$$

and the Reynolds number based on average friction velocity and hydraulic diameter is $Re_\tau = 627.3$. With the average friction velocity,

$$y^+ = \frac{y\overline{u_\tau}}{\upsilon_w} = \mathrm{Re}_\tau\frac{y}{D_h} = 627.3\frac{y}{D_h}\text{, and} \tag{3.27}$$

$$u^+ = \frac{u}{u_\tau} = \frac{\mathrm{Re}_b}{\mathrm{Re}_\tau}\frac{u}{u_b} = 15.94\frac{u}{u_b} \tag{3.28}$$

are obtained. Viscosities were normalized with the reference dynamic viscosity. Turbulence kinetic energy and Reynolds-stresses were non-dimensionalized with the bulk velocity squared.

### 3.1.3 Post-Processing Tools

#### *3.1.3.1 Vortex Identification*

For visualizing vortical structures we employed the Q-criterion by Hunt [1988],

$$Q = 1/2 W_{ij}\, W_{ij} - 1/2\, S_{ij} S_{ij}\,, \tag{3.29}$$

which identifies vortical structures by representing regions inside the flow where rotation, $W_{ij}$, dominates strain, $S_{ij}$.

#### *3.1.3.2 Auto-Correlation*

Discrete time-dependent velocity data, $u_n$, can be auto-correlated,

$$R(m) = \frac{1}{\sigma^2 N}\sum_{n=1}^{N}\left(u'_n\right)\left(u'_{n+m-1}\right) \tag{3.31}$$

for m = 1,…,N where u′ = u − $\bar{u}$ is a disturbance velocity,

$$\sigma^2 = \sum_{n-1}^{N}\left(u'_n\right)^2 \tag{3.32}$$

is the variance, and the index n + m − 1 is taken modulus N.

#### *3.1.3.3 Energy Spectrum*

Energy spectra,

$$E(\kappa_m) = \frac{a_m^2 + b_m^2}{4\dfrac{d\kappa_m}{dm}}, \tag{3.33}$$

can be computed from velocity data, $u_n$, where

$$a_m = \frac{2}{N}\sum_{n=1}^{N} u_n \cos(\kappa_m t_n) \tag{3.34}$$

$$b_m = \frac{2}{N}\sum_{n=1}^{N} u_n \sin(\kappa_m t_n). \tag{3.35}$$

For a linear wave number (κ = 2π/Δt) distribution

$$\kappa_m = \kappa_1 + \frac{m-1}{M-1}(\kappa_2 - \kappa_1), \tag{3.36}$$

$$\frac{d\kappa_m}{dm} = \frac{\kappa_2 - \kappa_1}{M-1} \tag{3.37}$$

is obtained.

## 3.2 Experimental Facility

### 3.2.1 Water Tunnel

The Hydrodynamics Laboratory of the Department of Aerospace and Mechanical Engineering at the University of Arizona is a state-of-the-art research facility that houses three water tunnels.

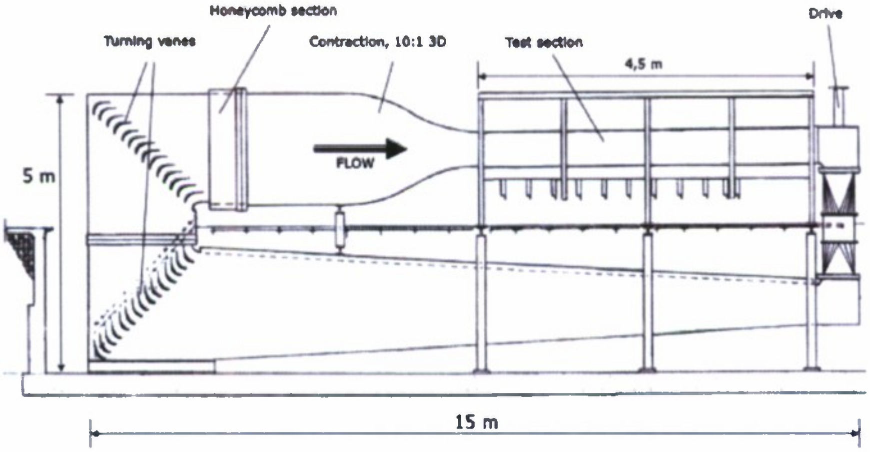

*Fig. 3.2: Sketch of closed water tunnel at the Hydrodynamics Laboratory at the Aerospace and Mechanical Engineering Department.*

Our experiments were conducted in the "high-speed" closed surface water tunnel. This tunnel has a test section with dimensions 0.5 x 0.7m. The maximum flow velocity in the test section is 1.34 m/s. A side view of the tunnel is given in Fig. 3.2. A 7.5 kW electric motor drives a four-bladed turbine. The pitch of the turbine blades can be adjusted for altering the velocity range. The water is fed back through a pipe in the basement. A 0.2m wide honey comb section is used for conditioning the flow (flow straightening, turbulence management). Some key parameters are listed in Tab. 3.1. A chart showing the velocity range for two different turbine blade pitch angles is provided in Fig. 3.3.

| | |
|---|---|
| Test Section Size | 4.5 m x 0.5 m x 0.7 m |
| Velocity Range slow | 0.03 m/s - 0.58 m/s |
| Velocity Range high | 0.08 m/s - 1.34 m/s |
| Water Volume | 56.000 liters |

*Tab. 3.1: Specifications of closed water tunnel.*

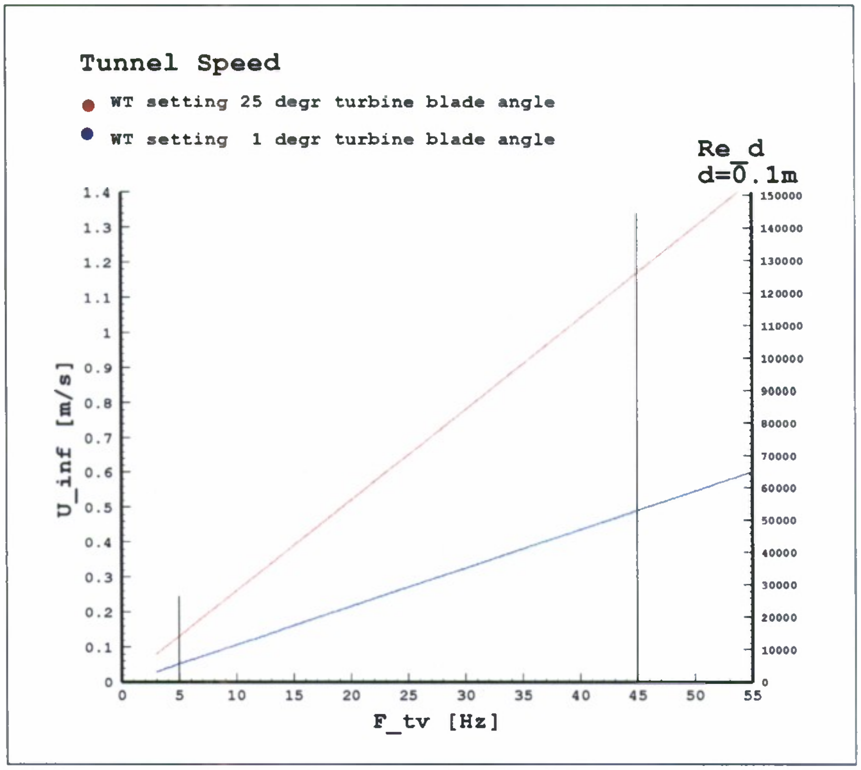

*Fig. 3.3: Tunnel speed over turbine revolutions per second for different turbine blade pitch angles. Velocity data was obtained from PIV measurements.*

### 3.2.2 Flow Diagnostics

In general, dye flow visualization is less involved and was therefore employed for fast and qualitative flow diagnostics, which provided considerable insight into the fluid dynamics. We utilized both, red and blue dye, which was delivered into the flow through holes, and phosphorescent dye, which was injected with a needle. The advantage of phosphorescent dye is that it allows for flow visualizations in a plane that is illuminated by a laser.

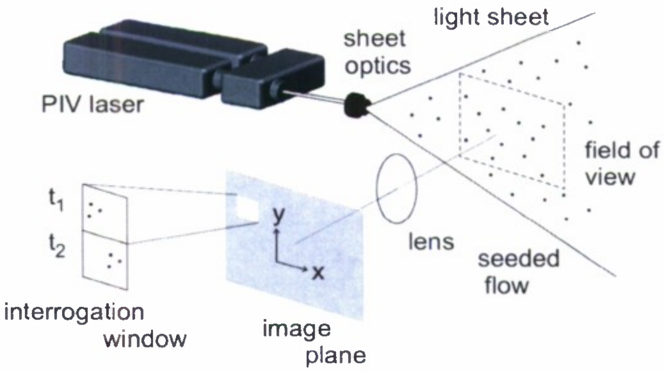
light sheet
sheet optics
PIV laser
field of view
$t_1$
$t_2$
y
x
lens
seeded flow
interrogation window
image plane

*Fig. 3.4: Sketch of PIV system.*

We also employed Particle Image Velocimetry (PIV) for quantitative flow measurements. In general, PIV requires a high power laser, an optical arrangement to widen the laser beam into a light sheet (cylindrical lens), and a camera (Fig. 3.4). Velocity fields are extracted from the movement of particles seeded into the flow. The particles are almost neutrally buoyant, and are therefore generally assumed to be accurately convected by the flow. The measurement area within the flow field is defined by the position of a laser sheet and the optical opening angle of the cameras. Using two short duration laser pulses, a double-exposure of the flow field is obtained. The velocity vectors are extracted by performing a mathematical correlation analysis of the two separate frames. The PIV interrogation process is repeated until all required velocity information is extracted from the snapshots.

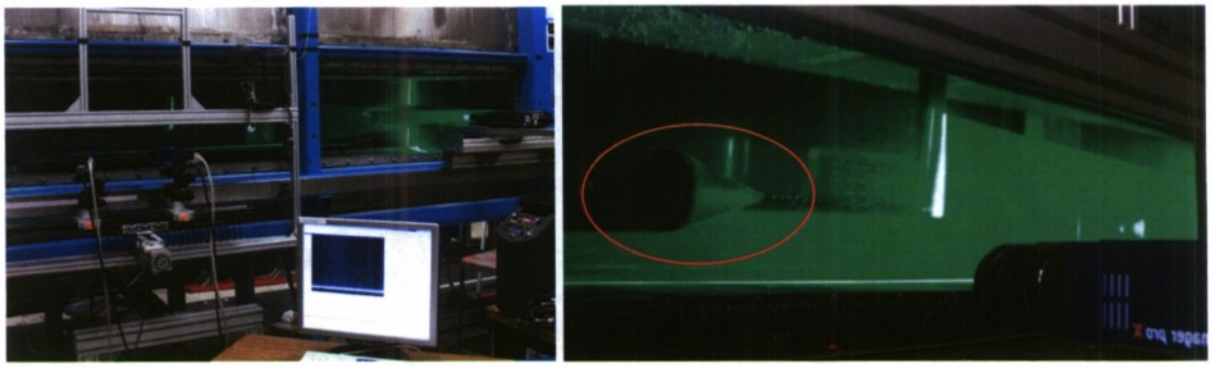

*Fig. 3.5: Photo of PIV system including cameras, laser, PIV computer and traverse system on the left. Seeded flow and laser beam with displacement body in test section on the right.*

A PIV system manufactured by LaVision was employed for our investigations (funded by a DURIP grant from ONR). This system consists of a double pulsed Nd:YAG laser (class 4), two high quality digital cameras and a Dell quad-core computer for post-processing (Fig. 3.5). The Imager ProX2M cameras with Nikon lenses have a maximum frame rate of 30Hz at full resolution. We designed and built a traverse system that uses computer-controlled stepper motors for moving the laser and cameras in downstream direction. The traverse system allows us to map out the entire volume which contains the three-dimensional separation bubble in fine slices. For the results shown in this report the laser beam was pointed at a mirror located in the rear of the test section for generating laser sheets in spanwise planes with a thickness of approximately 2mm. Two cameras are used to detect the particle movements within the plane. Hollow glass spheres with a diameter of approximately 10 microns, which are neutrally buoyant, were used as tracer particles.

# 4. SEPARATION BUBBLE: DIRECT NUMERICAL SIMULATIONS

The objective of our direct numerical simulations (DNS) and water tunnel experiments was to investigate in detail the structure and dynamics of three-dimensional (3-D) separation bubbles. In this section, results from our simulations are presented. The water tunnel experiments are discussed in section §5.

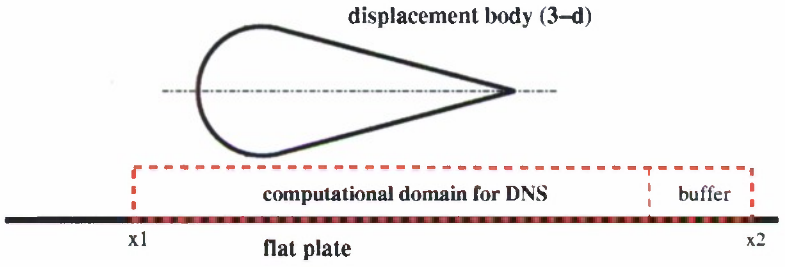

*Fig. 4.1(a): Schematic of set-up with displacement body and computational domain.*

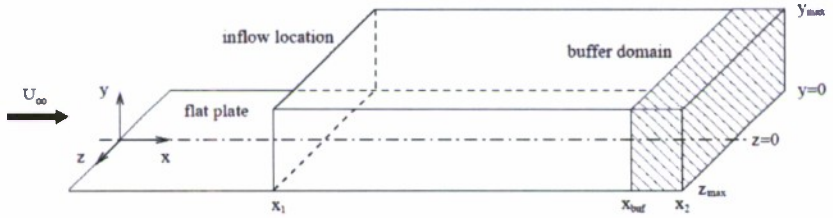

*Fig. 4.1(b): Schematic of computational domain for DNS.*

### 4.1 Precursor Calculations

Our computational approach involves two steps:

1. A precursor calculation of the inviscid flow around the displacement body.
2. A high-resolution Direct Numerical Simulation (DNS) of the separated flow region on the flat plate with freestream boundary conditions that are extracted from the precursor calculation.

The purpose of the precursor calculations is to obtain freestream boundary conditions for the highly resolved DNS and to study the effect of the geometric parameters on the potential flowfield. The calculations are based on the method described by Zedan and Dalton [1978] for computing the potential flow around a body of revolution with arbitrary shape. Corresponding to the body shape, linear source and sink distributions on the axis of rotation are determined and superposed on a uniform flow. The source and sink distributions are found by solving a system of linear equations, which is obtained from the conditions that (i) the streamfunction is zero at a certain number of control points on the body surface, and (ii) the net mass flux of the entire source and sink distribution is zero. To account for the presence of the flat plate, a mirror image is generated and added to the original solution. The change of the original body shape due to the mirroring was found to be negligible. For validation purposes, the wall-normal velocity profiles obtained with this procedure were compared to results of inviscid and viscous simulations of the entire flow field (flat plate and displacement body) using the commercial Navier-Stokes solver Fluent. The profiles extracted from the potential flow field and from the inviscid Fluent simulations agree very well and are also in very good agreement with the profiles extracted from the viscous Fluent simulations (Fig. 4.2). Similarly, the influence of "neighboring" displacement bodies due to the periodic boundary condition of the DNS was accounted for by repeating and mirroring the solution in the spanwise direction.

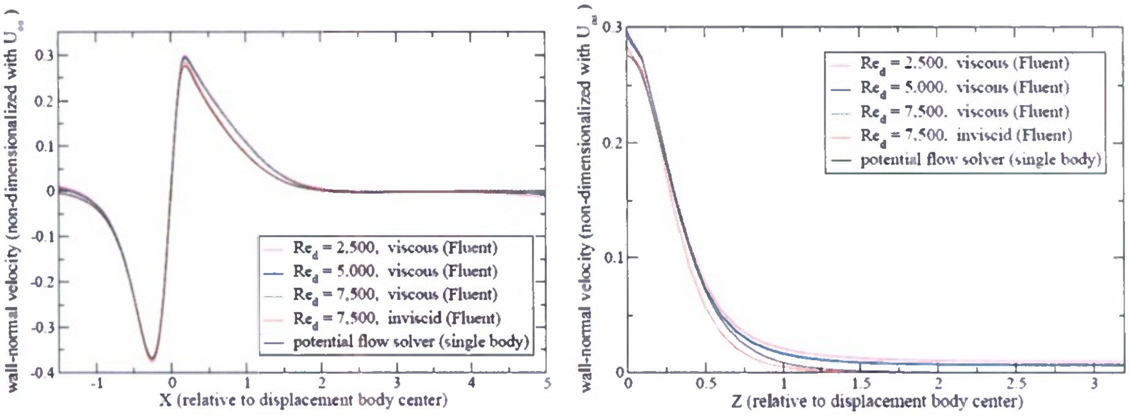

(a) Profiles of wall-normal velocity in the mid-span plane.

(b) Profiles of wall-normal velocity in spanwise direction at the downstream location of the suction peak.

*Fig. 4.2: Profiles of wall-normal velocity at wall-normal location $y_{max}$= 0.048m, extracted from potential flow and Fluent precursor calculations for different Reynolds numbers $Re_D$ (for the baseline case with H=1m).*

## 4.2 Simulation Setup

The computational domain for the high-resolution DNS is shown in Fig. 4.1b. The inflow boundary is located at a distance $x_1$=0.1m from the leading edge of the flat plate. The domain extends a distance $y_{max}$ from the surface of the flat plate. It spans from the midspan plane at z = 0 to z = $z_{max}$. For all simulations flow symmetry with respect to the body center was assumed. In addition, the flow was assumed to be periodic in the spanwise direction. The distance of the displacement body from the flat plate leading edge was s = 0.25m, or 0.15m measured from the inflow boundary of the computational domain. The spanwise variation of the freestream velocity at the inflow boundary due to the upstream influence of the displacement body was less than three percent. The streamwise domain length including the outflow was 0.640m for the unsteady cases and 0.768m for the steady cases. The outflow boundary was thus at $x_2$ = 0.740m and 0.868m, respectively. Normalized with the displacement body diameter, the streamwise extent of the computational domain measured from the center of the displacement body was 1.5D in upstream direction and 3.9D in downstream direction.

The height $y_{max}$ of the computational domain was varied between 0.048m and 0.068m. To investigate the influence of the spanwise domain width on the flow (Sec. 4.3.1), domain widths from 0.24m to 1.28m, i.e. from W = 1.2 to W = 12.8 body diameters, were investigated.

The grid for the steady simulations (i.e. for simulations where the Reynolds number is low enough so that the flow remained steady) had a resolution of $1\times10^{-3}$m in the streamwise direction. In the wall-normal direction, 129 or 161 points were used depending on $y_{max}$ with a mild exponential grid point clustering near the wall to adequately resolve the boundary layer on the flat plate as well as the developing shear layer and vortices. The stretching was adjusted such that the near wall resolution for the different $y_{max}$ was similar for the different cases and about half of the grid points were located in the lower 30% of the domain. The wall normal grid resolution at the wall was about $1.2\times10^{-4}$m. The boundary layer and separation bubble were resolved with 30–40 points. A higher-resolution grid was obtained by doubling the number of grid points in both the streamwise and the wall-normal direction, resulting in a streamwise resolution of $0.5\times10^{-3}$m and a near-wall grid-line spacing of $0.6\times10^{-4}$m. In the spanwise direction, between 61 and 321 modes were employed, which corresponds to 193 and 1025 collocation points, respectively, across the full physical spanwise domain width. This results in a spanwise resolution of $1.25\times10^{-3}$m for the lower-resolution grid and $0.625\times10^{-3}$m for the higher-resolution grid. For the unsteady simulations, we utilized the higher-resolution grid with 257 points in the wall-normal, 1281 points in the streamwise and up to 641 modes in the spanwise direction (337 million points total). The minimum grid resolution in wall units in the wake was $x^+ \approx 13$, $y^+ \approx 1.9$, and $z^+ \approx 9$.

### 4.3 Results

To gain a basic understanding of the topology of the 3-D separation, several steady flow cases were investigated first. In this chapter, the flow topologies for these steady flow cases as well as for the time-averaged flowfields obtained from simulations at larger Reynolds numbers, where the flow is unsteady, are presented. The unsteady features of the latter are described in Sec. 4.4 and the flow structures for all cases are discussed in more detail in Sec 4.5.

The flow topologies were analyzed based on the limiting streamline pattern on the flat plate and streamlines in the symmetry plane (Figs. 4.4-4.8). The limiting streamlines were overlayed with contours of spanwise vorticity on the plate and streamwise velocity in the symmetry plane ($z = 0$) to indicate the reverse flow region, which corresponds to negative values of vorticity and streamwise velocity, respectively. As suggested by Pauley (1994), the limiting streamline patterns were computed from the wall-tangential velocity components at the wall nearest grid points. In general, this worked very well and the constructed streamline patterns are in very good agreement with the flowfield as indicated by the wall vorticities.

#### 4.3.1 Effect of Domain Width

As discussed in Sec. 3.1.1, in the DNS code periodicity in the spanwise direction is assumed. Therefore, the first step was to analyze the effect of the domain width (W) on the potential flow field (Fig. 4.3) and on flow separation (Fig. 4.4). The spanwise periodicity implies that the simulated scenario is not a single separation bubble, but an infinite row of separation bubbles, or, in other words, an infinite row of displacement bodies. The test section side walls of the water tunnel can also be regarded as symmetry planes, which for potential flow can be modeled by adding images of the displacement body in the spanwise direction. The spanwise periodicity in the DNS is therefore consistent with the accompanying experiments. A domain width of $w = 0.64$m or $W = 6.4$ (in displacement body diameters) was chosen as the baseline case, as this is close to the spanwise width of the test section in the water tunnel (Sec. 3.2) and because this results in an inviscid pressure distribution on the flat plate that closely resembles that for a single displacement body (Fig. 4.3).

The domain width mostly affects the spanwise $C_p$ gradient with little effect on the streamwise pressure gradient (Tab. 4.1), and, therefore, allows us to investigate the influence of the spanwise pressure distribution on the separation topology.

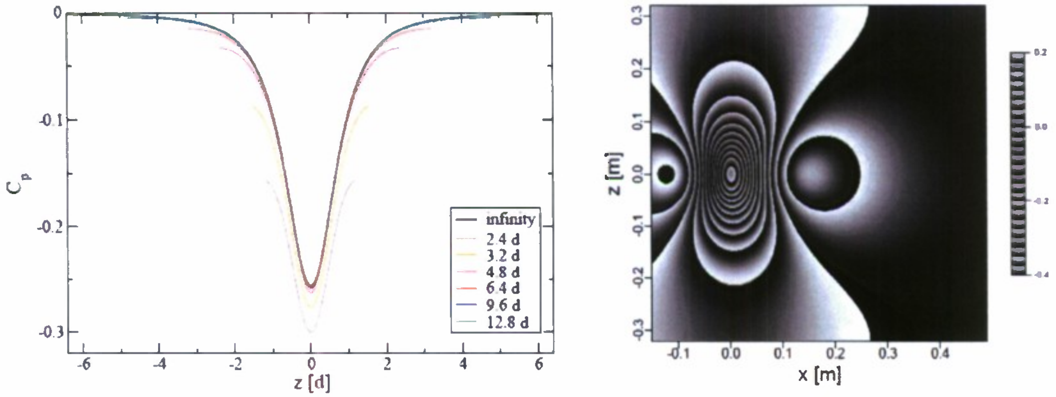

(a) Effect of distance to "neighboring" displacement bodies on the spanwise $C_p$ distribution. Profiles shown are plotted at the downstream location of minimum $C_p$.

(b) Illustration of the shape of $C_p$ for reference case $d = 0.1m, H = 1.0, W = 6.4$

*Fig. 4.3: Non-dimensional, inviscid pressure distribution $C_p$ on flat plate.*

The analysis of the limiting streamline patterns (Fig. 4.4) reveals that the width and, most importantly, the topology of the separation are greatly affected by the spanwise extent of the domain. For all domain widths from W = 2.4 to W = 6.4, the topology of the flow for $Re_D$ = 7,500 and H = 1.0 shows one saddle point associated with flow separation at the upstream end of the separation bubble. From this saddle point the line of primary separation leads to a focus on either side of the symmetry plane and a saddle point of attachment at the downstream end of the separated region (Figs. 4.4a,b).

When the domain width is increased, the saddle point of attachment splits in two. These two separate saddle points move away from the symmetry plane, where a node now replaces the original single saddle point. Along with this, a region develops adjacent to the symmetry plane inside and downstream of the separation bubble, where the limiting streamlines originate from this node of attachment (Figs. 4.4c,d). For the two widest domains that we considered, the topology of the separation bubble remains unchanged. This is, because the inviscid pressure distribution on the flat plate (Fig. 4.3a) for the maximum simulated domain width W = 12.8 is essentially identical to the pressure distribution for a domain with infinite spanwise extent. Very similar results are obtained for a spanwise domain width of W = 9.6. Although the difference in the spanwise inviscid pressure distribution for W = 2.4 and W = 6.4 is much larger than the difference seen for W = 6.4 and W = 9.6 (Fig. 4.3a), the change in topology is less significant for W = 2.4 and W = 6.4 than for W = 6.4 and W = 9.6. The streamlines in the symmetry plane exhibit the same general pattern for all cases and are not affected by the domain width.

| index | $H$ | $W$ | $Re_d$ | $Re_{\theta,sep}$ | $\Delta C_{p,inv.}/\Delta X$ | $\Delta C_{p,inv.}/\Delta Z$ |
|---|---|---|---|---|---|---|
| i | 1.00 | 3.2 | 7,500 | 102 | 0.197 | 0.118 |
| ii | 1.00 | 4.8 | 7,500 | 100 | 0.198 | 0.096 |
| iii | 1.00 | 6.4 | 7,500 | 99 | 0.197 | 0.076 |
| iv | 1.00 | 9.6 | 7,500 | 98 | 0.200 | 0.053 |
| v | 1.00 | 12.8 | 7,500 | 98 | 0.199 | 0.040 |
| vi | 1.02 | 6.4 | 7,500 | 103 | 0.185 | 0.071 |
| vii | 1.05 | 6.4 | 7,500 | 107 | 0.167 | 0.065 |
| viii | 1.10 | 6.4 | 7,500 | 117 | 0.142 | 0.057 |
| ix | 1.15 | 6.4 | 7,500 | — | 0.121 | 0.049 |
| x | 1.00 | 6.4 | 2,500 | — | 0.197 | 0.076 |
| xi | 1.00 | 6.4 | 5,000 | 88 | 0.197 | 0.076 |
| xii | 1.00 | 6.4 | 15,000 | 132 | 0.197 | 0.076 |

| index | $L_{bubble}$ | $W_{bubble}$ | $H_{bubble}$ | Topology |
|---|---|---|---|---|
| i | 1.49 | 0.52 | 0.044 | 2 SP, 2 F |
| ii | 1.53 | 0.54 | 0.059 | 2 SP, 2 F |
| iii | 1.58 | 0.58 | 0.063 | 2 SP, 2 F |
| iv | 1.60 | 0.64 | 0.065 | 3 SP, 2 F, 1 N |
| v | 1.61 | 0.68 | 0.065 | 3 SP, 2 F, 1 N |
| vi | 1.26 | 0.52 | 0.045 | 2 SP, 2 N |
| vii | 1.14 | 0.50 | 0.037 | 1 SP, 1 N |
| viii | 0.62 | 0.30 | 0.010 | 1 SP, 1 N |
| ix | — | — | — | no separation |
| x | — | — | — | no separation |
| xi | 0.81 | 0.38 | 0.028 | 1 SP, 1 N |
| xii | $\approx$1.82 | 0.88 | 0.069 | 3 SP, 2 F, 1 N |

*Tab. 4.1: Summary of simulation parameters (top) and separation bubble characteristics (bottom; SP = saddle point, F = focus, N = node).*

### 4.3.2 Effect of Displacement Body Distance from Flat Plate

The distance of the displacement body from the flat plate affects the pressure distribution on the flat plate. While the spanwise domain width mostly affects the spanwise pressure distribution, the parameter H (defined as the displacement body distance from the flat plate) was found to affect both the streamwise and spanwise pressure gradient.

For the simulations shown in Fig. 4.5, the displacement body was successively moved farther away from the flat plate, thus weakening the pressure gradients acting on the boundary layer on the flat plate. When comparing the separation topology for increased distances H relative to the reference case with H = 1.0 in Fig. 4.4b ($Re_D$ = 7, 500, W = 6.4), it can be seen that as H is increased, the saddle point of reattachment remains in the symmetry plane, whereas the saddle point of separation is replaced by a node of separation and the two foci vanish. This topology appears to remain stable until the pressure gradient becomes too weak and the separation disappears altogether (Fig. 4.5d).

A closer look at the streamline patterns for H = 1.02 and H = 1.05 (see Fig. 4.6) reveals a slight but important difference, which is seen most clearly in the color contours of streamwise vorticity near the line of separation. For H = 1.05 the line of zero streamwise vorticity (indicated by the white color) is found downstream of the line of separation, whereas for H = 1.02 it is located upstream of the line of separation. This difference is crucial, as it indicates that for H = 1.02 the streamlines converging on the line of separation lead away from the symmetry plane (same as for H = 1.0), while for H = 1.05 they point towards the symmetry plane. Consequently, the singular point in the symmetry plane from which the line of separation emanates, must be a saddle point for H = 1.02, and a node for H = 1.05. Since the point of attachment is also clearly a saddle point (in both cases), there must be nodes or foci at the outer ends of the line of separation for H = 1.02, according to the topological rules first proposed by Lighthill [1963]. [1]

As nothing suggests a "spiral" motion close to the end of the line of separation, the points are identified as a pair of nodes. In the cases (with separation) where no foci are present (Figs. 4.5a-c), the line of separation has no definite end point. (This fact necessitates an alternative definition for the width of the separated flow region [Jacobi et al. 2008]). The lack of definite end points of the line of separation also represents a unique property of 3-D separation called "open separation", which is discussed in more detail in Sec. 4.3.4. The general pattern of the streamlines in the symmetry plane is again not affected by the changes seen in the limiting streamline pattern on the flat plate.

---

[1] *Upon close examination of the streamlines for H = 1.02, one can see that near the outer end of the line of separation the streamline direction is not in agreement with the flow direction suggested by the wall-vorticity. The streamwise vorticity indicates flow away from the symmetry plane (red), where the streamlines turn towards the symmetry plane. The line of separation still ends in a node, as indicated both by the streamline behavior and the wall-vorticity. The discrepancy can be attributed to the fact that the streamline pattern was computed from flow data at a finite distance from the plate, which may differ from the flow field "right on" the surface. Such a difference has been observed for this case only.*

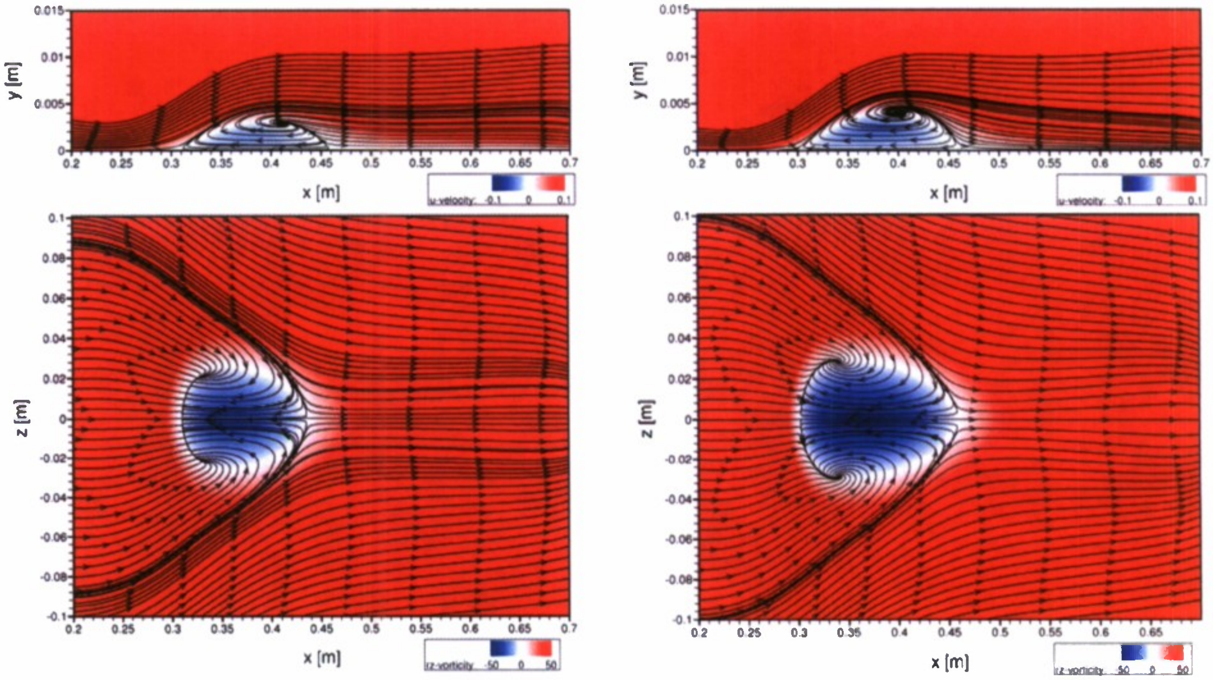

*(a)* $Re_D = 7{,}500,\ W = 3.2,\ H = 1.0$ *(b)* $Re_D = 7{,}500,\ W = 6.4,\ H = 1.0$

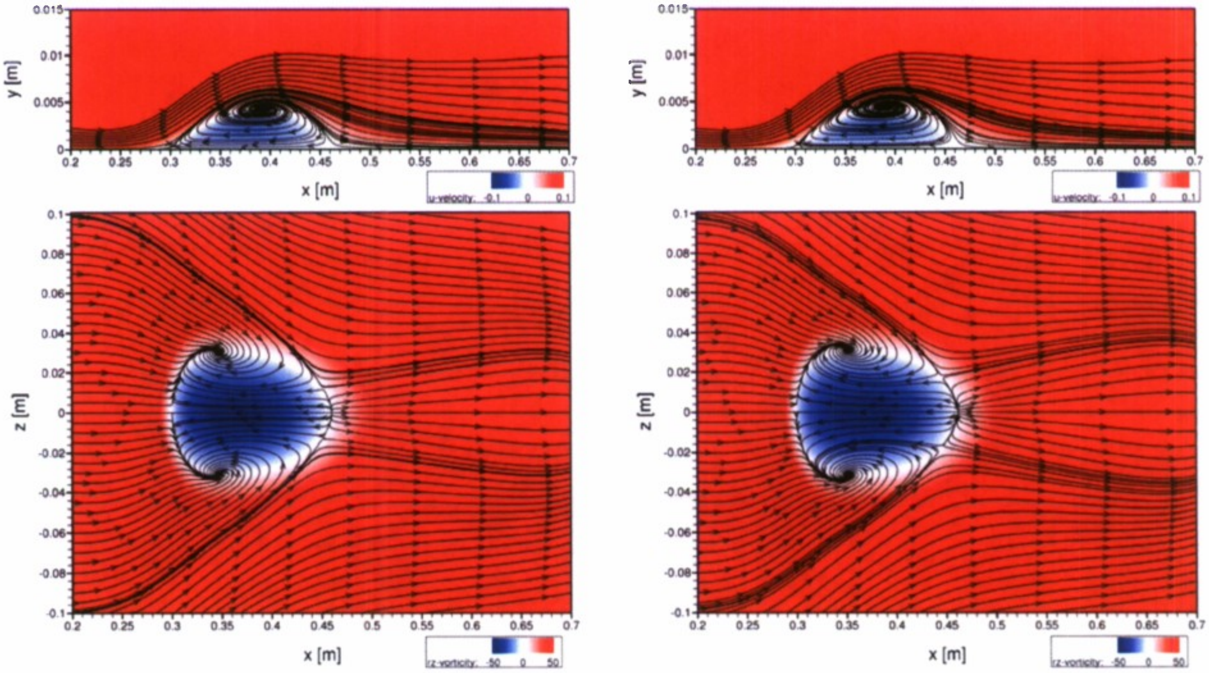

*(c)* $Re_D = 7{,}500,\ W = 9.6,\ H = 1.0$ *(d)* $Re_D = 7{,}500,\ W = 12.8,\ H = 1.0$

*Fig 4.4: Effect of spanwise domain width, W, on separation topology.*
*Shown are streamline patterns and color contours of streamwise velocity in the symmetry plane (z=0, on top), and limiting streamlines and color contours of spanwise vorticity on the plate (y=0, below). Blue indicates reverse flow.*

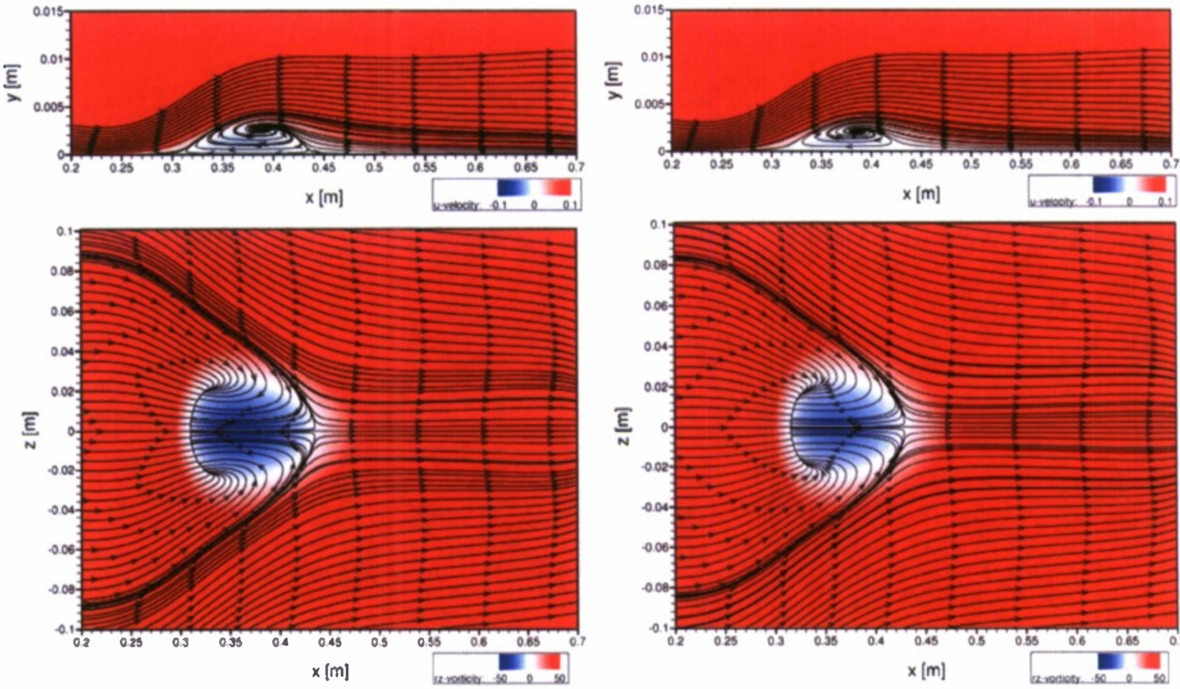

*(a) $Re_D = 7{,}500$, $W = 6.4$, $H = 1.02$*

*(b) $Re_D = 7{,}500$, $W = 6.4$, $H = 1.05$*

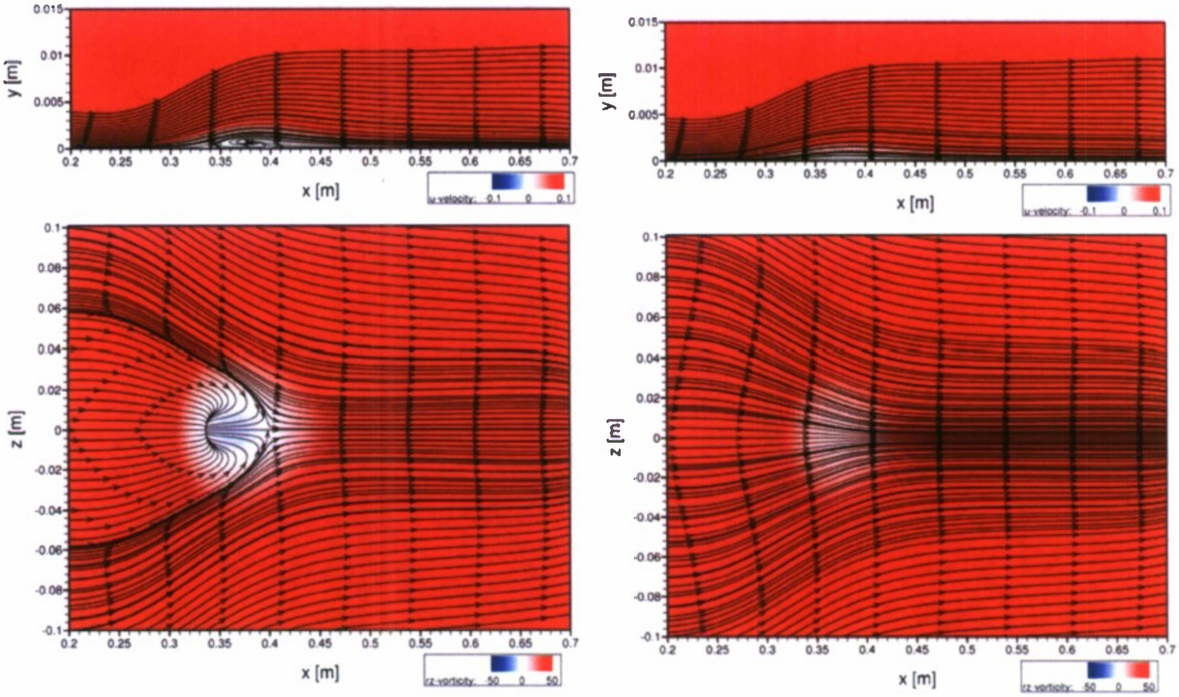

*(c) $Re_D = 7{,}500$, $W = 6.4$, $H = 1.10$*

*(d) $Re_D = 7{,}500$, $W = 6.4$, $H = 1.15$*

*Fig 4.5: Effect of distance of displacement body from flat plate, H, on separation topology. Shown are streamline patterns and color contours of streamwise velocity in the symmetry plane (z=0, on top), and limiting streamlines and color contours of spanwise vorticity on the plate (y=0, below). Blue indicates reverse flow.*

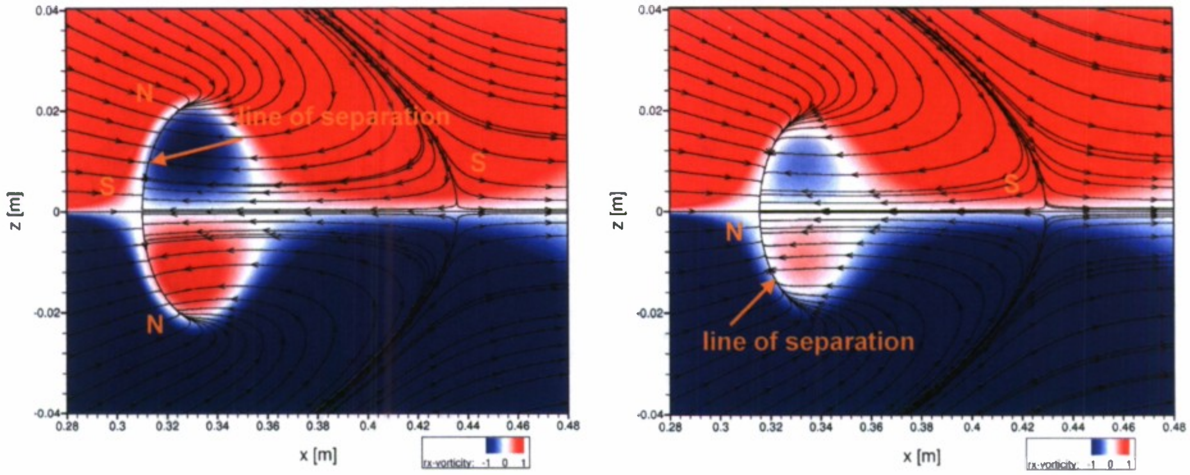

*Fig 4.6: Enlarged views of the separated region. Shown are limiting streamline patterns overlayed with color contours of streamwise vorticity on the flat plate (y = 0). Blue indicates flow going "upwards" (in positive z-direction), red indicates flow going "downwards" (in negative z-direction).*

### 4.3.3 Effect of Reynolds Number

A wide range of Reynolds numbers $Re_D$ (based on displacement body diameter and freestream velocity) between 2,500 and 30,000, were investigated for a fixed spanwise domain width W = 6.4 and distance of the displacement body from the flat plate H = 1.0. The separated flow is steady up to a Reynolds number of 10,000, it is unsteady for $Re_D$ = 11,000, 15,000, and 30,000. For the unsteady cases, the flow topologies were deduced from the time-averaged flowfields.

Fig. 4.7 shows the streamline pattern in the symmetry plane and on the flat plate for the steady cases. For $Re_D$ = 5,000 (Fig. 4.7b) the flow topology is the same as for some of the cases where the height of the displacement body was increased (Figs. 4.5b,c). The limiting streamline pattern on the flat plate only contains one node of separation and one saddle point of reattachment, and the line of primary separation shows the same "open separation behavior" as described in Sec. 4.3.2 for H = 1.05. (For $Re_D$ = 2,500 and H = 1.0, as well as for $Re_D$ = 7,500 and H = 1.15, the flow did not separate from the flat plate.)

The streamline patterns for increased displacement body distances H and decreased Reynolds numbers $Re_D$ are similar. Varying the Reynolds number $Re_D$, however, does not directly affect the non-dimensional inviscid pressure distribution $C_{p,inv}$, as it is independent of the freestream velocity. Thus, for reproducing a particular experiment, both Reynolds number and $C_p$ have to be matched. Nevertheless, the simulations show that it is possible to—at least qualitatively—duplicate the flow behavior at a different Reynolds number, if the $C_p$ distribution imposed on the flat plate is adequately adjusted.

For the unsteady cases, the time-averaged flowfields shown in Fig. 4.8a-c indicate topologies that to some extent differ from the reference case with $Re_D$ = 7,500 and W = 6.4, but also share some commonalities with the $Re_D$ = 7,500 cases with large domain widths: For example, the line of primary separation connects a saddle point of separation with two focal points, although the foci are much stronger for the higher Reynolds numbers. Also, the width of the bubble, as determined by the spanwise extrema of the line of primary separation, is considerably larger. While the saddle point of separation is seen to move upstream with increasing Reynolds number, the location of the foci remains almost unchanged, compared to the reference case.

The attachment regions of the time-averaged flowfields exhibit a topology that is not easily interpreted, but qualitatively similar. A node of attachment is located in the symmetry plane with a saddle point on either side (Fig. 4.8a-c). The node of attachment is necessitated by the theorem governing the number of singular points, provided one accepts the notion that the singular points away from the symmetry plane are saddle points [Lighthill 1963].

Compared to the topology of a separation bubble at $Re_D = 7{,}500$ ($W = 12.8$, Fig. 4.4d), which displays an equal number and arrangement of singular points, the node of attachment in the unsteady cases appears to be rotated by 90 degrees, and the streamline patterns near the symmetry plane and downstream of the point of reattachment differ. Figure 4.8 also shows that at least one line of secondary separation emanates on either side of the symmetry plane from the saddle points downstream of the separation bubble. Note that for all the cases which we investigated this is the only indication of a secondary separation.

The difference in the separation topology between the unsteady and steady cases, which shows up in the streamline patterns in the symmetry plane, can also be seen in Fig. 4.10. Whereas for the steady reference case the shear layer in the symmetry plane stays detached from the wall (Fig. 4.10a), for the unsteady cases the flow reattaches for the time-averaged flow field (Fig. 4.10b-d). This is discussed in more detail in Sec. 4.4.

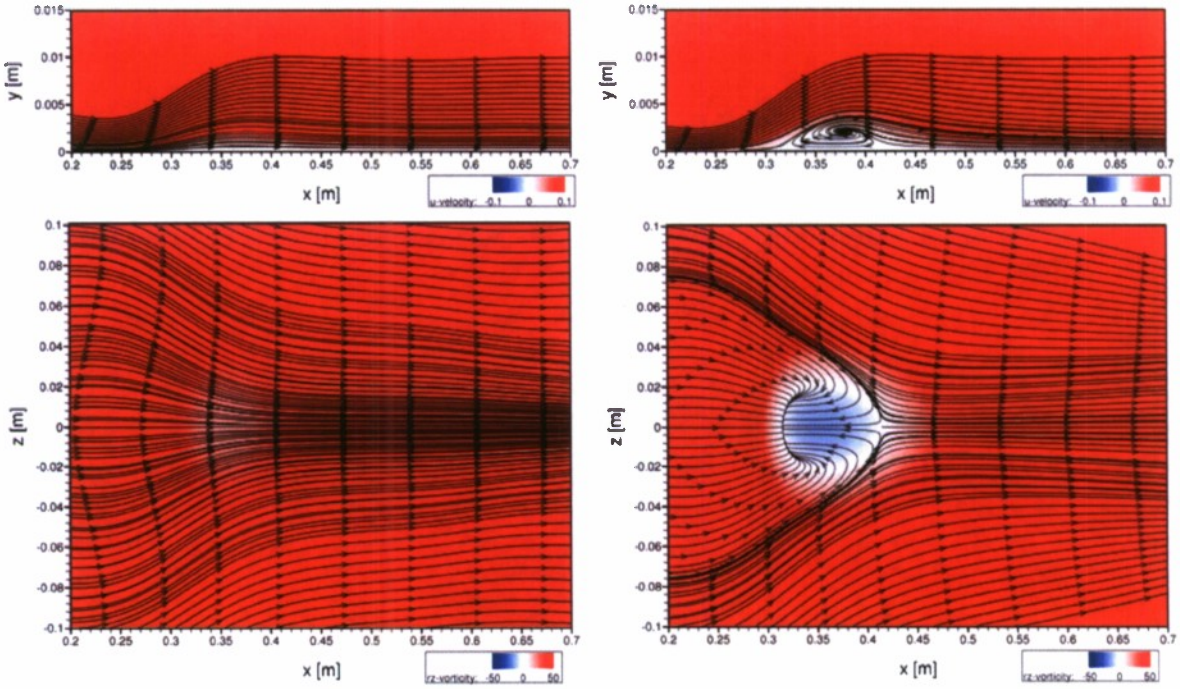

*(a) $Re_D$ = 2,500, W = 6.4, H = 1.0*

*(b) $Re_D$ = 5,000, W = 6.4, H = 1.0*

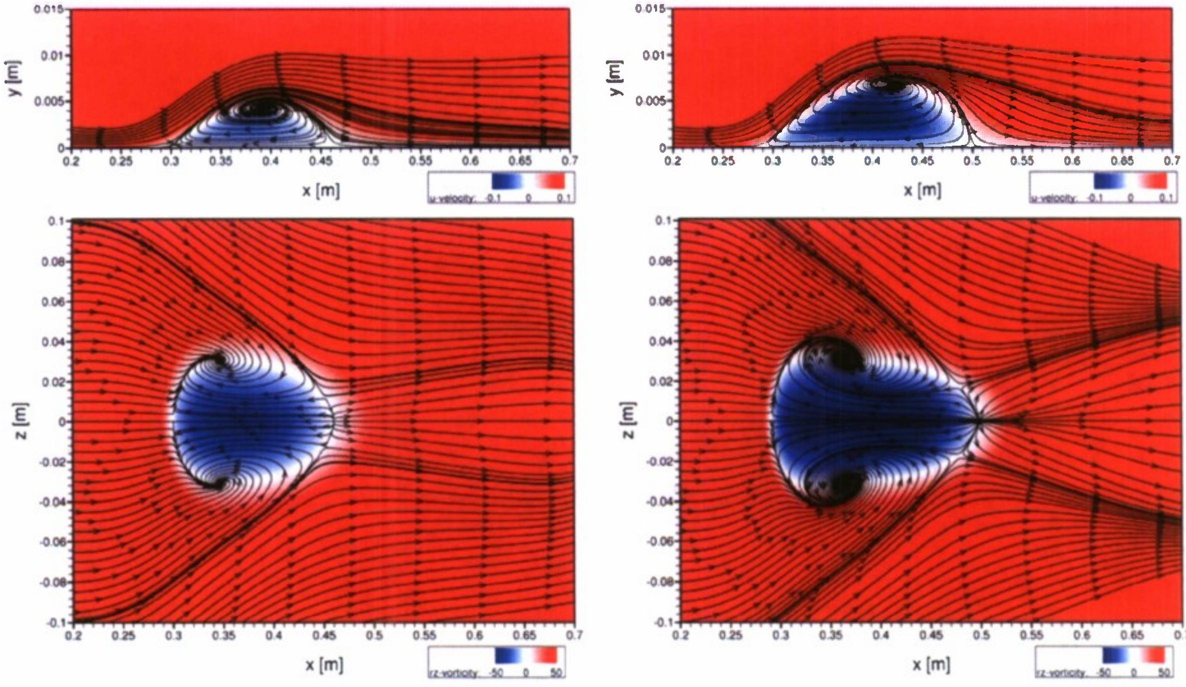

*(c) $Re_D$ =7,500, W = 6.4, H = 1.0*

*(d) $Re_D$ = 10,000, W = 6.4, H = 1.0*

*Fig 4.7: Effect of Reynolds number $Re_D$ on separation topology (steady cases).*
*Shown are streamline patterns and color contours of streamwise velocity in the symmetry plane (z=0, on top), and limiting streamlines and color contours of spanwise vorticity on the plate (y=0, below). Blue indicates reverse flow.*

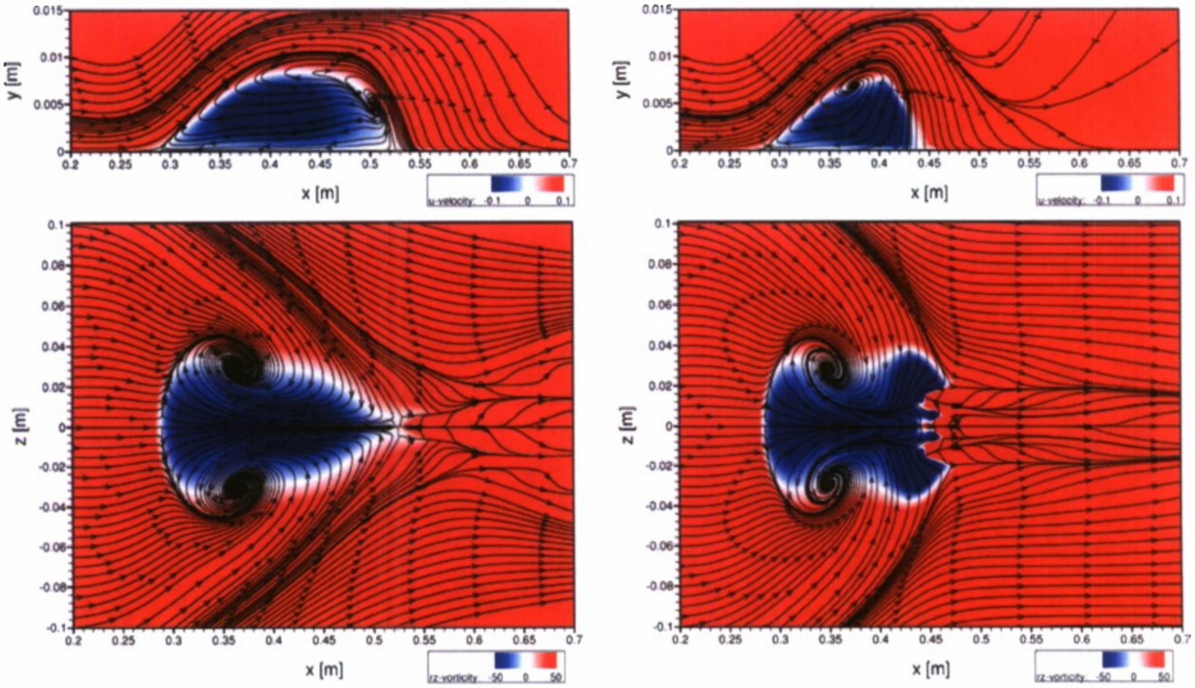

*(a) $Re_D$ = 11,000, W = 6.4, H = 1.0 (time-average)*

*(b) $Re_D$ = 15,000, W = 6.4, H = 1.0 (time-average)*

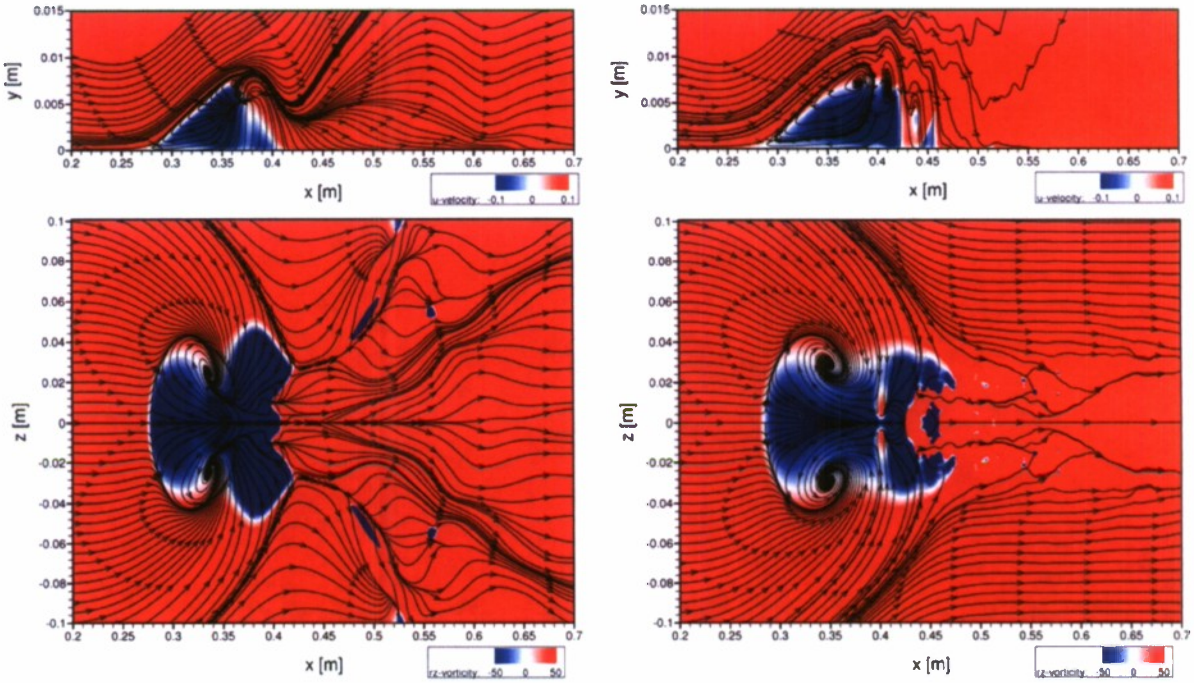

*(c) $Re_D$ =30,000, W = 6.4, H = 1.0 (time-average)*

*(d) $Re_D$ = 15,000, W = 6.4, H = 1.0 (instantaneous)*

*Fig 4.8: Effect of Reynolds number $Re_D$ on separation topology (unsteady cases).*
*Shown are streamline patterns and color contours of streamwise velocity in the symmetry plane (z=0, on top), and limiting streamlines and color contours of spanwise vorticity on the plate (y=0, below). Blue indicates reverse flow.*

### 4.3.4 Flow Topology

Foci in the limiting streamline patterns are the roots of so-called "horn vortices", as described in Sec. 1. The topologies observed for H = 1.0 and Reynolds numbers greater than 5,000 contain a pair of foci at either end of the line of separation. It is important to point out that this is the case for both, the steady and unsteady cases. Furthermore, for all cases that we investigated the streamline pattern in the symmetry plane displays vortical structures with reverse flow near the surface.

Insight into the interaction between the two horn vortices associated with the foci on the flat plate and the spanwise vortex associated with the reverse flow in the symmetry plane can be gained from 3-D streamlines (Fig. 4.9a,b). Fig. 4.9b also includes a visualization of the vortex core, which we extracted using the method of Kenwright and Haimes [1997]. The vortex core extends from the foci upwards and towards the mid-span plane. Judging from the visualizations in Fig. 4.9, the horn vortices appear to connect with the spanwise vortex. The 3-D streamlines exhibit a strong "swirling motion" induced by the horn vortices and also illustrate how the flow is ingested on the sides and then ejected near the top of the separation bubble close to the symmetry plane.

When analyzing the flowfield in cross-flow planes at different downstream locations, no streamwise vortical structures could be identified in the separated region. However, as shown in Fig. 4.9c, the velocity vectors at locations downstream of the separation bubble seem to indicate the existence of a pair of streamwise vortices close to the surface.

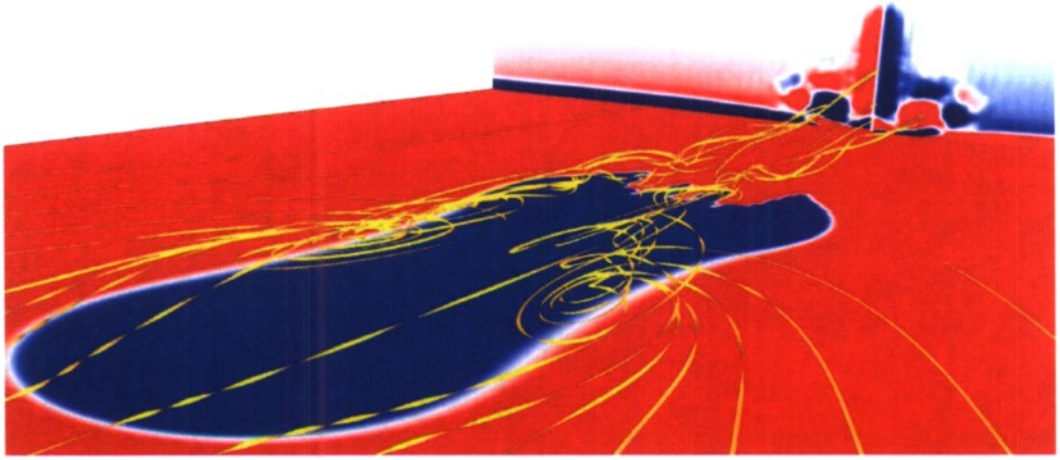

*(a) Perspective view of 3-D streamlines and color contours of spanwise vorticity on the plate obtained from time-averaged flow data for* $Re_D = 15{,}000$*,* $W = 6.4$*, and* $H = 1.0$ *(blue indicates reverse flow).*

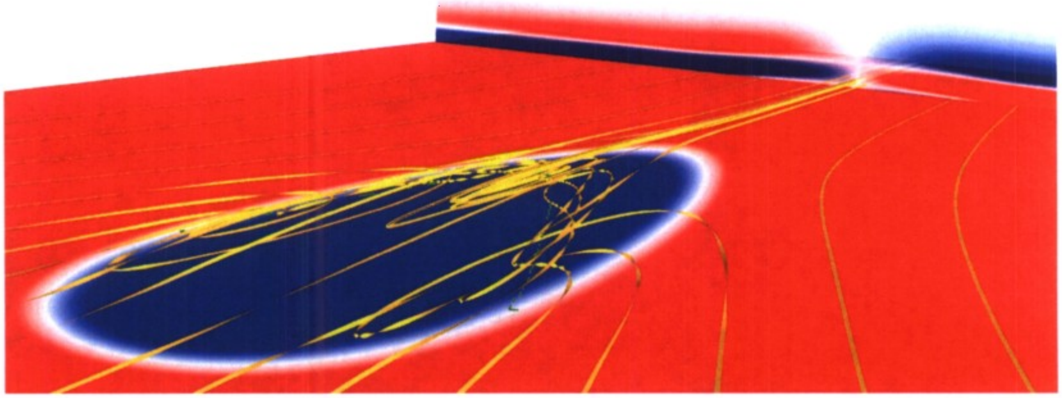

*(b) Perspective view of 3-D streamlines and color contours of spanwise vorticity on the plate for* $Re_D = 7{,}500$*,* $W = 12.8$*, and* $H = 1.0$ *(steady; blue indicates reverse flow).The green line represents the vortex core [Kenwright & Haimes 1997].*

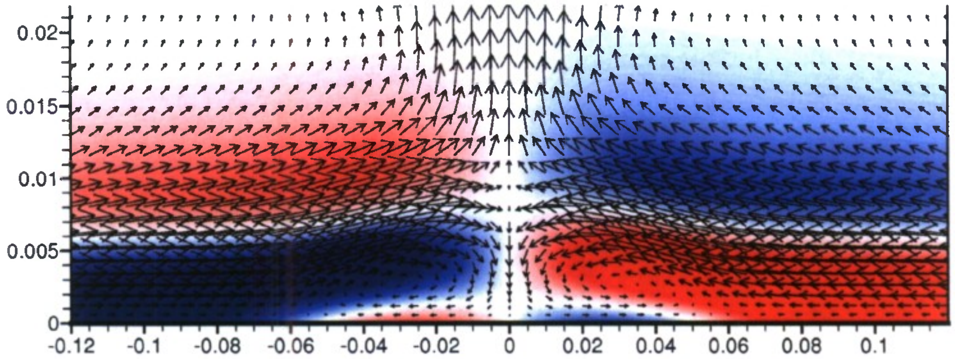

*(c) Cross-flow visualization for* $Re_D = 7{,}500$*,* $W = 12.8$*, and* $H = 1.0$ *downstream of separated region at* $x = 0.6$*m looking downstream. Velocity vectors and color contours of streamwise vorticity (red - counter-clockwise rotation, blue - clockwise rotation).*

*Fig 4.9: Flow visualizations. Cross-flow planes are colored with isocontours of streamwise vorticity (red - counter-clockwise rotation, blue - clockwise rotation).*

## 4.4 Results: Unsteady Separation Phenomena

Fig. 4.10 shows isocontours of spanwise vorticity in the mid-span plane, for the time-averaged flowfield of the unsteady cases and for one exemplary steady case ($Re_D$ =10,000). For all steady cases, the separated shear layer does not reattach to the flat plate. For the unsteady cases, however, the shear layer reattaches in the mean. Another interesting observation is that as the Reynolds number is increased, the reattachment point moves upstream, resulting in a gradual reduction of the length of the separation bubble. A possible explanation is provided by Fig. 4.11, which shows instantaneous visualizations of the spanwise vorticity in the mid-span plane for the unsteady cases. The separation bubble sheds spanwise vortical structures, which break up into smaller scale structures, leading to transition, and eventually reattachment in the mean. These structures are likely a consequence of hydrodynamic instabilities of the flow and thus highly dependent on the flow conditions. As the Reynolds number is increased from 11,000 to 30,000, the separated boundary layer "rolls up" earlier and the flow transitions farther upstream, resulting in a shortening of the separation bubble. With increasing Reynolds number, the size of the smallest structures is reduced, as the turbulent energy cascade extends over a larger wave number range. In addition, the wake is seen to spread more quickly in the spanwise direction. The question whether the primary instability is convective or absolute has yet to be addressed. Transition not only results in an earlier closing of the separation bubble but also affects the instability mechanisms itself, since the time-average or base flow is altered. In summary, the complicated interplay between separation and transition determines the separation bubble characteristics.

Wake visualizations are provided in Fig. 4.12, where isosurfaces of the Q vortex identification criterion [Hunt et al. 1988] are shown. Strong coherent structures which propagate in downstream direction can clearly be identified. The structures have a strong periodicity in the streamwise direction, even for $Re_D$ = 30,000. Similar structures were observed for two-dimensional separation bubbles (e.g. Postl 2005). These large-scale spanwise coherent structures are mainly responsible for the transport of high-momentum fluid from the freestream towards the wall, which ultimately results in reattachment of the flow.

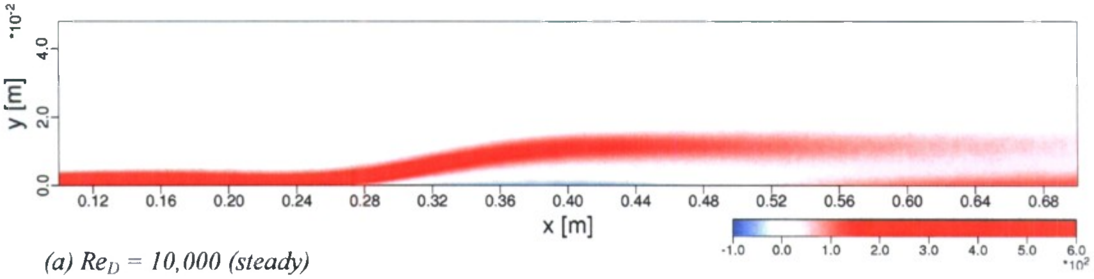

(a) $Re_D$ = 10,000 (steady)

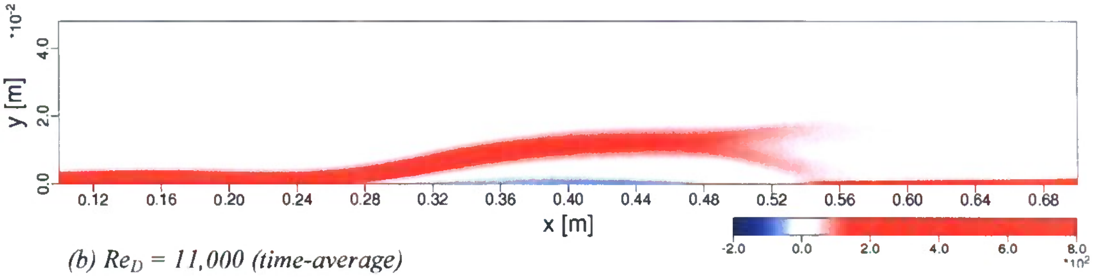

(b) $Re_D$ = 11,000 (time-average)

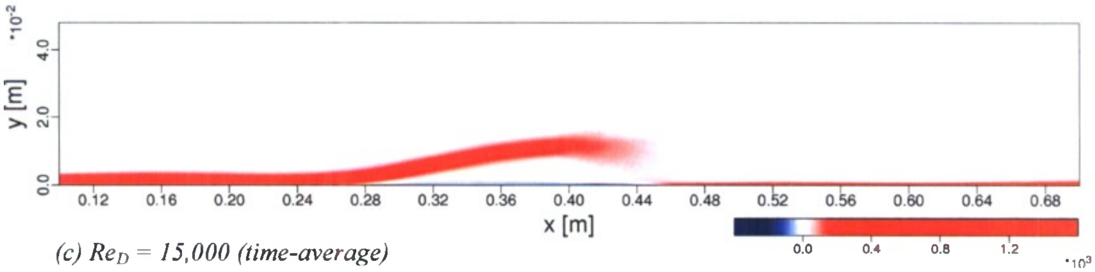

(c) $Re_D$ = 15,000 (time-average)

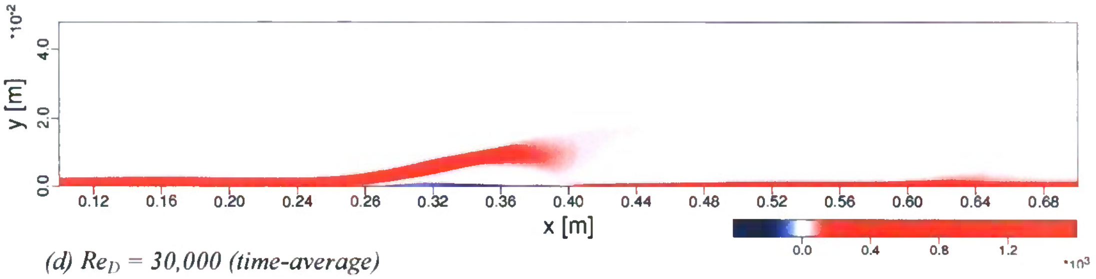

(d) $Re_D$ = 30,000 (time-average)

*Fig 4.10: Comparison of spanwise vorticity in the mid-span plane for steady and unsteady separation (for the latter obtained from the time-averaged flow data; red - counter-clockwise rotation, blue - clockwise rotation).*

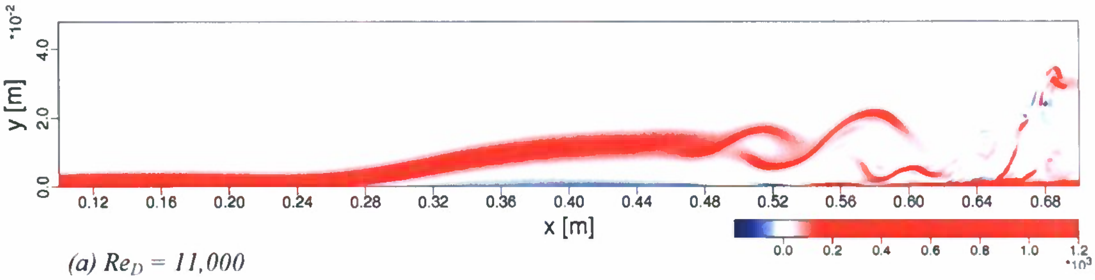

(a) $Re_D = 11{,}000$

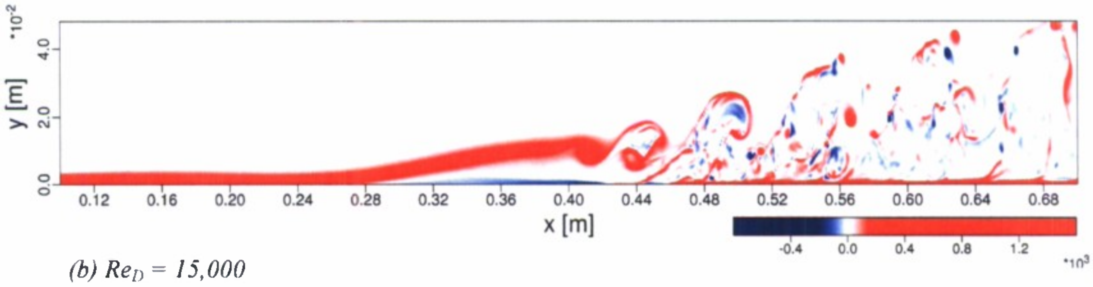

(b) $Re_D = 15{,}000$

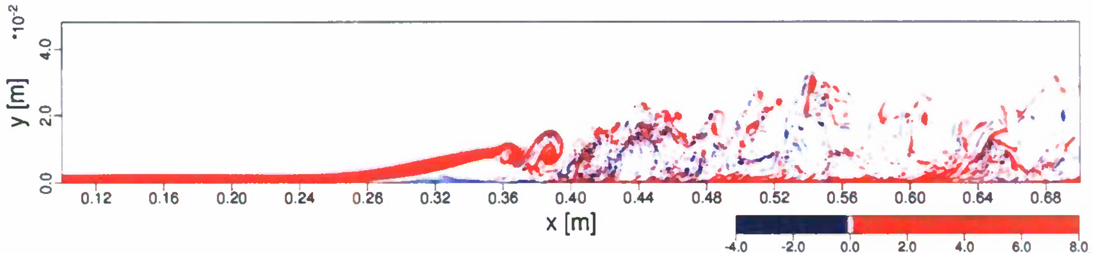

(c) $Re_D = 30{,}000$

*Fig 4.11: Comparison of instantaneous spanwise vorticity in the mid-span plane for cases with unsteady separation (red - counter-clockwise rotation, blue - clockwise rotation).*

(a) $Re_D = 11{,}000$ ($Q=1000$)

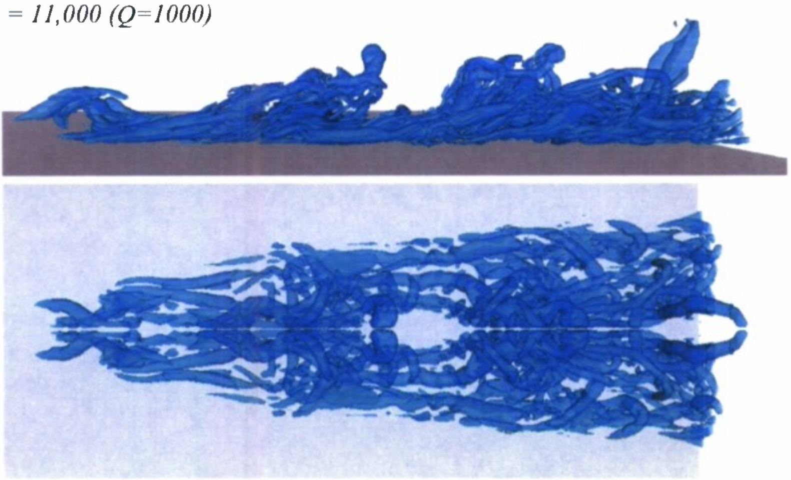

(b) $Re_D = 15{,}000$ ($Q=6000$)

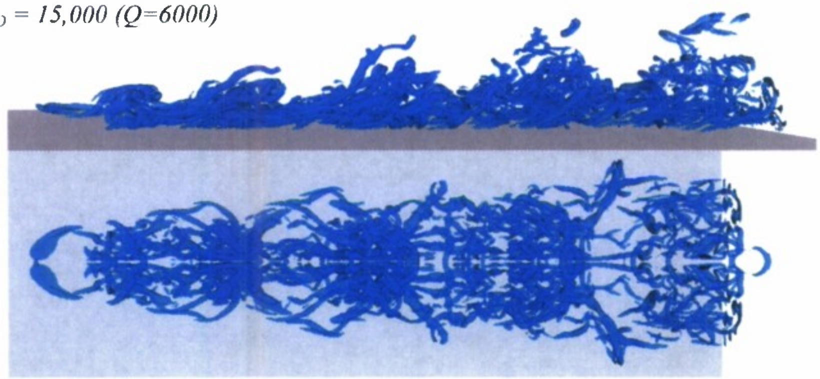

(c) $Re_D = 30{,}000$ ($Q=6000$)

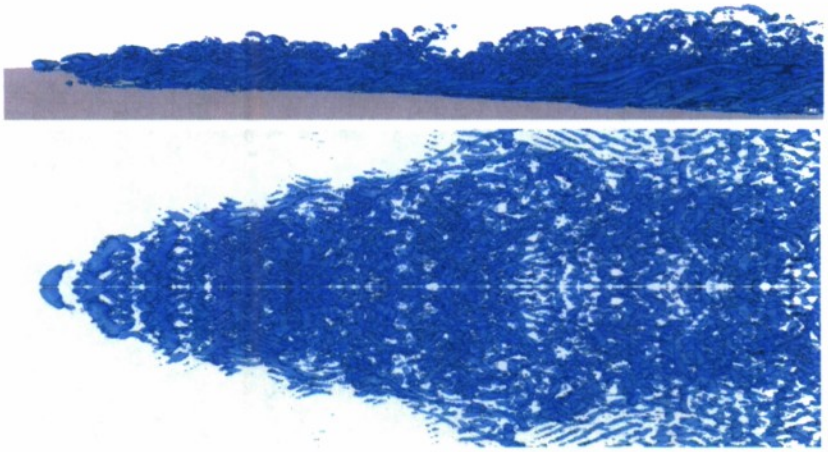

*Fig 4.12: Visualization of vortical structures in the wake of the separation bubble. Shown are isosurfaces of the Q vortex identification criterion.*

### 4.3.6 Comparison to Two-Dimensional Separation Bubbles

Although the visualizations of spanwise vorticity in the symmetry plane provided in Fig. 4.10 are reminiscent of similar visualizations for two-dimensional separation bubbles, the streamline patterns in the symmetry plane (Figs. 4.4-4.8) are evidence that no closed recirculation region exists for the steady scenarios that we investigated. The fluid entrained into the separation bubble from the sides is ejected at the top of the bubble. This demonstrates a fundamental difference between two- and three-dimensional separation bubbles. For two-dimensional bubbles, the separated boundary layer must eventually reattach, thus forming a closed recirculation region. However, in three dimensions, the attached flow downstream of the separated region does not require a closed recirculation in the symmetry plane, as fluid may enter the reverse flow region from the sides. For the steady separation scenarios the dividing streamsurface originating from the line of primary separation never reattaches (within the computational domain). Rather, the attached flow downstream of the separated region consists of fluid that is being entrained from the sides. However, in the unsteady cases depicted in Fig. 4.10c-d, the shear layer of the time-averaged flow field reattaches just as for a two-dimensional separation bubble. This may be a consequence of the large-scale, unsteady spanwise coherent structures, as discussed in Sec. 4.4.

### 4.3.7 Comparison to Flow over Hemisphere-Cylinder

The wall skin-friction line topology suggested by Tobak and Peake [1979] for the separation bubble at the nose, or "nose bubble" of a hemisphere-cylinder at low to intermediate angles of attack is depicted in Fig. 4.13. It features a saddle point of separation from which a separation line leads to a pair of focal points. Two saddle points and a node of attachment in the symmetry plane are seen in the rear of the bubble. The foci are the roots of two "horn vortices. Lines of secondary separation emerge from the saddle points at either side of the symmetry plane and extend downstream.

Our results for the unsteady cases (Fig. 4.8) are similar to the limiting streamline topology proposed by Tobak and Peake for the hemisphere-cylinder, including the secondary separation. For the steady cases, only the topologies for W = 12.8 and W = 9.6 (Fig. 4.4c,d) feature the same singular points. Both cases, however, lack any secondary separation.

The cross-flow pattern reported by Hsieh and Wang [1996] for flow over a hemisphere-cylinder (Fig. 4.14) features two streamwise recirculation regions downstream of the nose bubble that can be associated with the cross-flow component of the approach flow. These recirculation regions are similar to those seen in our simulations of 3-D separation bubbles (Fig. 4.9).

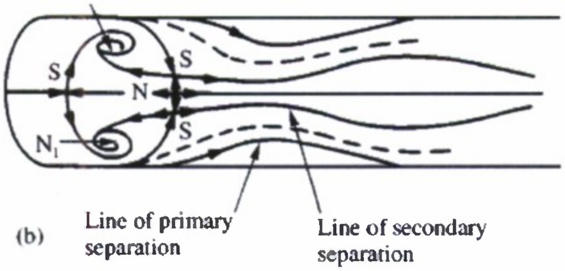
S
S
N
S
N1
(b)
Line of primary separation
Line of secondary separation

*Fig. 4.13: Skin-friction line topology for flow over hemisphere cylinder [Tobak and Peake 1979].*

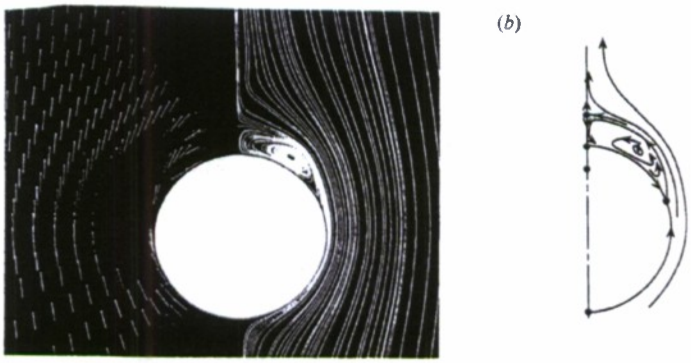

*Fig. 4.14: Cross-flow visualizations for flow over hemisphere-cylinder [Hsieh and Wang 1996].*

# 5. SEPARATION BUBBLE: WATER TUNNEL EXPERIMENTS

## 5.1 Experimental Setup

In parallel with the numerical investigations, we conducted water tunnel experiments for the same geometry. We considered Reynolds numbers between $Re_D$= 5,000 and $Re_D$=15,000 based on the diameter of the displacement body D. A schematic of the experimental setup is provided in Fig. 5.1. Boundary layer suction was applied on the surface of the displacement body to prevent flow separation on the body itself.

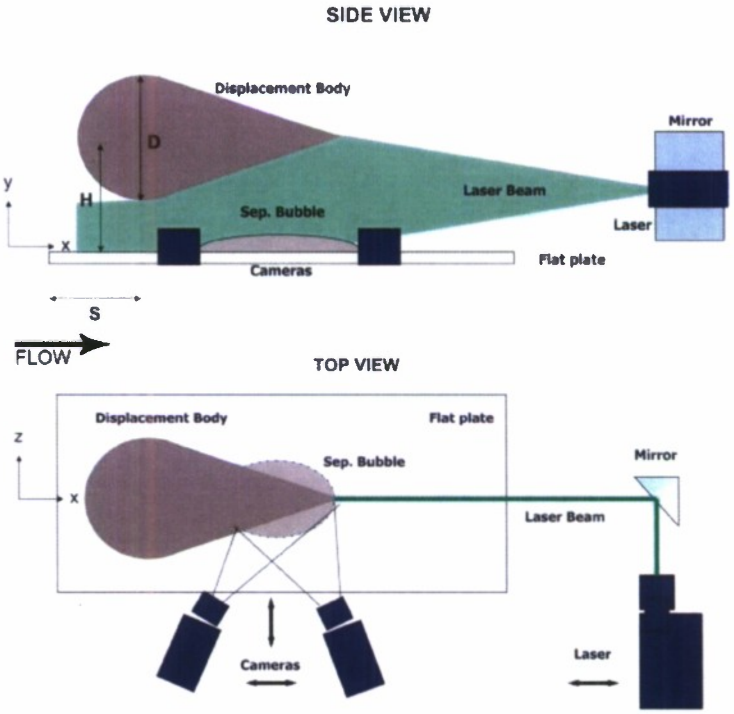
SIDE VIEW
Displacement Body
D
H
y
x
Sep. Bubble
Laser Beam
Mirror
Laser
Cameras
Flat plate
s
FLOW
TOP VIEW
Displacement Body
Flat plate
z
x
Sep. Bubble
Mirror
Laser Beam
Cameras
Laser

*Fig. 5.1: Sketch of experimental setup showing displacement body, separation bubble and stereo PIV equipment (not to scale).*

### 5.1.1 Exploratory Experiments

First, a preliminary experimental setup was developed for some exploratory experiments. In order to speed up design and construction, it was decided to construct the three-dimensional displacement body from materials that were already available in the lab (Fig. 5.2). This allowed us to quickly set up and run our experiments and obtain flow visualizations using dye injection to get a first glance at three-dimensional separation bubbles. Based on these observations, we proceeded with the design of an advanced and accurate displacement body with improved boundary layer suction.

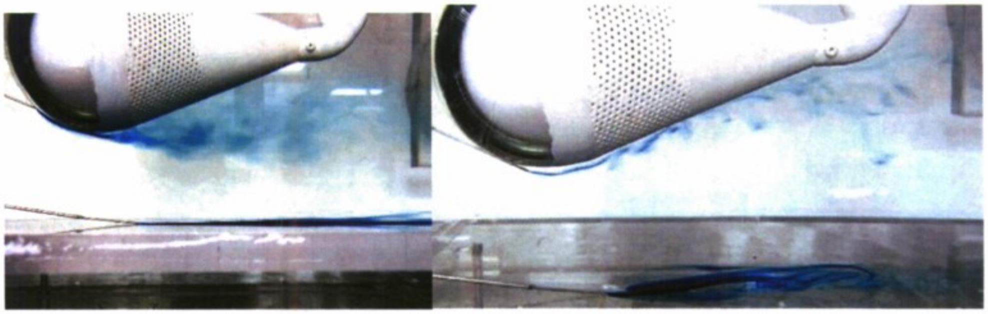

*Fig. 5.2: Preliminary displacement body. Without (left) and with boundary layer suction (right).*

### 5.1.2 Axisymmetric Displacement Body

The displacement body was built from a fiberglass shell. A negative mold was generated from a positive model, which had been fabricated from aluminum (Fig. 5.3). The final fiberglass displacement body was obtained using the negative molds (Fig. 5.4). Both, displacement body and flat plate were painted in matte black to reduce glare during the PIV measurements. To prevent separation from the displacement body, boundary layer suction was applied. The suction holes had a diameter of 1mm. Gravity forced suction was generated by a long pipe that lead to the basement of the building. This method was preferred over a suction pump which could introduce undesired disturbances. The removed water was pumped back into the tunnel to ensure a constant static pressure in the test section. The highest suction volume flow rate was 10.5 liter/min. By adjusting the length of the suction pipe the flow rate could be increased or decreased. This adjustment was performed whenever the flow conditions (e.g. Reynolds number) were altered. We took great care to ensure that the boundary layer suction was as axisymmetric as possible.

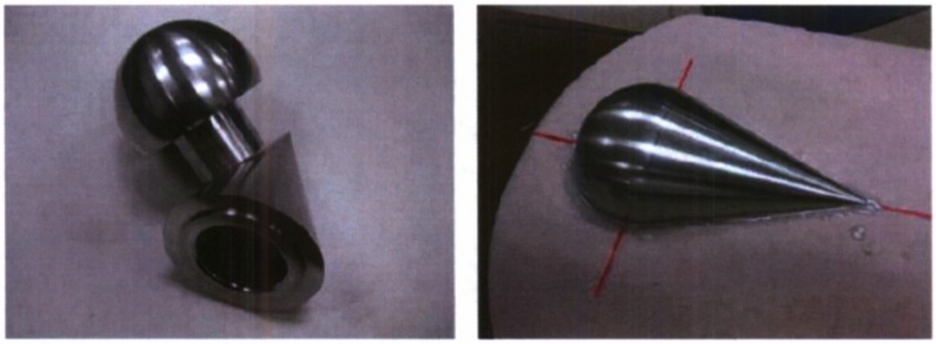

*Fig. 5.3: Lathed aluminum positive.*

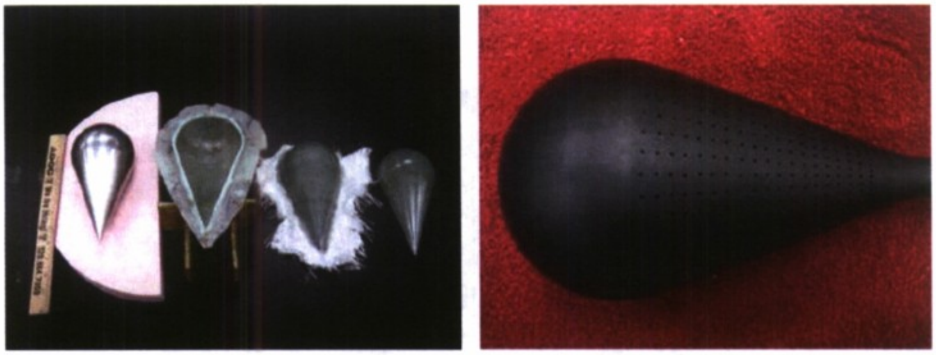

*Fig. 5.4: Manufacturing of displacement body from aluminum positive body, negative fiberglass mold and positive half-shell (left). The final displacement body with boundary layer suction holes is shown on the right.*

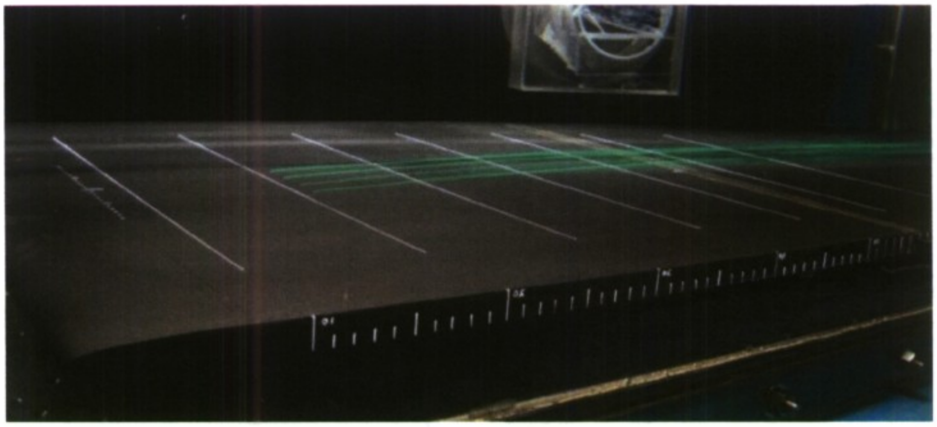

*Fig. 5.5: Fluorescent dye injection on surface of modular flat plate.*

### 5.1.3 Flat Plate

In addition to the displacement body, a flat plate model was manufactured. The flat plate consists of a leading edge, an exchangeable middle section with dye injection holes and a trailing edge. The surface roughness was minimized to maintain laminar flow over the entire length of the flat plate. Interchangeable middle-sections allow for an adjustment of the plate's configuration and length. The dimensions of the flat plate were chosen such that the experimental setup could be varied. The dye injection holes allow us to visualize the flow close to the wall. The dye flow rate can be regulated from outside the water tunnel. A typical dye visualization without displacement body (Fig. 5.5) clearly indicates that the flow over the flat plate is laminar.

## 5.2 Results from Dye Flow Visualization

Before we carried out detailed velocity measurements with the La Vision stereoscopic Particle Image Velocimetry (PIV) system, we employed fluorescent dye for flow visualization. Using dye flow visualizations we were able to identify the reverse flow region and the limiting streamlines of separation. The dimensions of the separation bubble were documented for different Reynolds numbers. Results are presented for a Reynolds number range of $Re_D$=5,000 to

$Re_D$=15,000, a wall-normal distance of the displacement body from the flat plate of H=1, and a downstream distance of the displacement body from the leading edge of the flat plate of S = 2.5D. For a Reynolds number of $Re_D$ = 5,000 the bubble was found to be steady. For $Re_D$ = 7,500 the separation bubble was almost steady (Fig. 5.6), whereas for higher Reynolds numbers the bubble was found to shed vortical structures.

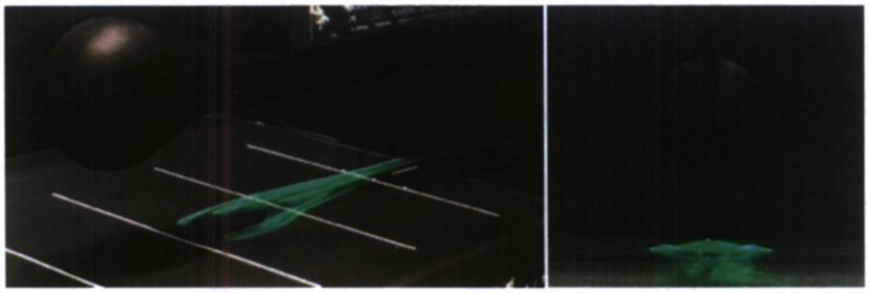

*Fig. 5.6: Perspective view (left; flow direction from left to right) and view from the back (right; flow direction towards the observer) for $Re_D$ = 7,500. The separation bubble was visualized using fluorescent dye.*

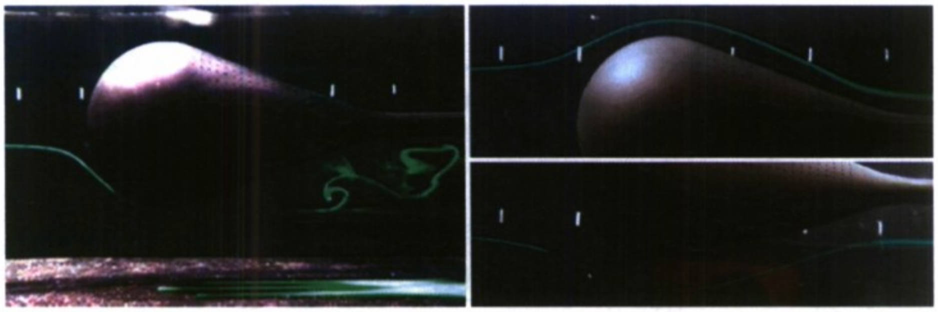

*Fig. 5.7: Flow visualization without (left) and with (right) boundary layer suction for $Re_D$=7,500, H=1 and S=2.5D.*

In order to generate a sufficiently large pressure gradient on the flat plate, flow separation from the displacement body had to be prevented by applying boundary layer suction. Dye flow visualization was utilized to optimize the suction flow rate (Fig. 5.7). Without suction the flow separates near the apex of the displacement body, whereas with boundary layer suction the flow remains attached and the dye lines follow the contours of the displacement body.

For the baseline case ($Re_D$=7,500, H=1 and S=2.5D) two so-called "horn vortices" are present on the flat plate. The topology of the bubble can be outlined by streamlines in the symmetry plane and by surface skin friction lines. The best flow visualization results were obtained when the fluorescent dye was injected through four holes on the surface of the flat plate (Fig. 5.8). The limiting streamlines are characterized by a saddle point (S) which is the upstream separation location in the symmetry plane as well as two foci (F) which are situated at the base of the horn vortices. To capture the development of the foci in our visualizations, only the outer streamlines of the bubble were visualized as shown on the right in Fig. 5.9.

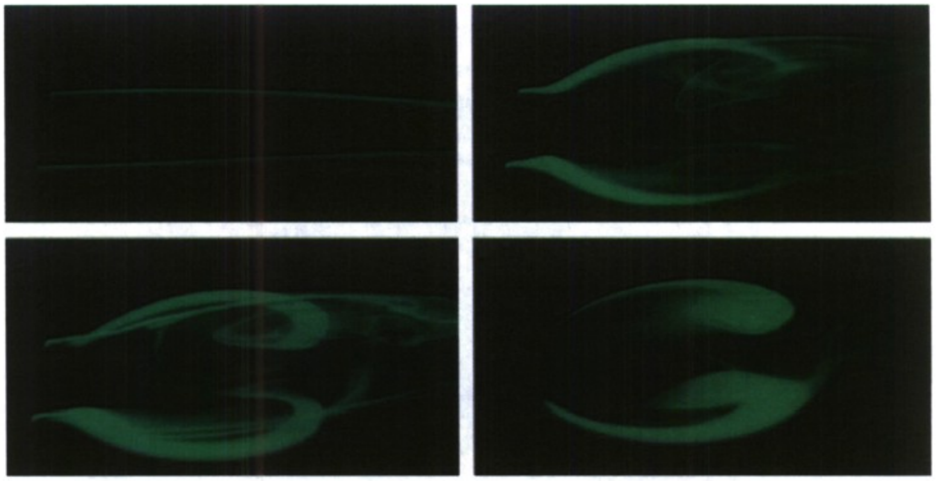

*Fig. 5.8: Transient development of separation bubble (after pressure gradient is applied by turning on boundary layer suction) for the baseline case ($Re_D$=7,500, H=1, S=2.5D).*

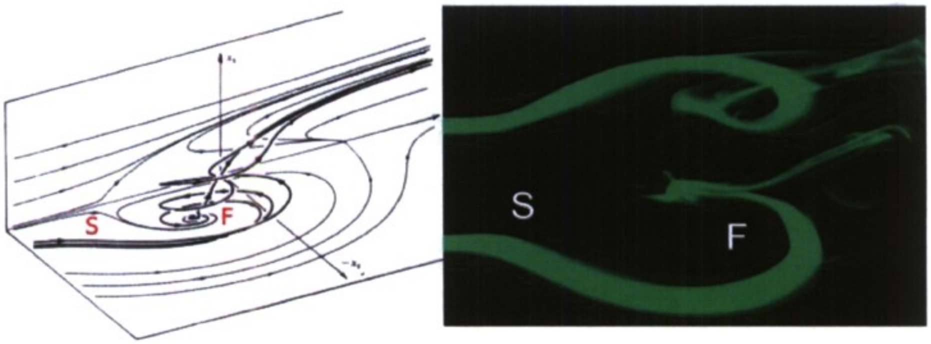

*Fig. 5.9: Location of foci in three dimensional separation bubble. Flow topology sketch (left) by Perry and Chong [1986] and dye flow visualization (right) for Re = 7,500, H = 1, and S = 2.5D.*

For high enough Reynolds numbers the separated flow becomes unstable, resulting in the shedding of vortical flow structures from the bubble. With increasing Reynolds number the unsteady flow structures appear further upstream, leading to an earlier reattachment of the separated flow. This trend is shown in Fig. 5.10. We also found that by bringing the displacement body closer to the flat plate the shedding frequency could be increased. In addition, for certain conditions we observed a so-called bubble "breathing" that results in an intermittent change of the physical size of the separation bubble (Fig. 5.11).

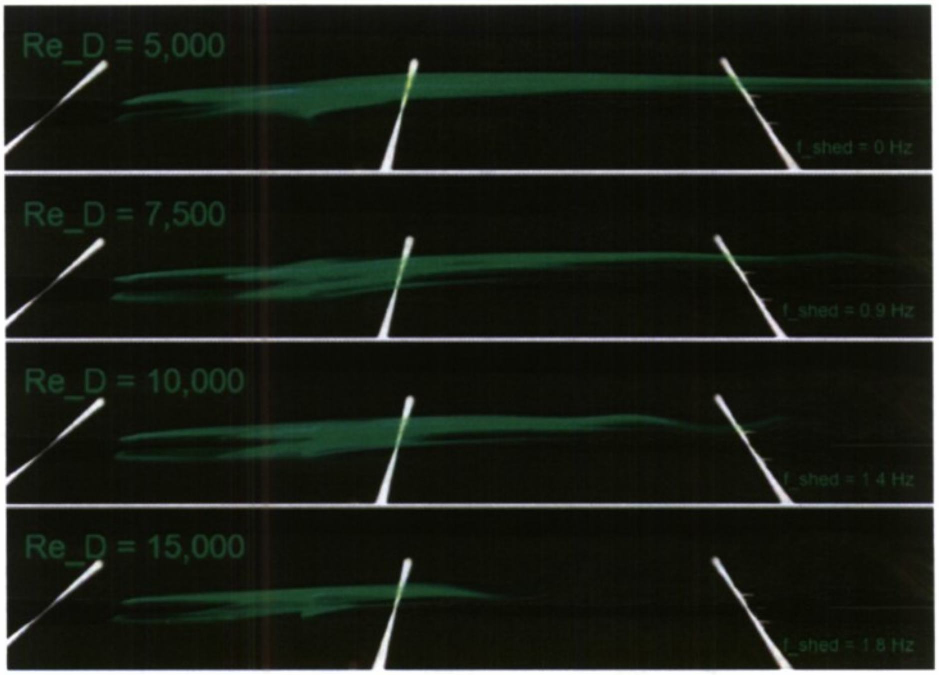

*Fig. 5.10: Side view of separation bubbles for Reynolds number range $Re_D = 5{,}000$ to $Re_D = 15{,}000$ using fluorescent dye. As the Reynolds number is increased beyond 7,500, the bubble begins to shed vortical structures. The dominant shedding frequency of each case is shown in the lower right corner.*

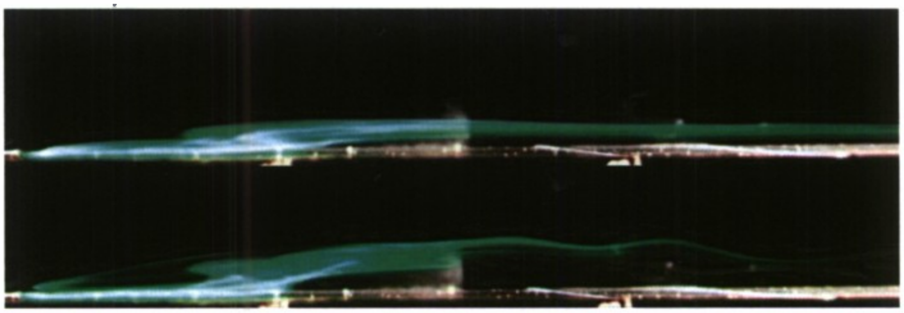

*Fig. 5.11: Sideview of the separation bubble for $Re_D=5{,}000$, $H = 1$, and $S = 2.5D$. Dye flow visualizations showing the two states (steady and unsteady) of the "bubble breathing" cycle.*

## 5.3 PIV Measurements

For all Reynolds numbers considered ($Re_D = 5{,}000$ to $Re_D = 15{,}000$) we measured the instantaneous velocity components in the mid-span plane and parallel spanwise planes. Since the field of view of one camera is limited to about 50mm, several sets of images were taken and later on patched together. First, instantaneous velocity measurements were obtained at a number of locations in downstream direction, and then the averaged velocity field over the entire extent of the separation bubble was constructed from the instantaneous data. Finally, velocity profiles at different downstream locations were extracted from the time-averaged PIV data (Fig. 5.12).

Normalized with the freestream velocity, the velocity profiles confirmed the different local flow behavior which was already observed in the dye flow visualizations. A Blasius velocity profile was measured upstream of the separation bubble. In the bubble, inflectional profiles with various degrees of reverse flow near the wall were obtained.

Using PIV, we also measured the flow around the displacement body to once more confirm that the suction strength and distribution were appropriate (Fig. 5.13). We then measured the time-averaged flow in the mid-span plane. In Fig. 5.14 the results from these measurements for various Reynolds numbers are presented. Streamlines overlaid with streamwise velocity contours, as well as velocity profiles at different downstream locations are shown. As already observed in the dye flow visualizations, the length of the separation bubble decreases with increasing Reynolds number. In addition, the time-averaged PIV measurements also indicate that the separation bubble height decreases with increasing Reynolds number.

For a Reynolds number range of $Re_D = 7{,}500$ to $Re_D = 15{,}000$ we observed an intermittency phenomenon. Due to the recirculating fluid in the separation bubble, the size of the bubble, in particular its height, increases. The separated shear layer moves away from the wall and the reverse flow velocity increases to a point where the bubble starts shedding (Fig. 5.11). The vortical structures associated with the shedding lead to flow reattachment, which weakens the reverse flow and stops the shedding. The frequency of this "breathing" cycle was found to be in the order of $f_{breath} = 0.03$ Hz to 0.2 Hz for $Re_D = 7{,}500$ to 15,000.

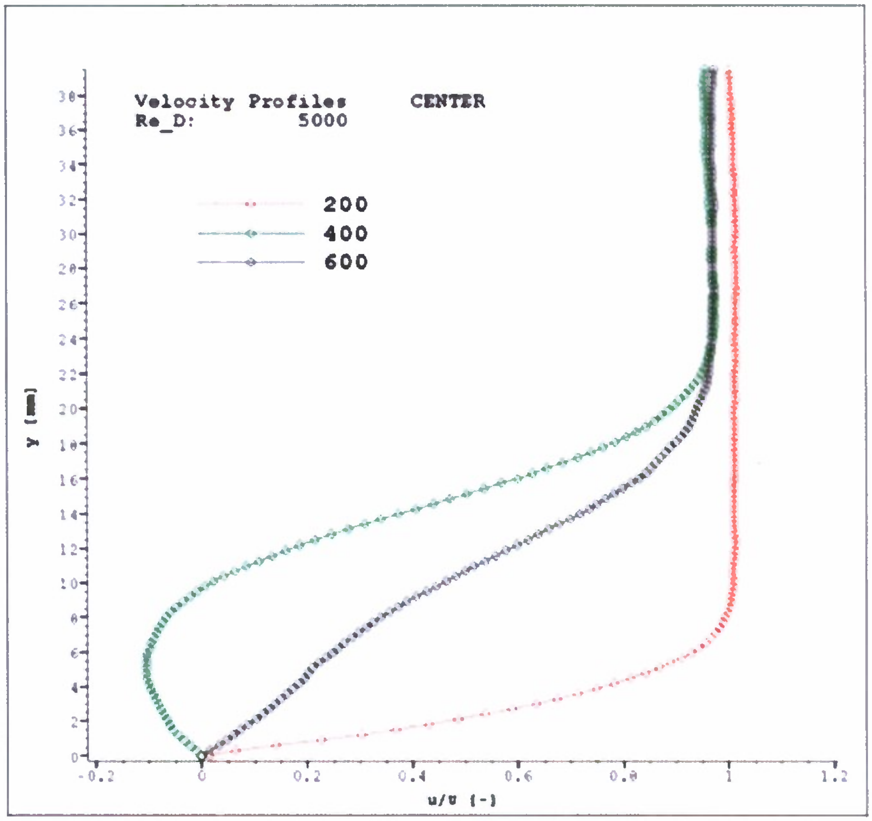

*Fig. 5.12: PIV data: Time averaged velocity profiles at different downstream locations relative to the flat plate leading edge (normalized with free stream velocity; $Re_D = 5{,}000$, $H=1$, $S=2.5D$).*

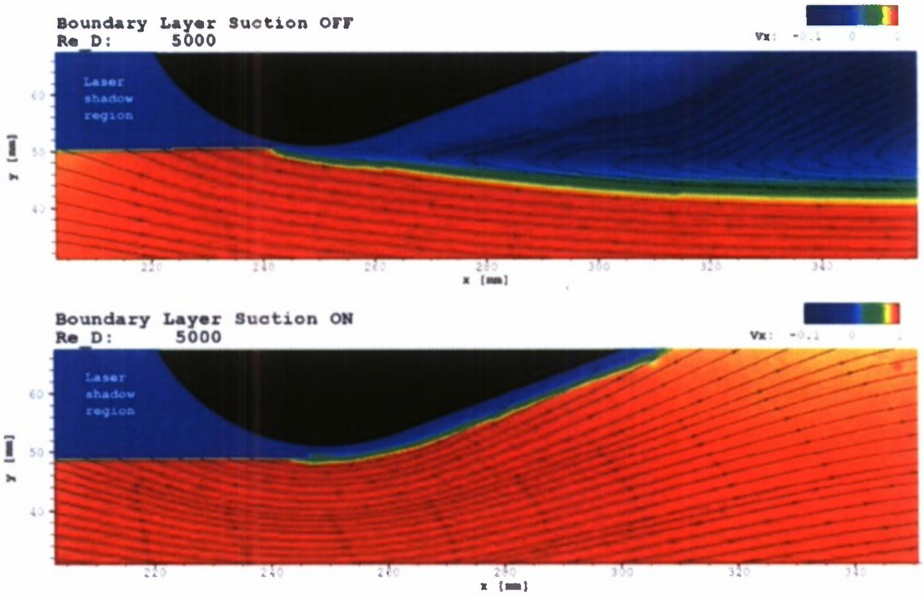

*Fig. 5.13: PIV data: Streamlines showing the separated boundary layer without (top) and the attached boundary layer with boundary layer suction (bottom).*

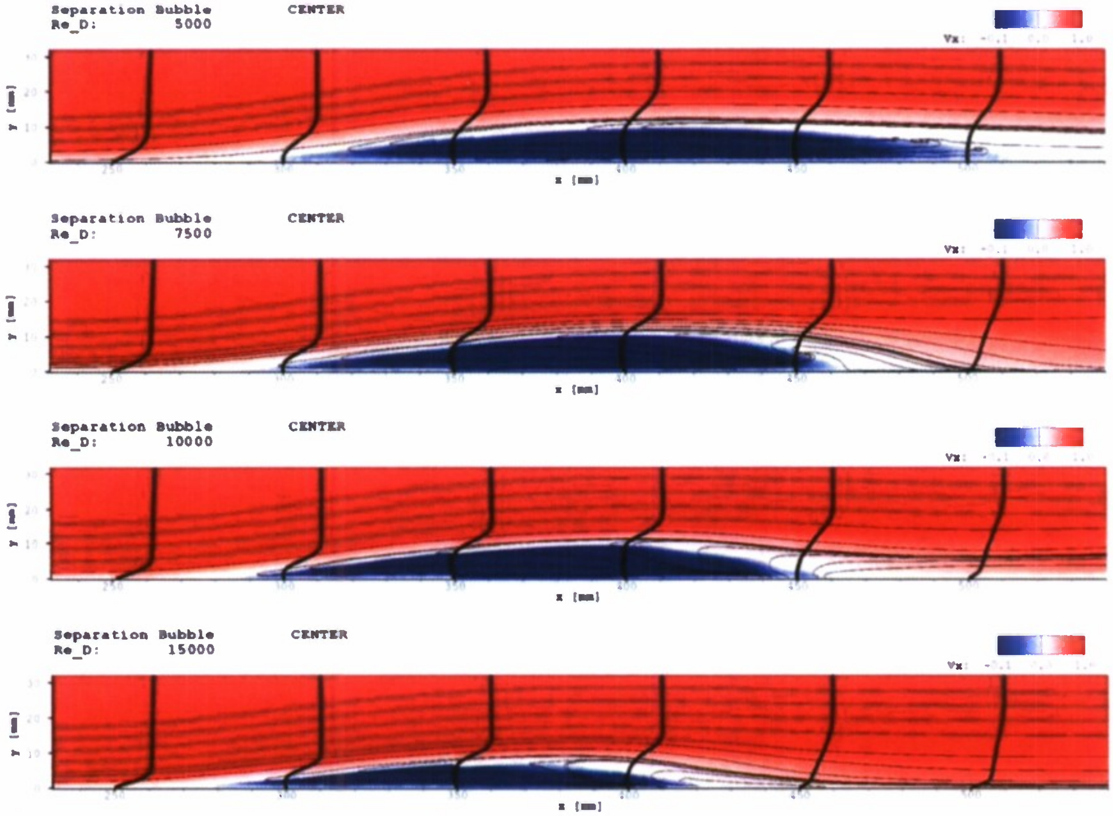

*Fig. 5.14: PIV data for $Re_D$ = 5,000 to $Re_D$ = 15,000, H = 1 and S = 2.5D. Streamlines and velocity contours of streamwise velocity in the mid-span plane (z=0), as well as velocity profiles at different downstream locations.*

# 6. SQUARE-DUCT FLOW SIMULATIONS

Before investigating the Stanford diffuser flow, which is physically more complex and which features a turbulent separation bubble, we carried out simulations of a square-duct flow using DNS, RANS, and hybrid RANS/LES. The purpose of these simulations was to determine the grid resolution required for DNS and to assess RANS and hybrid models for a well documented 3-D channel flow. For these simulations the Reynolds number based on bulk velocity and hydraulic diameter was $Re_b$=10,000.

## 6.1 Computational Grid

The hybrid turbulence model simulations were carried out for 3 different grid resolutions to determine how well the hybrid models adapt to changes in the grid resolution. We employed computational grids with 192×40×40 (coarse grid, 307,200 cells), 192×54×54 (medium grid, 559,872 cells) and 384×80×80 (fine grid, 2,457,600 cells) cells (Fig. 6.1). The near-wall grid resolution in wall units $\Delta x^+ \times \Delta y^+ \times \Delta z^+$ was 82.1×0.941×1.88...43.6 (coarse grid), 41.1×0.941×1.88...20.6 (medium grid), and 20.5×0.941×1.88...9.87 (fine grid). In addition, as a reference, we also carried out a direct numerical simulation (DNS) on a super fine grid with 384×160×160 cells (9,830,400 cells, Fig. 6.2) where we resolved all scales of motion. The near wall grid line spacing in wall units was $\Delta x^+$=10.3, $\Delta y^+$=0.314, $\Delta z^+$=0.627...4.62. The grids were generated such that the laminar sublayer was resolved.

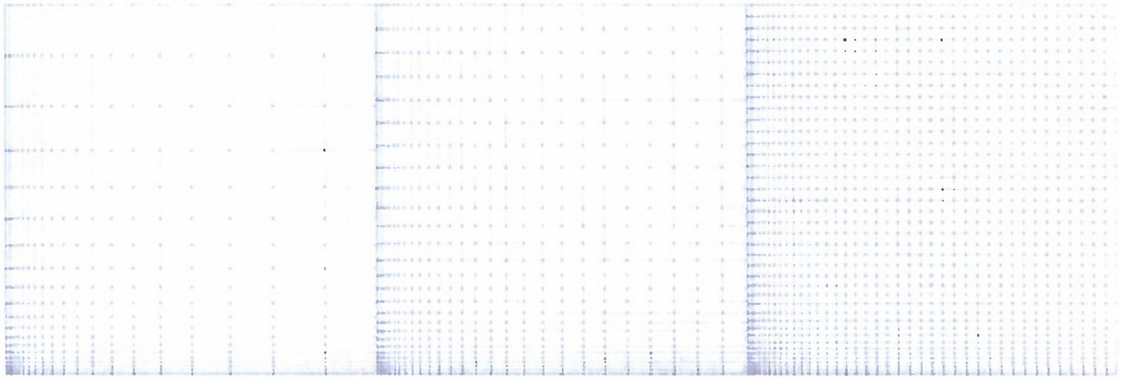

*Fig. 6.1: Cross-sectional views of lower left corner of computational domains for hybrid RANS/LES simulations of square-duct flow. From left to right: Coarse, medium, and fine grid.*

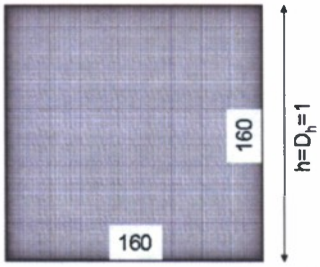

*Fig. 6.2. Cross-sectional view of computational grid for DNS of square-duct flow.*

## 6.2 Domain Length

We first investigated the effect of the domain length. Huser and Biringen determined a zero streamwise correlation for a streamwise separation of 3.2 [Huser and Biringen 1993]. Accordingly, a domain length of $L_x = 6.4$ was chosen. Interestingly, the domain length in the DNS by Gavrilakis [1992] was $L_x = 5\pi$ while Madabhushi and Vanka [Madabhushi and Vanka 1991] decided on a domain length of $L_x = 2\pi$. To save computer time we performed a domain length analysis for the coarse resolution grid using FBR [Johansen et al. 2004] and the 1998 k-ω model with EASM. During the run time of the simulation we recorded velocity data at the mid-channel location. Auto-correlations of the recorded u-velocity component are shown in Fig. 6.3. For $L_x = \pi$ the auto-correlation has multiple peaks which can be associated with the domain length and its multiples. As the domain length is increased by factors of two (with the streamwise grid resolution being kept constant at $\Delta x = 2\pi/192$) "in-between" peaks disappear and the maxima get smaller indicating reduced coherence of domain length related waves. For $L_x = 4\pi$ a weak peak can still be discerned for $\Delta t \approx 10$, while at $L_x = 8\pi$ the auto-correlation is almost flat. Isocontours of the u-velocity at mid-span (Fig. 6.4) provide visual evidence of the large structures.

We decided that a domain length of $L_x = 8\pi$ was sufficient for our coarse grid simulations. Out of practical considerations we reduced the domain length to $4\pi$ for the medium and fine grid and to $2\pi$ and $\pi$ for the super fine grid to keep the number of cells and the computational expense down to a reasonable limit.

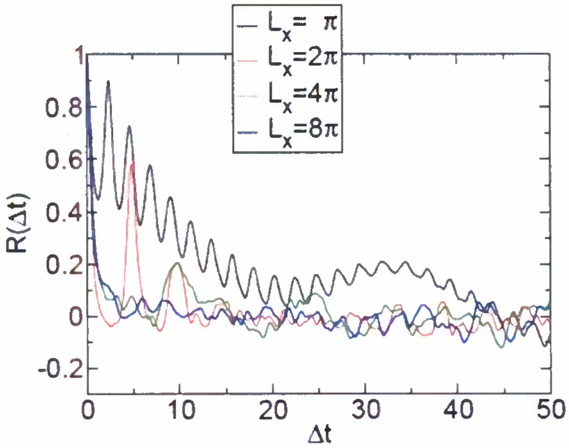

*Fig. 6.3 Square-duct flow at Re=10,000. FBR and 1998 k-ω model with EASM. Auto-correlation of u-velocity disturbance at y = z = 0.5 for different streamwise domain extents.*

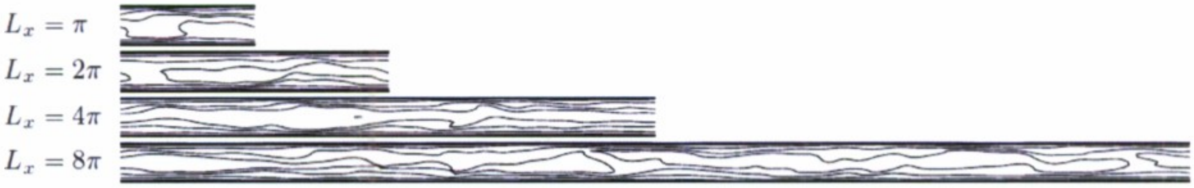

*Fig. 6.4. Square-duct flow at Re=10,000. FBR and 1998 k-ω model with EASM. Isocontours of u-velocity (0 . . . 1.5, Δ = 0.1) at mid-span.*

### 6.3 Direct Numerical Simulation (DNS)

An instantaneous visualization obtained from the reference DNS for Re=10,000 [Gross and Fasel 2009a] is provided in Fig. 6.5. Here, the Q vortex identification criterion by Hunt et al. [1988] was employed for visualizing vortical structures. The near wall region of turbulence production is populated by worm-like structures. In wall bounded flows turbulent streaks have an average length and spanwise spacing in wall units of roughly 1000 and 100 [Cantwell 1981].

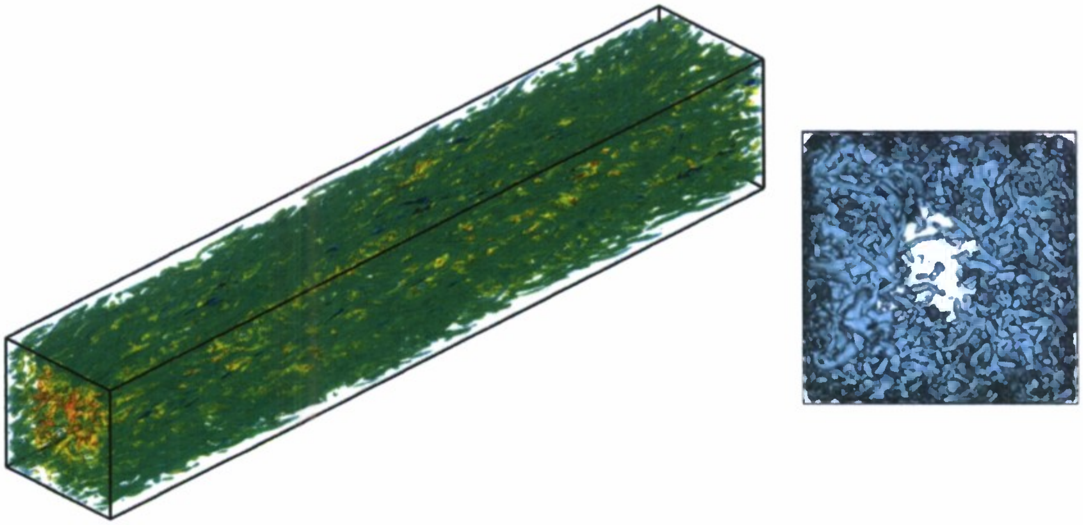

*Fig. 6.5: DNS of square-duct flow. Isosurfaces of Q=5.*

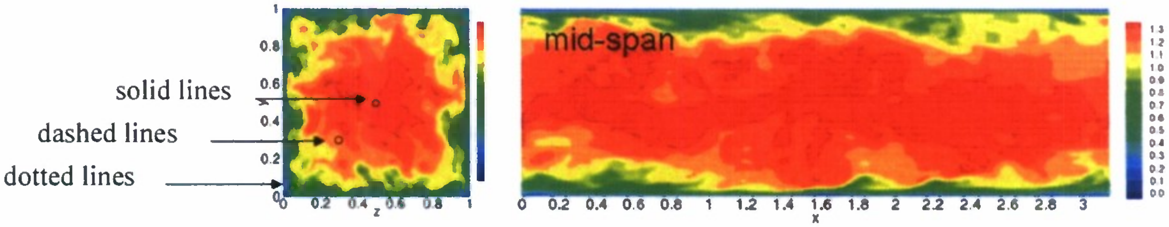

*Fig. 6.6: DNS of square-duct flow. Isocontours of streamwise velocity in cross-flow plane (left) and at mid span, z=0.5 (right).*

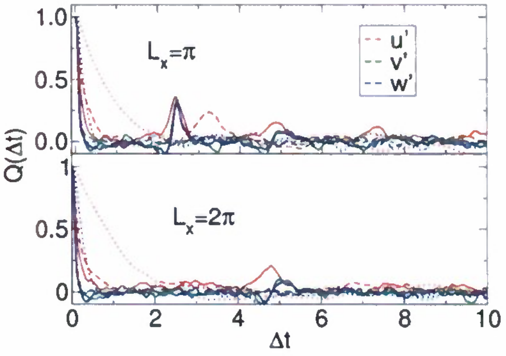

*Fig. 6.7: Auto-correlations of velocity fluctuations at y=z=0.0493 (dotted lines), 0.297 (dashed lines), 0.496 (solid lines).*

Instantaneous visualizations of the streamwise velocity component are provided in Fig. 6.6. Also indicated are 3 points which were situated halfway into the channel at $y=z=0.0493$, 0.297, 0.496 where time-dependent velocity data was extracted. The turbulent structures are seen to reach all the way to the center of the channel. Autocorrelations of the velocity data obtained at the 3 locations indicated in Fig. 6.6 over time intervals of 300 are shown in Fig. 6.7. For the short domain, $L_x = \pi$, peaks are seen near $\Delta t = 2.5$ for $y = z = 0.496$ and 3.2 for $y = z = 0.297$. With a mean flow velocity of about 1.32 near the center of the channel and 1.25 near $y = z = 0.297$ the corresponding downstream wavelengths are 3.3 and 4. Therefore, the peak at $\Delta t = 2.5$ is likely related to the domain length. Additional confirmation is provided by the fact that it disappears for the longer domain, $L_x = 2\pi$. A peak is also seen near $\Delta t = 4.8$ for both, the short and the long domain. This peak is likely related to the domain length of $L_x = 2\pi$. Although our domain length study showed that a domain length of $2\pi$ was insufficient, out of practical considerations and also because Huser et al. [1993] used a domain length of $2\pi$ in their simulations, we did not further increase the downstream extent of the computational domain for our DNS.

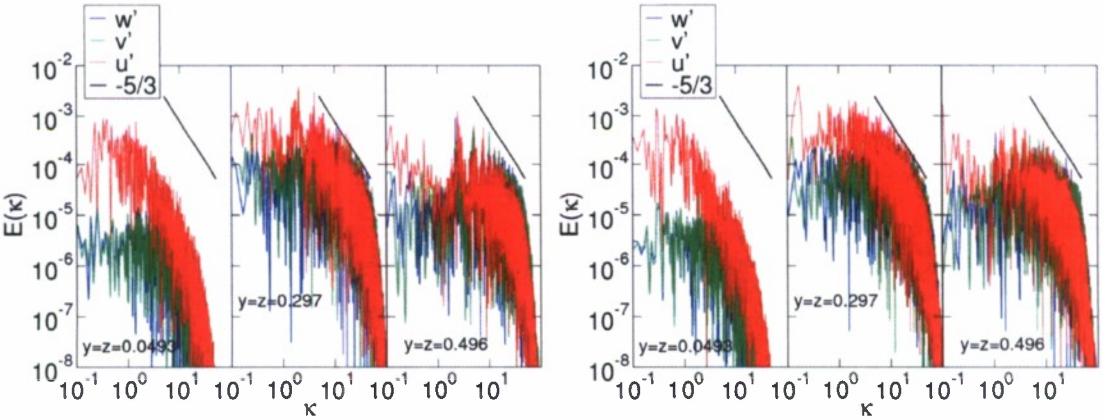

*Fig. 6.8: Energy spectra computed from velocity fluctuations for short ($L_x=\pi$) and long domain ($L_x=2\pi$).*

We also computed the energy spectra (Fig. 6.8). The spectra display the -5/3 slope decay which is characteristic of the inertial subrange. Distinct peaks are visible at the low frequency end of the spectrum. Some of the peaks can be directly related to the peaks in the autocorrelation, e.g. for the short domain peaks are located at $\kappa = 2\pi f = 2\pi/2.5 = 2.5$ and $2\pi/3.2 = 2.0$. Other peaks may likely be associated with energetic coherent flow structures. Since the mean flow is almost grid converged, since computations with longer computational domain are expensive, and since the purpose of the present DNS was to provide mean flow reference data for comparison with RANS and hybrid RANS/LES results, it was decided that the long domain data were sufficiently accurate.

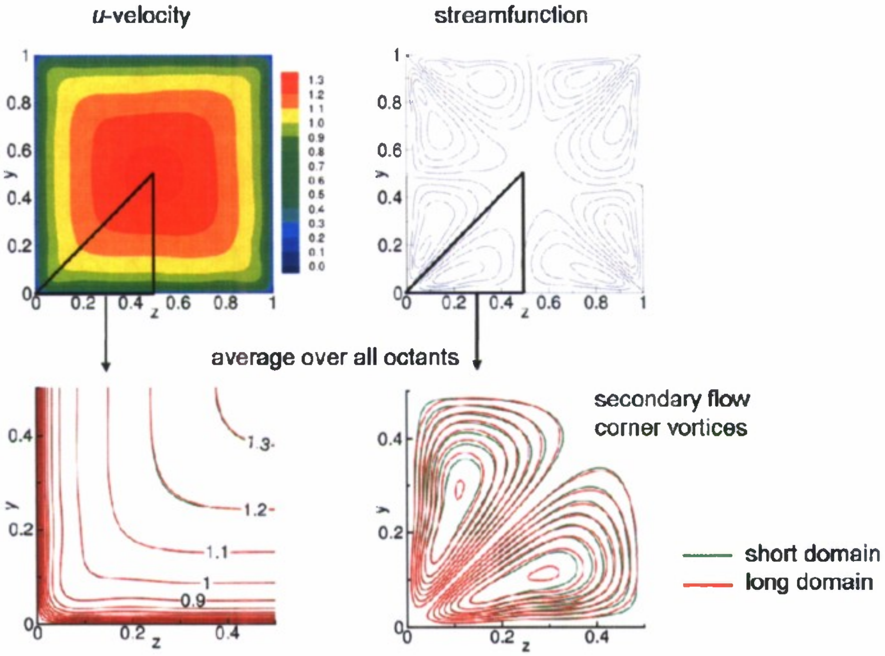

*Fig. 6.9: Temporal and streamwise average of DNS data for $L_x=2\pi$.*

Fig. 6.9 shows temporal and streamwise averages of the flow. As a result of the finite duration of the time-averaging process the averages are not fully symmetric. By also averaging over all octants a symmetric picture is obtained. When considering isocontours of the streamfunction, $\Psi$, ($v=\partial\Psi/\partial z$ and $w=-\partial\Psi/\partial y$) counter-rotating streamwise vortices emerge that transport high momentum fluid from the center into the corners. This secondary flow of Prandtl's second kind is induced by the Reynolds stresses and typical for duct flows with corners. Almost identical results were obtained for the short and long domain. The computed bulk velocities of 1.03 for the short and long domain are in close agreement with the expected result of 1. The slight mismatch may be attributed to numerical factors such as accuracy and/or resolution, the domain length or the empirical relation (we used Petukhov's) that was employed for obtaining the magnitude of the volume force that drives the flow. Velocity profiles in wall units are compared in Fig. 6.10. Our DNS data are in good agreement with other simulation data [Gavrilakis 1992, Madabhushi and Vanka 1991, Huser and Biringen 1993].

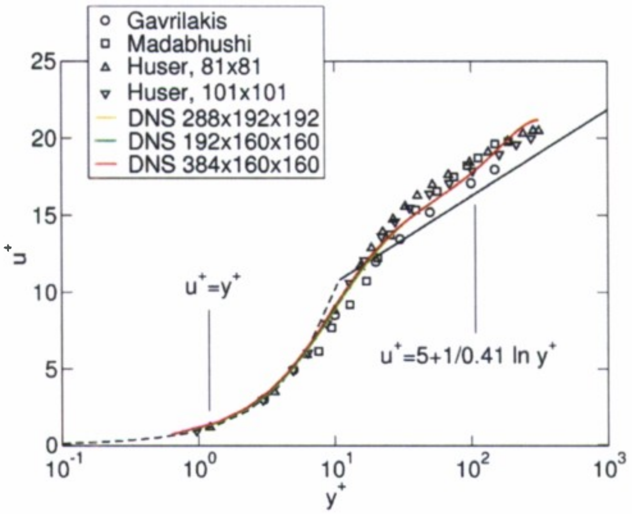

*Fig. 6.10: Velocity profiles in wall units at wall bisector.*

## 6.4 Reynolds-Averaged Navier-Stokes (RANS) Calculations

We also carried out steady RANS calculations for Re=10,000 and for the coarse, medium, and fine grid to determine a suitable underlying RANS model for the hybrid simulations. Because hybrid RANS/LES reverts to RANS in the coarse grid limit the accuracy of the RANS model is important. Isocontours of eddy viscosity, $\mu_T$, turbulence kinetic energy, k, and streamfunction, $\Psi$, taken in the cross-flow plane are shown in Fig. 6.11. The streamfunction isocontours indicate counter-rotating streamwise vortices that transport high momentum fluid from the center into the corners. The Explicit Algebraic Stress Model (EASM) [Rumsey and Gatski 2001] is needed to capture this secondary flow. With the low-Reynolds number terms the near wall turbulence kinetic energy is increased. A comparison with the DNS data is provided in Fig. 6.12. Although the secondary flow is captured with the EASM its intensity and spatial characteristics only approximately match the DNS data.

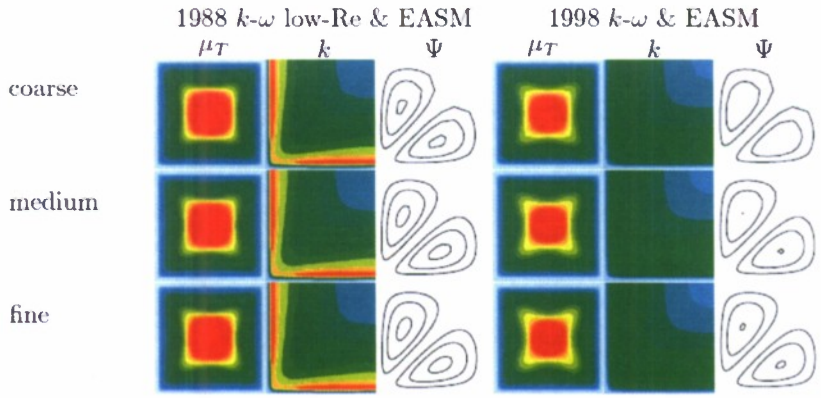

*Fig. 6.11: Square-duct flow at Re=10,000. RANS results. Isocontours of eddy viscosity ($\mu_T = 0 \ldots 40$), turbulence kinetic energy ($k = 0 \ldots 0.02$) and streamfunction (lower left quadrant, $\Psi = -0.002 \ldots 0.002$) in cross-flow plane obtained from steady RANS calculations.*

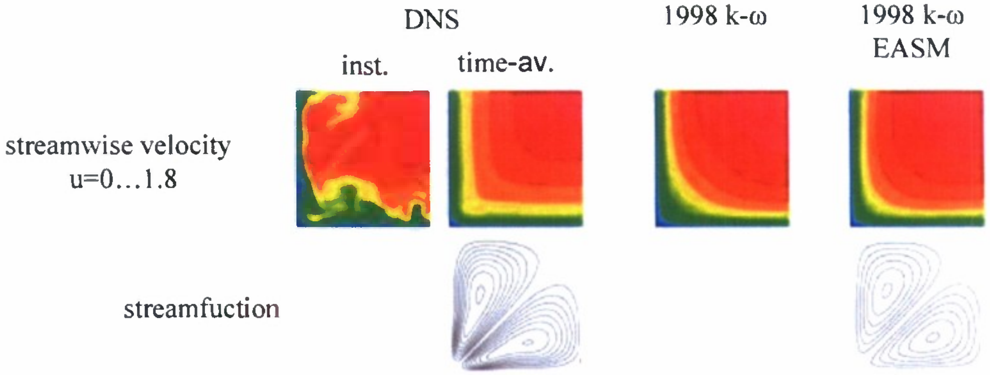

*Fig. 6.12: DNS. Isocontours of instantaneous u-velocity ($0<u<1.8$, $\Delta u=0.1$). Isocontours of u-velocity and streamfunction ($-0.001<\Psi<0.001$, $\Delta\Psi=0.0001$) for RANS results obtained with 1998 k-ω model with Boussinesq approximation and EASM.*

A more quantitative comparison becomes possible when considering profiles taken at the wall and corner bisector and comparing with our DNS results and the DNS data by Huser and Biringen [1993]. The RANS velocity profiles in wall units (Fig. 6.13a) all overshoot the log-layer law, $u^+ = 5 + 1/0.41 \ln y^+$, which may be attributed to 3-D effects resulting from the vicinity of the neighboring walls, and display a larger log layer slope than the DNS data. The mismatch requires further attention in the future. Profiles of the v-velocity taken at the corner bisector allow for a comparison of the secondary flow amplitudes (Fig. 6.13b). Our DNS results agree with the Huser and Biringen [1993] DNS data with respect to the maximum amplitude, although the shapes of the curves are slightly different. The secondary flow is under-predicted in the RANS calculations and the amplitude distribution does not match the DNS data. A comparison of the Reynolds normal stresses, $\overline{u'u'}$, $\overline{v'v'}$, and $\overline{w'w'}$ is provided in Fig. 6.13c. For our DNS, statistical quantities were time-averaged over a time interval of 400. Agreement of our DNS data with the Huser and Biringen [1993] DNS data is only seen for the streamwise normal Reynolds stress. Discrepancies in the $\overline{v'v'}$ and $\overline{w'w'}$ distributions necessitate further examination. The RANS data match the DNS data only qualitatively. With the low-Reynolds number terms, higher near wall normal Reynolds stresses are predicted. Finally, profiles of the Reynolds shear stress and the turbulence kinetic energy are shown in Fig. 6.13d. Surprisingly, the Reynolds shear stress profiles from the DNS and RANS are quite close. A very good match between the two DNS data sets is seen for the turbulence kinetic energy. Especially near the wall the turbulence kinetic energy distribution obtained from the RANS calculation with low-Reynolds number terms agrees reasonably well with the DNS data. Without low-Reynolds number terms, the near wall turbulence kinetic energy peak is, as expected, under-predicted.

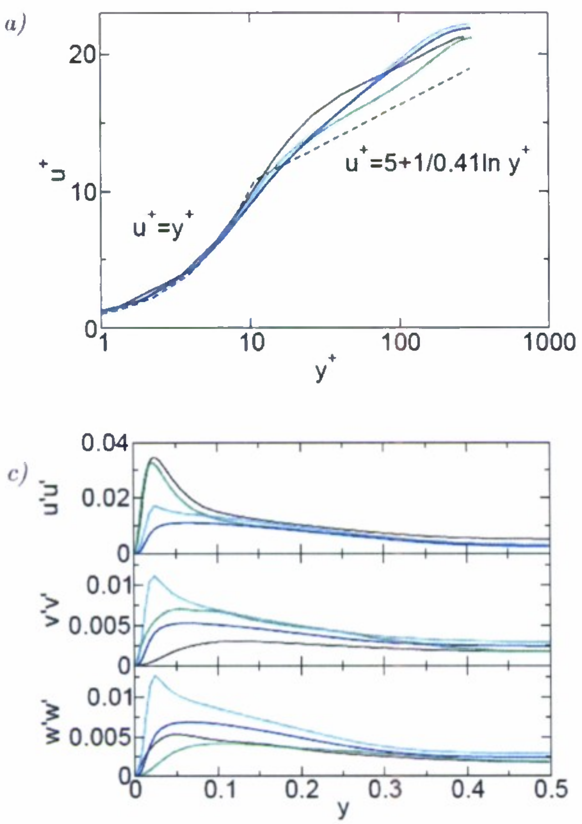

*Fig. 6.13: Square-duct flow at Re=10,000. a) Wall bisector profiles of streamwise velocity in wall units. b) Corner bisector profiles of v-velocity component. c) and d) Wall bisector profiles of Reynolds stresses and turbulence kinetic energy. Black lines: $u^+$ from Fig. 6, run B, −v from Fig. 7b, run B, u'u' and u'v' from Fig. 11c/a, v'v' and w'w' from Fig. 13a/b in Huser and Biringen [1993]; Green lines: our DNS; Cyan lines: RANS, 1988 k-ω low-Re and EASM; Blue lines: RANS, 1998 k-ω and EASM.*

## 6.5 Hybrid RANS/LES Simulations

We then computed the same flow using two hybrid turbulence models that we determined successful in an earlier numerical campaign [Gross and Fasel 2008b, 2009a,b]. We employed both, a modified version of our flow simulation methodology (FSM) [Speziale 1997, Fasel et al. 2002] where the model contribution is computed from the von Kármán energy spectrum and the filter-based RANS approach [Johansen et al. 2004] with filter-width set equal to the local grid line spacing. An approach similar to the one by Batten et al. [2004] was employed for "injecting" or "seeding" statistically random turbulent motion in regions with vanishing model contribution [Gross and Fasel 2009b]. As underlying turbulence models we employed the 1988 k-ω model with low-Reynolds number terms and the 1998 k-ω model, both with EASM. Time-averages were computed over time-intervals of 400, except for the coarse grid FSM with 1988 k-ω model and low-Reynolds number terms and the medium grid FSM with 1998 k-ω model for which time-averages were computed over time-intervals of 360 and 300, respectively.

Velocity fluctuations were computed with respect to the unprocessed "raw" time-averages, meaning that the time-averages were not averaged in the streamwise direction and over the 8 octants. The reasoning behind this approach was that any imbalances or inaccuracies in the code that may result in an asymmetry in the solution, which would be captured in the time-averages, would result in a systematic error if the time-averages were averaged in the streamwise direction or over the 8 octants. For the cases where the computed bulk velocities were close to the DNS value of 1.03 statistical quantities were computed over a time interval of 400.

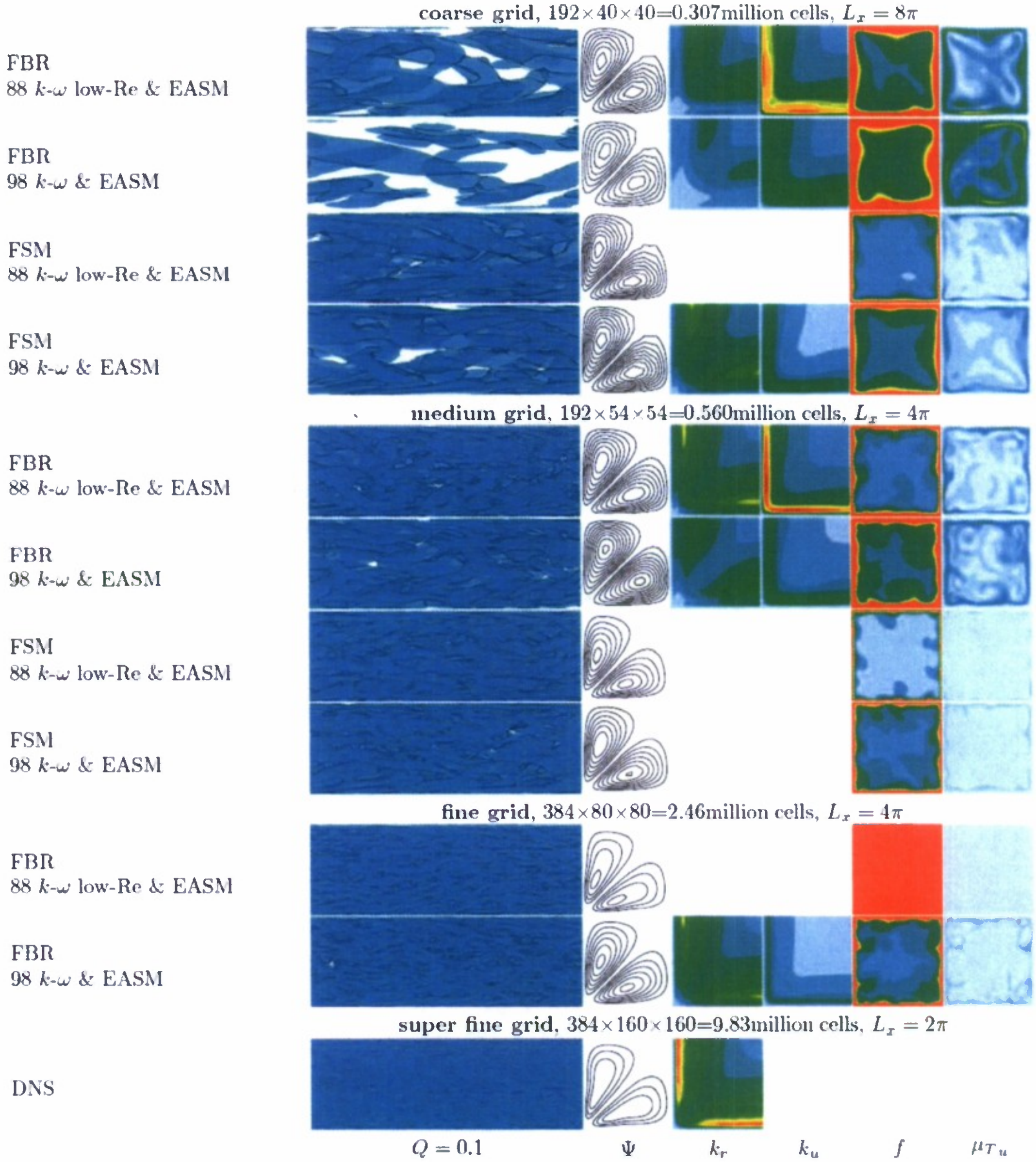

*Fig. 6.14: Square-duct flow at Re=10,000. Hybrid RANS/LES and DNS. Isosurfaces of* $Q = 0.1$*, and isocontours of streamfunction,* $\Psi = -0.002 \ldots 0.002$*, resolved turbulence kinetic energy,* $k_r = 0 \ldots 0.02$*, unresolved turbulence kinetic energy,* $k_u = 0 \ldots 0.02$*, model contribution,* $f = 0 \ldots 1$*, and unresolved eddy viscosity,* $\mu_{Tu} = 0 \ldots 20$*.*

An overview of the different cases is provided in Fig. 6.14. When considering the isosurfaces of the vortex identification criterion, Q = 0.1, which allows for an identification of vortical flow structures, the most small-scale structures are, as expected, observed for the DNS on the super fine grid. As the grid resolution is reduced more and more of the resolved turbulence kinetic energy, $k_r$, is absorbed in the unresolved turbulence kinetic energy, $k_u$, and less and less small-scale flow structures are resolved. Isocontours of the streamfunction, $\Psi$, taken in a cross-flow plane illustrate the secondary flow. Differences in the predicted secondary flow distributions are indicative of differences in the particular Reynolds stress distributions which drive the secondary flow (Fig. 6.14). Huser et al. [1994] compared results obtained from a RANS calculation based on Speziale's non-linear k-ε model with DNS data. They found significant differences between the model prediction and the DNS results, such as an underprediction of the intensity of the secondary flow. The model contribution, f, provides a measure for how much turbulence modeling is afforded by the hybrid RANS/LES models. With increasing grid resolution the model contribution is reduced. With FBR and 1988 k-ω model with low-Reynolds number terms the model contribution is 1 at the highest grid resolution and the unresolved eddy viscosity is close to 0. This inconsistency requires further investigation. In general, a lower model contribution, f, coincides with a smaller unresolved eddy viscosity, $\mu_{Tu}$, and more resolved flow structures. In all instances, the model contribution is 1 near the wall which is desirable as modern RANS models capture wall bounded turbulent flows with high fidelity. The model contribution is seen to be slightly larger for the 1998 k-ω model than for the 1988 k-ω model with low-Reynolds number terms. Also, the model contribution is lower for the FSM than for the FBR which again manifests itself in a larger number of resolved flow structures. However, for the FBR model the constant $C_3$ could be adjusted for reducing the model contribution. The unresolved eddy viscosity, $\mu_{Tu}$, even on the coarse grid, is always less than 20 which indicates that the turbulence model contribution in the present simulations is relatively low.

| modeling | coarse | medium | fine | super fine |
|---|---|---|---|---|
| DNS | | | | 1.03 |
| RANS, 88 k-ω low-Re & EASM | 1.10 | 1.10 | 1.10 | |
| RANS, 98 k-ω & EASM | 1.08 | 1.08 | 1.08 | |
| FBR, 88 k-ω low-Re* | 1.19† | | | |
| FBR, 88 k-ω low-Re & EASM | 1.09 | 1.03 | 1.11 | |
| FBR, 98 k-ω low-Re* | 1.18† | | 1.16 | |
| FBR, 98 k-ω & EASM | 1.09 | 1.05 | 1.02 | |
| FSM, 88 k-ω low-Re & EASM | 1.12 | 1.13 | | |
| FSM, 98 k-ω & EASM | 1.11 | 1.09 | | |

*Tab. 6.1: Square-duct flow at Re=10,000. Computed bulk velocities. *- Discontinued, approximate results; †- Steady solutions.*

A summary of the computed bulk velocities is provided in Tab. 6.1. The DNS result is highlighted in green as it provides the reference for the hybrid simulations. Since we use the same code for the hybrid simulations, the DNS result should be approached in the fine grid limit. The RANS results are highlighted in blue as they provide the low-grid resolution reference for the hybrid simulations. As the grid resolution is reduced the RANS result should be approached. The bulk velocities obtained from our hybrid simulations with FBR, 1998 k-ω model, and EASM approach the RANS result in the coarse grid limit and the DNS result in the fine grid limit. With FBR, 1988 k-ω model, low-Reynolds number terms, and EASM a very good bulk velocity prediction is already obtained for the medium resolution grid, however, for the fine grid, as was seen earlier (Fig. 6.14) the unresolved eddy viscosity goes to zero and the predicted bulk velocity is too high. With 1988/98 k-ω model, Boussinesq approximation, and low-Reynolds number terms steady solutions were obtained for the coarse grid. Medium grid resolution simulations were not attempted. The fine grid simulation with 1998 k-ω model was unsteady. With the present version of the FSM the predicted bulk velocities are slightly too high and the model contribution is too low.

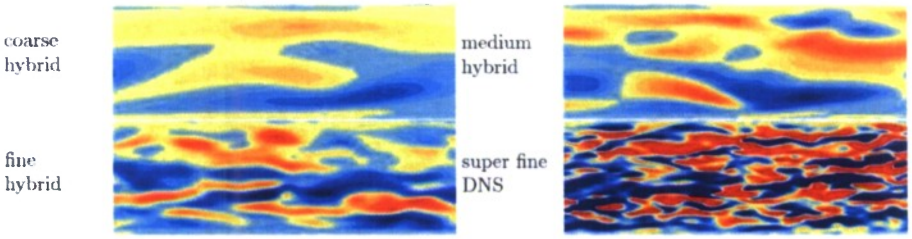

*Fig. 6.15: Square-duct flow at Re=10,000. Isocontours of streamwise vorticity,* $\omega_x = -10 \ldots 10$*, at* $z = 0$ *obtained from FBR with 1998 k-ω model and EASM and DNS.*

Isocontours of the streamwise wall vorticity,

$$\omega_x = \frac{\partial w}{\partial y} - \frac{\partial v}{\partial z}, \tag{6.1}$$

provide evidence of near wall streamwise vortical structures (Fig. 6.15). Again it can be seen how the number and intensity of the flow structures is reduced with decreasing grid resolution. Velocity profiles and profiles of turbulence kinetic energy (unresolved, resolved, and total) for the FBR are shown in Fig. 6.16. The medium and fine grid velocity profiles obtained with both, 1988 k-ω model with low-Reynolds number terms and 1998 k-ω model, almost match the DNS profile in the log-layer. The coarse grid velocity profiles approach or overshoot the RANS result near the center of the channel. The total turbulence kinetic energy, k, was computed by summation of the time-averaged unresolved turbulence kinetic energy, $k_u$, which attains its maximum near the wall, and the time-averaged resolved turbulence kinetic energy, $k_r$, which was computed from the unsteady velocity fluctuations and which attains its maximum further away from the wall and more towards the center of the channel. The total turbulence kinetic energy is higher for the 1988 k-ω model with low-Reynolds terms than for the 1998 k-ω model. With 1998 k-ω model the total turbulence kinetic energy shows the same near wall magnitude as for the DNS. As the grid resolution is reduced the location of the peak of the total turbulence kinetic energy moves away from the wall as the unresolved turbulence kinetic energy distribution begins to approach the RANS result.

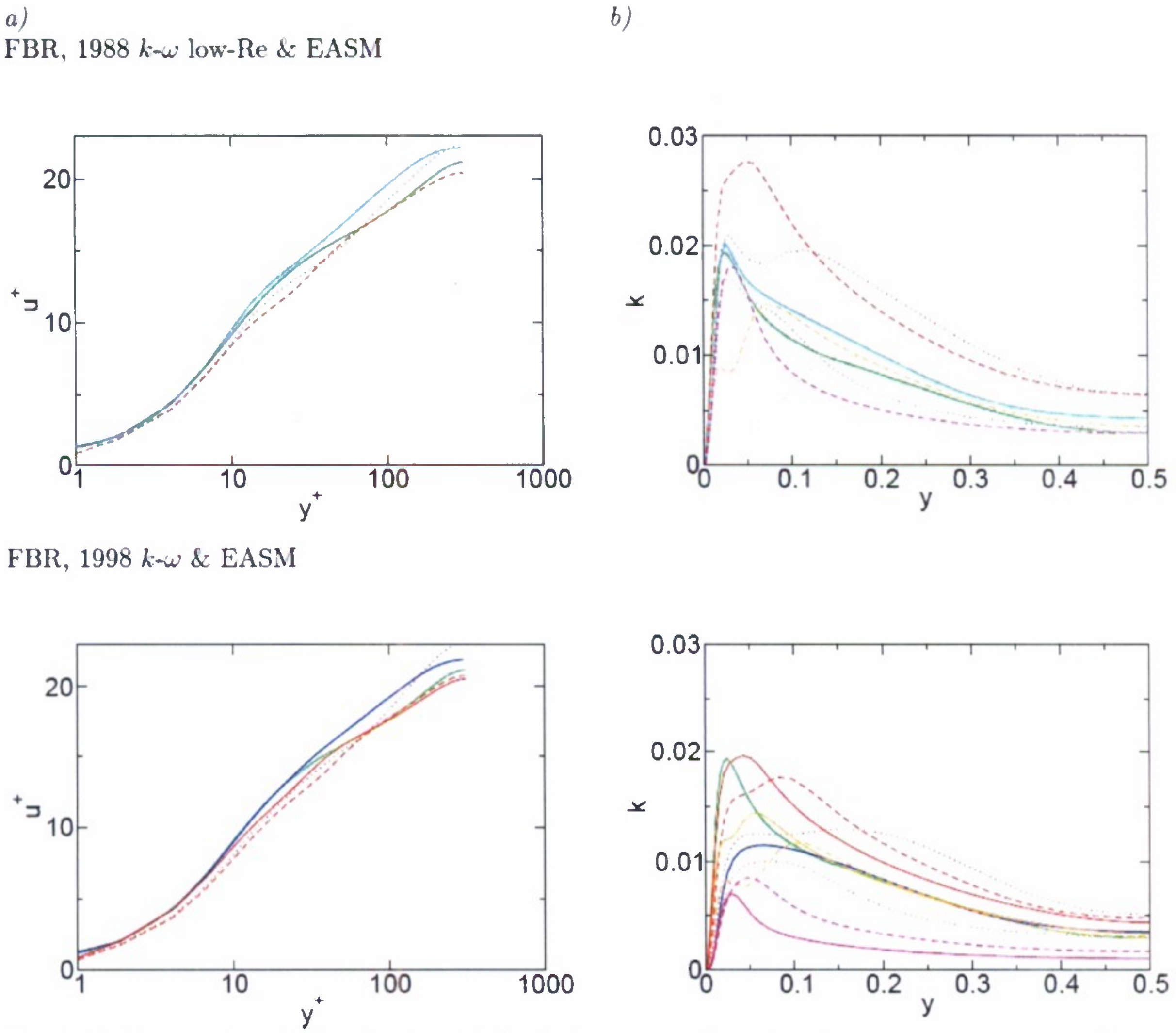

*Fig. 6.16: Square-duct flow at Re=10,000. Wall bisector profiles of a) streamwise velocity in wall units and b) total (red), resolved (orange) and unresolved (magenta) turbulence kinetic energy obtained from* ***FBR simulations****. Green lines: DNS; Cyan lines: RANS, 1988 k-ω low-Re and EASM; Blue lines: RANS, 1998 k-ω and EASM. Red lines: hybrid models as indicated. Dotted lines: Coarse grid; Dashed lines: Medium grid; Solid lines: Fine grid.*

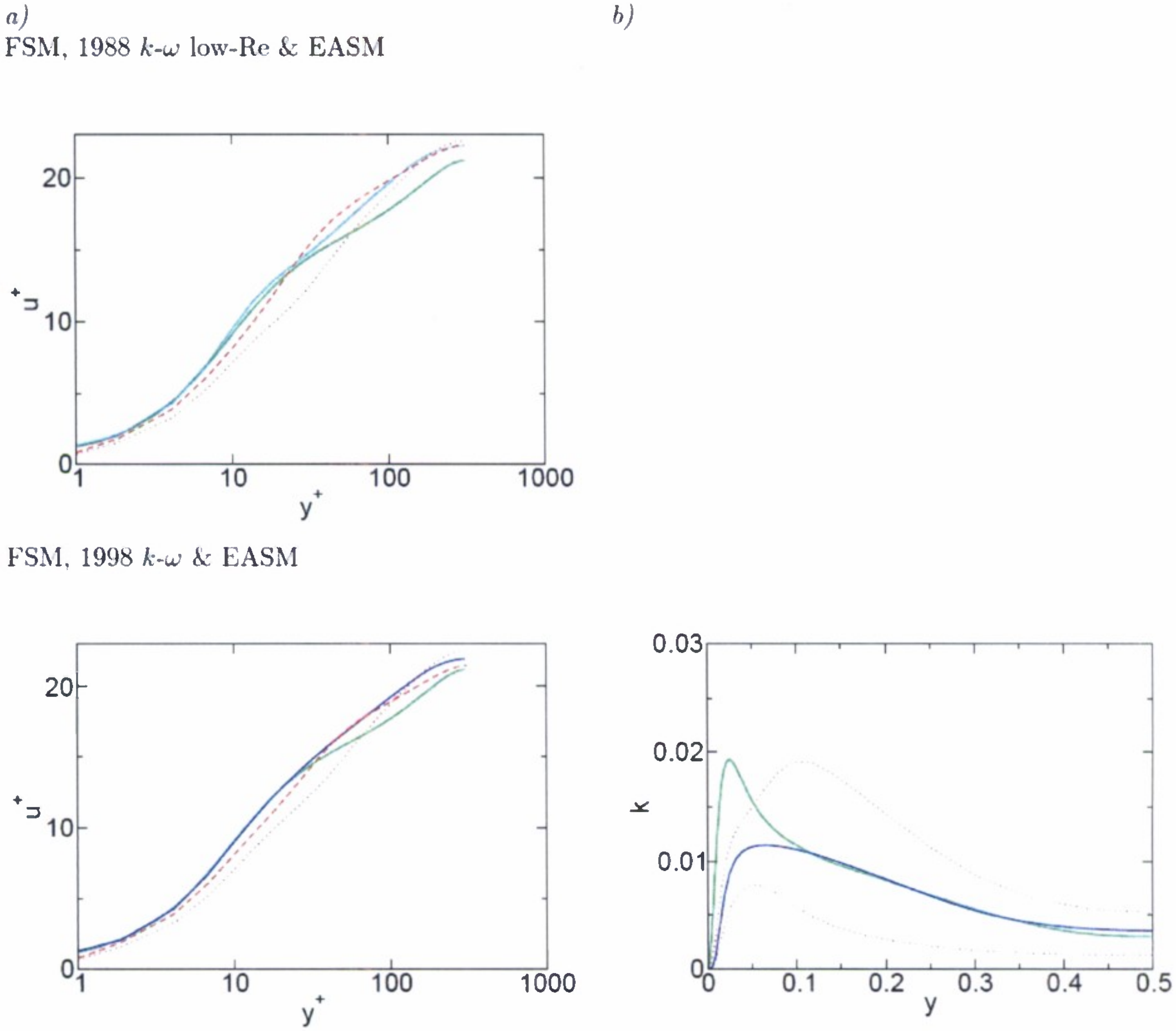

*Fig. 6.17: Square-duct flow at Re=10,000. Wall bisector profiles of a) streamwise velocity in wall units and b) total (red), resolved (orange) and unresolved (magenta) turbulence kinetic energy obtained from FSM simulations. Green lines: DNS; Cyan lines: RANS, 1988 k-ω low-Re and EASM; Blue lines: RANS, 1998 k-ω and EASM. Red lines: hybrid models as indicated. Dotted lines: Coarse grid; Dashed lines: Medium grid; Solid lines: Fine grid.*

Similar graphs for the FSM are provided in Fig. 6.17. Turbulence kinetic energy distributions are not shown for the FSM with 1988 k-ω model and low-Reynolds terms. Because the predicted bulk velocities were too high we decided against computing statistical quantities. The velocity profiles in wall units obtained from the FSM are closer to the RANS than to the DNS result as the grid resolution is increased from coarse to medium. Turbulence kinetic energy distributions are only available for the coarse grid FSM with 1998 k-ω model. Compared with the FBR result, the resolved turbulence kinetic energy and accordingly also the total turbulence kinetic energy are increased.

*a)* *b)*

FBR, 1988 *k*-*ω* low-Re & EASM

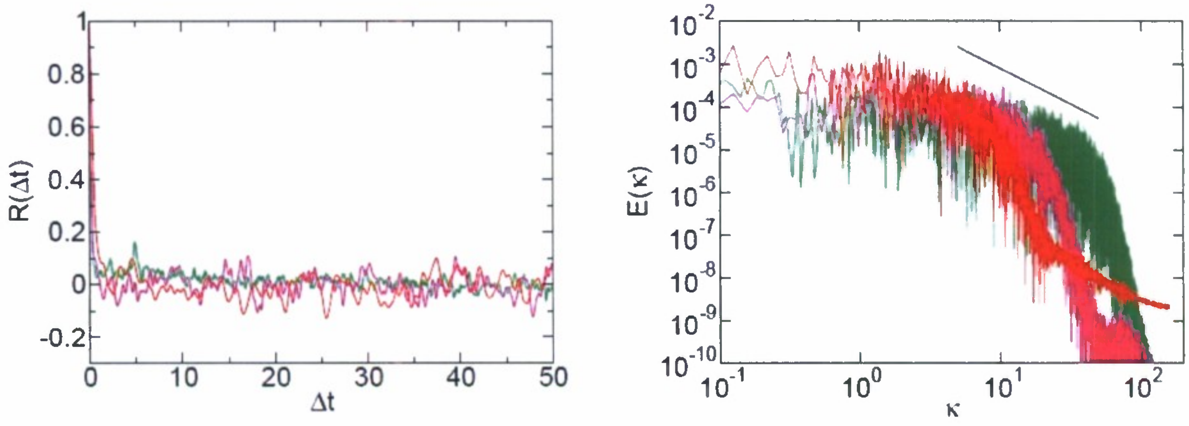

FBR, 1998 *k*-*ω* & EASM

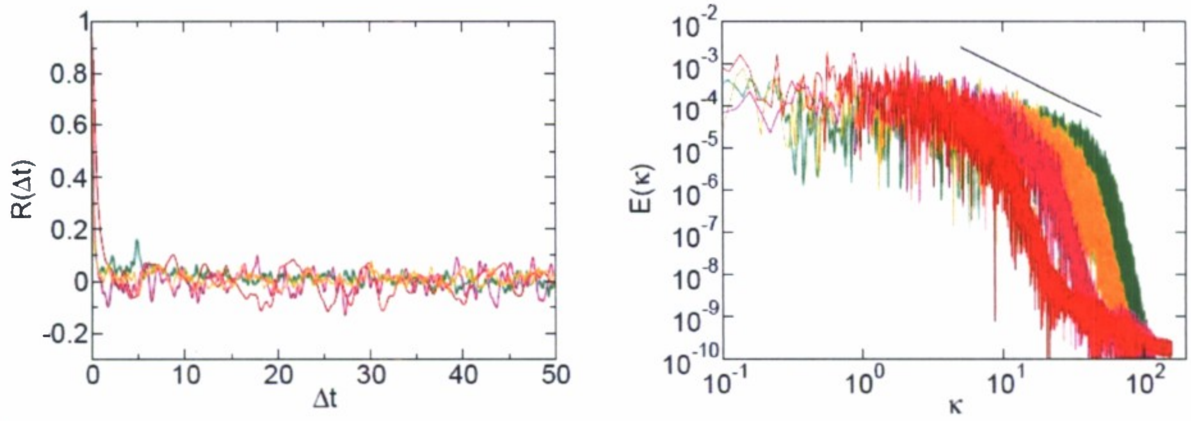

*Fig. 6.18: Square-duct flow at Re=10,000. a) Auto-correlations and b) frequency spectra of u-velocity perturbation at y = z = 0.5. Green lines: DNS; hybrid models as indicated: Red lines: Coarse grid; Magenta lines: Medium grid; Orange lines: Fine grid. Black lines: -5/3 slope of inertial sub-range.*

Auto-correlations and frequency spectra of the u-velocity perturbation, u'=u-U, at the mid-channel location are shown in Fig. 6.18. The data appears sufficiently de-correlated in time, leading to the conclusion that the streamwise domain extent was likely sufficient. However, the original intent was to identify extrema in the auto-correlations and correlate them with dominant wavelengths in the flow and then to investigate how well those waves are represented by the different hybrid RANS/LES approaches for different grid resolutions. Spectra are shown in Fig. 6.18b. The low frequency end of the spectra is not well resolved because of the limitation of the time intervals over which time-dependent data was recorded. Nevertheless, Fig. 6.18b indicates that the inertial sub-range is captured by the DNS and partially captured by the medium and fine grid hybrid simulations. Fig. 6.18b also shows how the wave number cutoff is shifted to lower wave-numbers as the grid resolution is reduced.

### 6.6 Rectangular Duct Flow

As a next step towards simulations of the entire diffuser we then computed the approach channel flow of the Stanford diffuser experiment [Cherry et al. 2008]. The approach channel flow Reynolds number based on channel height was 10,000 (or Re=15,381 based on hydraulic diameter). The computational domain (Fig. 6.19) had dimensions (length× height× width) of $6.66\times1\times3.33$ and a resolution of $64\times96\times96$ cells. The near wall grid line spacing in wall units was $\Delta x^+=62$, $\Delta y^+=0.89$, and $\Delta z^+=1.8\ldots33$ at the "long" wall (y=0) and $\Delta x^+=62$, $\Delta y^+=1.78\ldots7.1$, and $\Delta z^+=0.89$ at the "short" wall (z=0). Again, we first obtained RANS solutions with the 1998 k-ω model (Fig. 6.20). In agreement with the experiment a secondary flow is captured with the EASM (Fig. 6.21). The computed bulk velocities are 1.05 (Boussinesq approximation) and 1.08 (EASM).

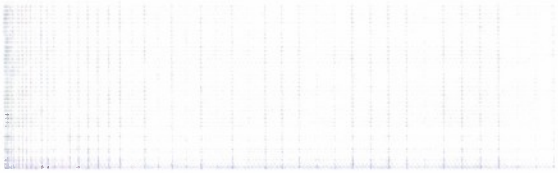

*Fig. 6.19: Computational grid for RANS and hybrid simulations of approach channel flow.*

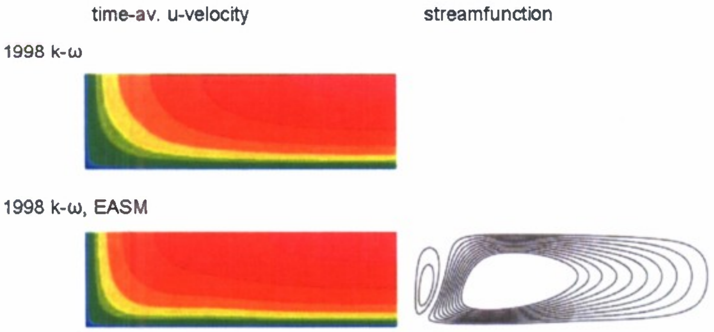

*Fig. 6.20: RANS results obtained with 1998 k-ω model. Isocontours of streamwise velocity ($0<u<1.8$, $\Delta u=0.1$) and streamfunction ($-0.001<\Psi<0.001$, $\Delta\Psi=0.0001$). Top: Boussinesq approximation, bottom: EASM.*

Instantaneous flow visualizations obtained from hybrid simulations with FSM and filter-based RANS (FBR) are shown in Fig. 6.22. We employed both approaches with and without "turbulence injection" in areas of vanishing model contribution. Slightly fewer structures are seen for the FBR again, indicating a larger model contribution. No difference is seen between the instantaneous flow fields with and without "turbulence injection".

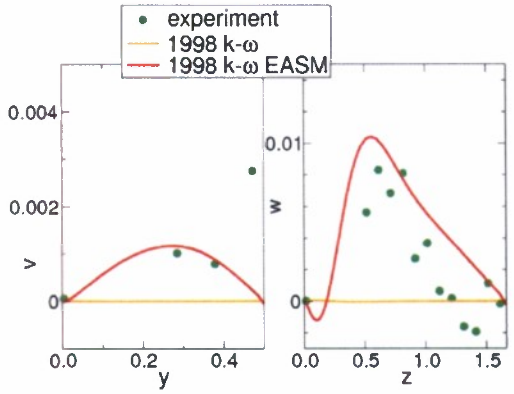

*Fig. 6.21: Velocity profiles at wall bisectors. Circles: Experiment by Cherry et al. [2008].*

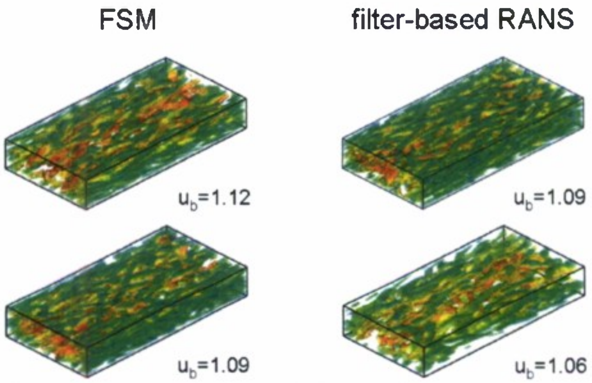

*Fig. 6.22: Hybrid simulations of approach channel flow without (top) and with "turbulence injection" (bottom). Isocontours of Q=0.1. Left: FSM and right: FBR.*

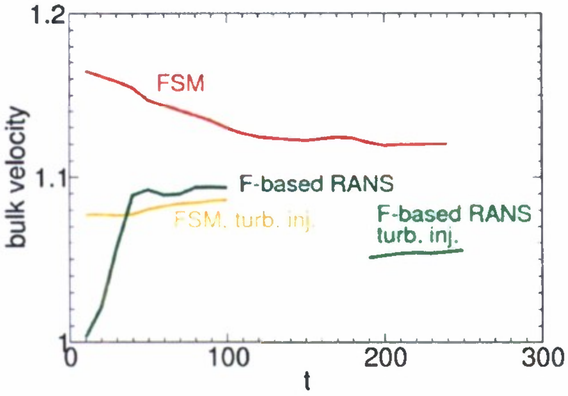

*Fig. 6.23: Approach channel flow bulk velocities.*

Histories of the computed bulk velocities are shown in Fig. 6.23. The bulk velocities are generally higher for the FSM when compared to the filter-based RANS. "Turbulence injection" lowers the bulk velocities possibly as the result of more and strengthened small scale structures.

# 7. DIFFUSER FLOW SIMULATIONS

We considered our hybrid RANS/LES duct flow simulations successful enough to begin simulations of a geometrically and physically more complex flow, the Stanford asymmetric diffuser for which measurements indicate a turbulent separated flow region [Cherry et al. 2008]. The diffuser inflow bulk Reynolds number based on hydraulic diameter is Re=15,380.

## 7.1 Computational Grid

The computational domain for our simulations was broken up into two sub-domains, one for the approach channel flow and one for the diffuser (Fig. 7.1). The approach channel flow sub-domain had a length×height×width ratio of 6.66×1×3.33 with 92×76×96 cells. The near wall grid line spacing in wall units was $\Delta x^+ = 42.8$, $\Delta y^+=0.556$, and $2.02 < \Delta z^+ < 36.3$ at $y=0$ and $\Delta x^+ = 42.8$, $1.07 < \Delta y^+ < 13.6$, and $\Delta z^+ = 1.01$ at $z = 0$. The diffuser opens up from a height× width ratio of 1×3.33 at $x = 0$ to 4×4 at $x = 15$. The inflow of the diffuser sub-domain was located at $x = -0.579$ to not fully suppress potential upstream effects of the diffuser flow on the approach channel flow. The outflow was located at $x = 45$. The diffuser grid had 268×76×96 cells. The near wall grid line spacing in wall units at the diffuser exit (Re=8,325) was $\Delta x^+ = 18.5$, $\Delta y^+ = 0.473$, and $0.548 < \Delta z^+ < 9.87$ at $y = 0$ and $\Delta x^+ = 18.5$, $0.946 < \Delta y^+ < 12.0$, and $\Delta z^+ = 0.274$ at $z = 0$. The total number of cells was 2.7 million.

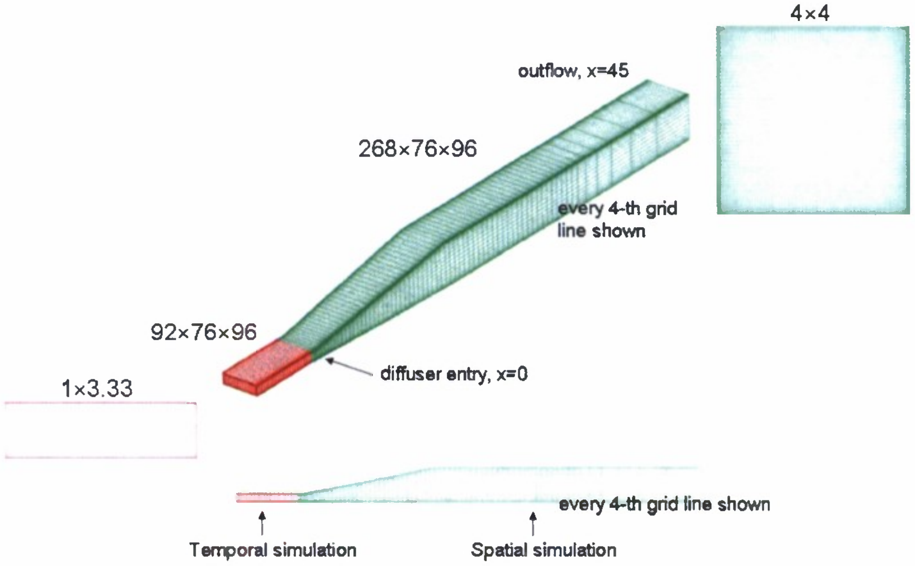

*Fig. 7.1: Computational grid for diffuser flow simulations.*

## 7.2 Simulation Results

We carried out several hybrid simulations [Gross and Fasel 2008b, 2010]. According to Margolin and Rider [2002] certain second-order-accurate upwind schemes have similar properties as standard LES sub-grid models. This motivated us to perform a simulation with second-order-accurate TVD scheme [Yee 1987] for the convective terms and a second-order-accurate discretization for the viscous terms. In addition, we performed one simulation with the same discretization as for the hybrid simulations (ninth-order-accurate discretization for the convective terms and fourth-order-accurate discretization for the viscous terms) but without turbulence model. The time step for all 4 simulations was Δt = 0.01. The simulations without turbulence model were advanced in time over 12000 time steps, which corresponds to approximately 7 diffuser flow-through times. For the FBR hybrid simulation with 1988 k-ω model, low-Reynolds number terms, and EASM time-averaging was initiated after 28000 time steps and stopped after 36000 time steps (approximately 5 flow-through times). For the FBR hybrid simulation with 1998 k-ω model and EASM the time-averaging was initiated after 12000 time steps and terminated after 36000 time steps (approximately 14 flow-through times).

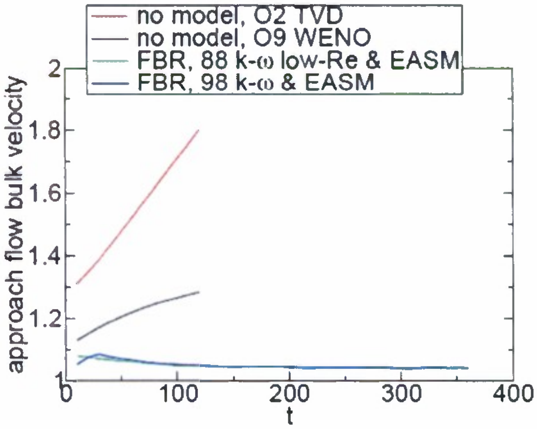

*Fig. 7.2: Diffuser approach flow bulk velocities.*

The time-histories of the approach flow bulk velocity are depicted in Fig. 7.2. With the second-order-accurate TVD scheme all unsteady flow structures in the approach flow are dampened out hinting at excessive numerical diffusion. This loss of unsteady flow structures reduces the amount of wall-normal mixing which increases the bulk velocity. Without correction of the channel flow volume force the bulk velocity increases beyond 1.8. The resulting diffuser inflow Reynolds number is larger than in the experiment. With the higher-order-accurate scheme and without turbulence model the approach flow bulk velocity asymptotically approaches a value in excess of 1.3. With the hybrid RANS/LES models the approach flow bulk velocity stabilizes near 1.04 which, considering the value of 1.03 for the square-duct flow DNS, is an acceptable value.

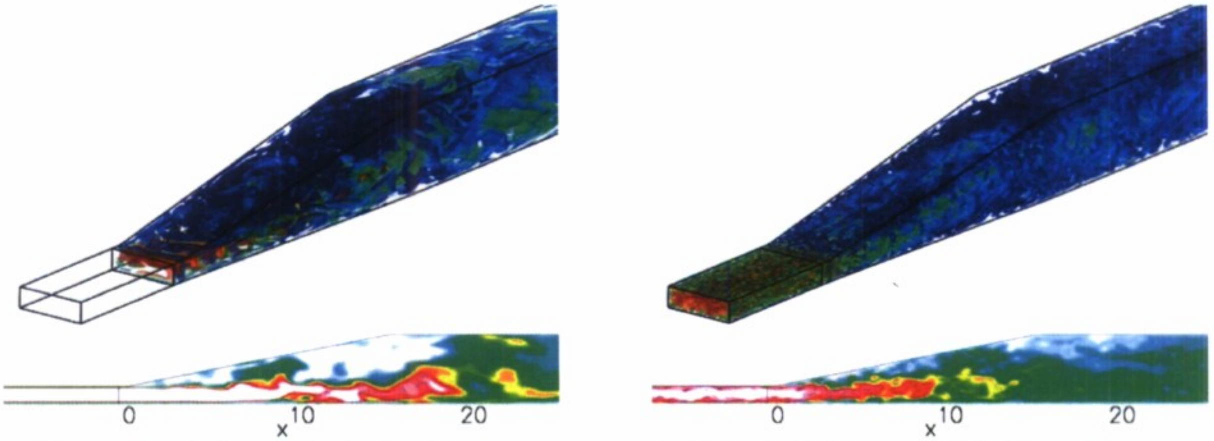

*a) O2 upwind scheme, no turbulence model*

*b) O9 upwind scheme, no turbulence model*

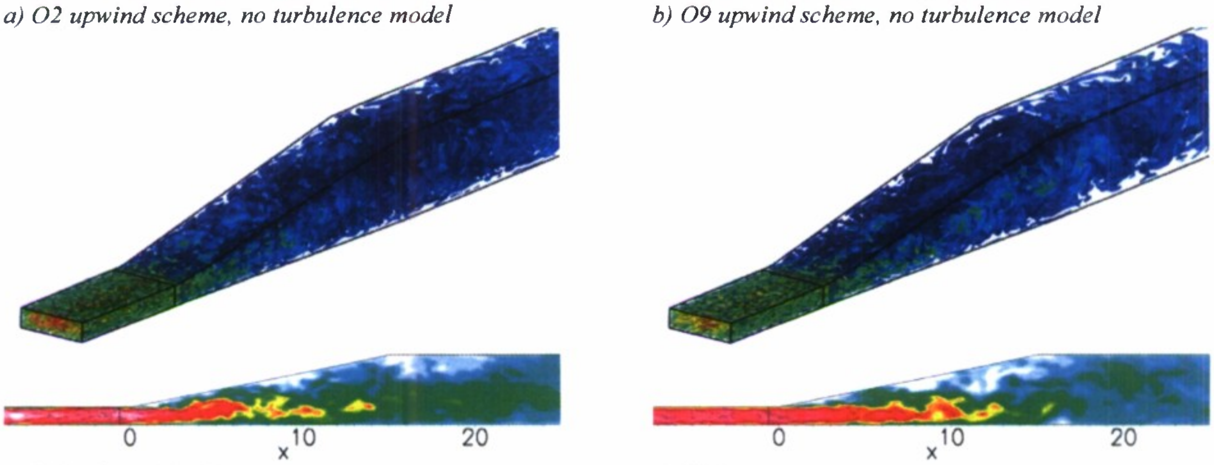

*c) Filter-based RANS*

*d) FSM*

*Fig. 7.3: Isosurfaces of $Q=0.01$ colored by u-velocity and isocontours of u-velocity (0...1.5) at $z=1.665$*

Instantaneous flow visualizations using the Q-criterion [Hunt 1988] are shown in Figs. 7.3 and 7.4. In all instances small-scale unsteady flow structures are seen in the diffuser ($0 < x < 15$) even for the diffusive second-order-accurate scheme where all unsteadiness in the approach channel flow is suppressed. This hints at a strong hydrodynamic instability mechanism that generates unsteady flow structures. Few large structures are seen for the diffusive second-order-accurate scheme while many small structures are seen for the ninth-order-accurate scheme without turbulence modeling.

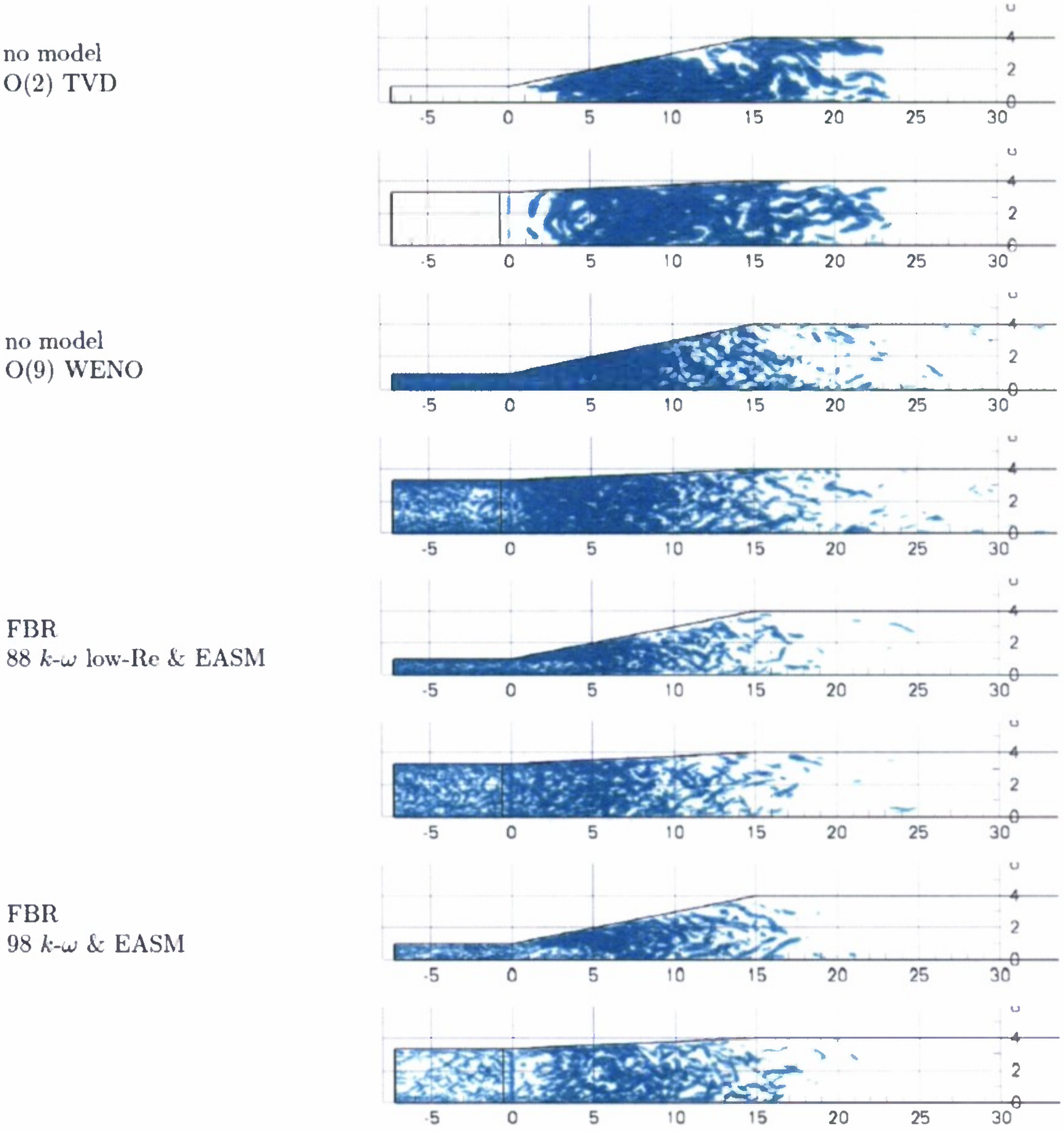

*Fig. 7.4: Diffuser at Re=15,380. Isosurfaces of Q = 1. Side views and top down views.*

Spanwise views of the time-averaged streamwise velocity (Fig. 7.5) provide information regarding the shape and extent of the separated flow region. In the experiments, volume data were obtained using magnetic resonance velocimetry [Cherry et al. 2008]. In the spanwise plane z=1.665 the flow appears to separate near x ≈ 7.5 and not at the diffuser inlet corner at x = 0. A similar behavior is observed for the FBR with 1988 k-ω model, low-Reynolds number terms, and EASM, although no conclusive statement can be made yet because the quality of the time-averages is poor. Because the diffuser geometry is asymmetric, data can only be averaged in time and time-averages take a long time to converge. For the FBR with 1998 k-ω model the flow appears to separate at the corner where the diffuser begins to open up, (x, z) = (0, 1.665), and to reattach near (x, z) = (7.5, 1.665). Also noteworthy is that the approach channel flow bulk velocity appears to be smaller in the experiment.

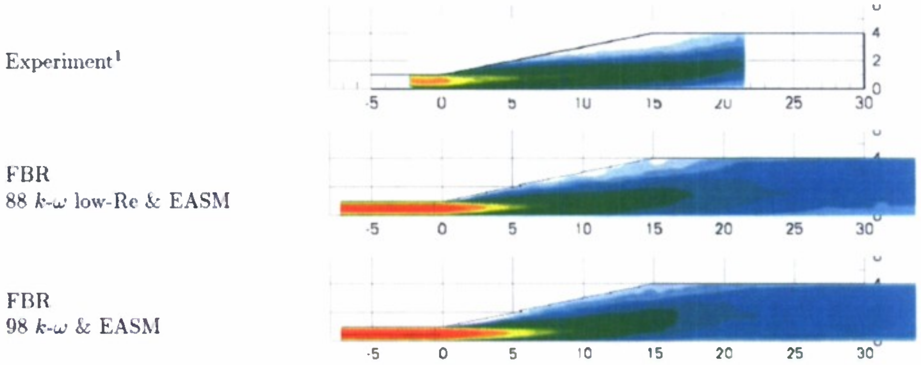

*Fig. 7.5: Diffuser at Re=15,380. Isocontours of time-averaged streamwise velocity at z = 1.665. Measurements by Cherry at al. [2008].*

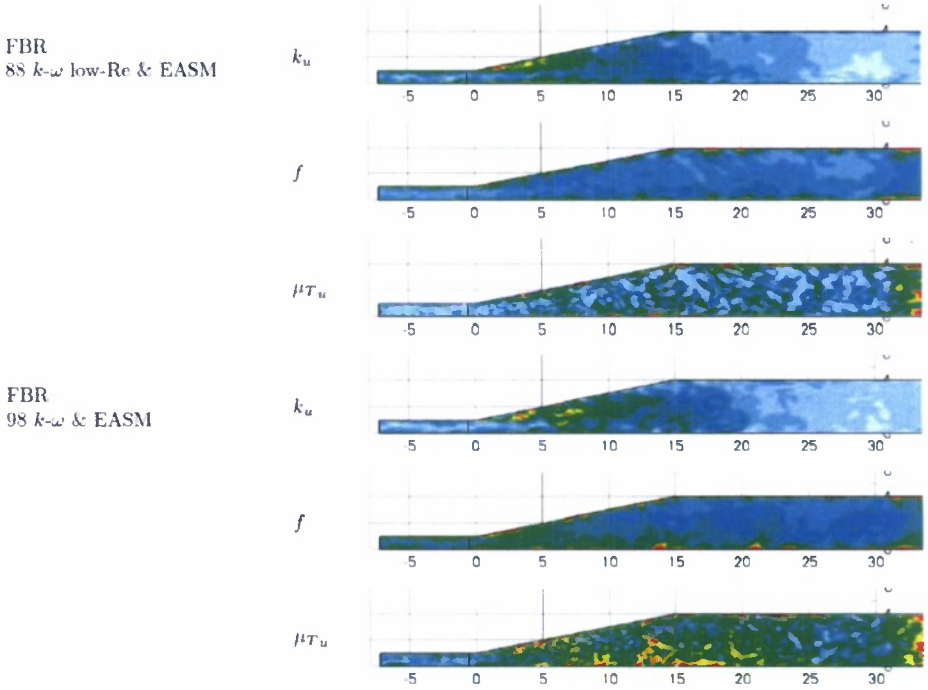

*Fig. 7.6: Diffuser at Re=15,380. Isocontours of instantaneous unresolved turbulence kinetic energy, $k_u$ =0 . . . 0.02, model contribution, $f$ = 0 . . 1, and unresolved eddy viscosity, $\mu_{Tu}$ = 0 . . . 10, at z = 1.665.*

Instantaneous visualizations in the spanwise plane, z = 1.665, for the two hybrid RANS/LES simulations are shown in Fig. 7.6. Unresolved turbulence kinetic energy, $k_u$, is produced in the separated shear layer and near the walls. Both, model contribution, f, and unresolved eddy viscosity, $\mu_{Tu}$, are larger for the 1998 k-ω model than for the 1988 k-ω model with low-Reynolds number terms.

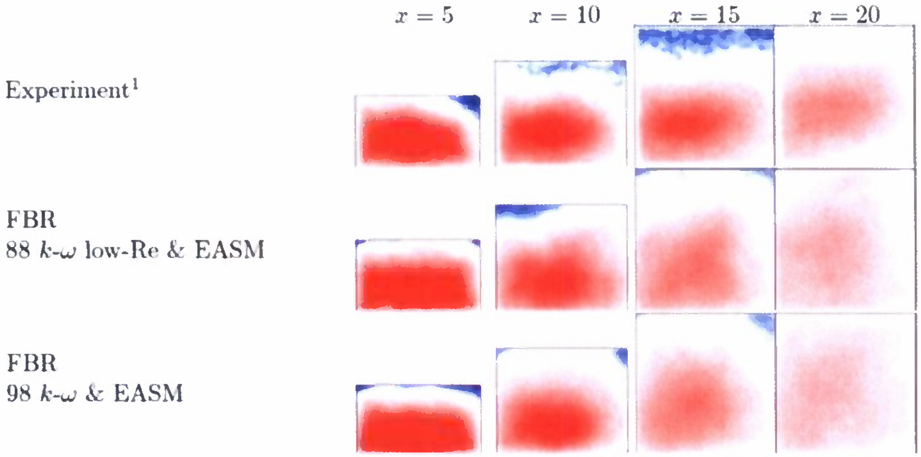

*Fig 7.7: Diffuser at Re=15,380. Cross-sectional views of streamwise velocity, u = −0.2 . . . 1.*

Cross-sectional views of streamwise velocity as shown in Fig. 7.7 provide information about the shape and extent of the separated flow region. In the experiment at x=5, the flow was separated from the top right-hand-side corner. At x=10 and x=15 the flow was separated from the entire top wall with the velocity maximum being slightly off to the left from mid-span. At x=20 the flow was fully attached. Although the quality of the time-averages obtained from our hybrid simulations is insufficient to allow for any final conclusions, the amount of flow separation appears under-predicted compared to the experiment.

# 8. SUMMARY AND CONCLUSIONS

## 8.1 3-D Separation Bubble on Flat Plate: Simulations and Experiments

We studied steady and unsteady 3-D separation bubbles on a flat plate using both direct numerical simulations (DNS) and water tunnel experiments. Separation was induced by a three-dimensional pressure distribution that was generated by an axisymmetric displacement body which was placed above the flat plate. Fundamental features that are documented in the literature for 3-D separated flows in general as well as for the flow over a hemisphere-cylinder in particular could be reproduced in our simulations and experiments. We investigated the effects of changes in the Reynolds number and the non-dimensional pressure distribution on the topology of the separation. The closed separation topologies that we identified all showed the same characteristic pattern of the skin friction lines at the upstream end of the separation bubble; i.e., the line of separation connects a saddle point of separation with a focus on either side of the symmetry plane. The foci are the roots of so-called "horn-vortices". We also showed that the topology at the downstream end of the separation bubble varies considerably for different flow conditions. In addition to the closed separation patterns, we also found an open separation topology that had not been documented before. The separation patterns that we identified for the unsteady cases exhibit a topology, which is equivalent to what is documented in the literature for the separated flow over a hemisphere-cylinder at low to intermediate angles of attack. In particular, we could detect lines of secondary separation. The fact that the characteristics of the separated flow over a hemisphere-cylinder could not always be reproduced in its entirety in our flat plate simulations, suggests that future research needs to address the effect of surface curvature. Our results also suggest that by adjusting the wall pressure distribution it is possible to at least qualitatively duplicate the flow behavior at a different Reynolds number. Our simulation results are in qualitative agreement with the accompanying water tunnel experiments. In particular, the topology of the bubble and the onset of bubble shedding at larger Reynolds numbers could be confirmed. We also noticed a relationship between Reynolds number, vortex shedding and the so-called "bubble breathing", as observed by Dogval and Kozlov [1994] for two-dimensional separation bubbles. The experiments thus provided guidance and validation for our simulations.

## 8.2 Simulations of Square-Duct Flow and Asymmetric Diffuser

We computed a square-duct flow at Re = 10,000, using Reynolds-averaged Navier-Stokes (RANS) and hybrid RANS/large eddy simulation (LES) turbulence modeling strategies [Gross and Fasel 2010]. We also carried out direct numerical simulations (DNS) of the same square-duct flow [Gross and Fasel 2009a]. Data from these DNS and DNS by Huser and Biringen [1993] served as a reference for our RANS and hybrid RANS/LES simulations. For our RANS and hybrid RANS/LES simulations we considered a modified version of the flow simulation methodology (FSM) [Speziale 1997, Fasel et al. 2002, Israel 2005, Zhang et al. 2000] and a modified version of the filter-based RANS (FBR) [Johansen et al. 2004] for which "backscatter" was introduced [Gross and Fasel 2009a,b]. The hybrid models were based on the 1988 k-ω model with low-Reynolds number terms and the 1998 k-ω model, both with explicit algebraic stress model (EASM) by Rumsey and Gatski [2001]. The FBR simulations were found to be in closer agreement with the reference data. In particular, reasonably accurate predictions of the bulk velocity and the streamwise velocity profiles in wall units were obtained. Encouraged by the channel flow results we carried out hybrid RANS/LES simulations of the Stanford diffuser experiment [Cherry et al. 2008] using the FBR model. Also, compared to the experiment, the amount of flow separation was underpredicted in our simulations. However, the quality of the time-averages was poor, since due to the asymmetric shape of the diffuser data could only be averaged in time. The mean flow was found to be strongly dependent on the underlying turbulence model. More simulations using longer time-averages and in particular also more investigations using different grid resolutions are required to further corroborate our hybrid results. In addition, our modified hybrid RANS/LES models require further attention and improvement.

# REFERENCES

Batten, P., Goldberg, U., and Chakravarthy, S., 2004, "Interfacing Statistical Turbulence Closures with Large-Eddy Simulation," AIAA Journal, Vol. 42, No. 3, pp. 485-492

Cantwell, B.K., 1981, "Organized Motion in Turbulent Flow," Annual Review of Fluid Mechanics, Vol. 13, pp. 457-515

Cherry, E.M., Elkins, C.J., and Eaton, J.K., 2008, "Geometric sensitivity of three-dimensional separated flows," Int. J. Heat and Fluid Flow, Vol. 29, No. 3, pp. 803-811

Dogval, A. V., Kozlov, V., and Michalke, A., 1994, "Laminar boundary layer separation: Instability and associated phenomena," Prog. Aero. Sciences

Fasel, H.F., Seidel, J., and Wernz, S., 2002, "A methodology for simulations of complex turbulent flows," Transactions of the ASME, Journal of Fluids Engineering, Vol. 124, No. 4, pp. 933-942

Gavrilakis, S., 1992, "Numerical simulation of low-Reynolds-number turbulent flow through a straight square-duct," Journal of Fluid Mechanics, Vol. 244, pp. 101-129

Gross, A., and Fasel, H., 2002, "High-Order WENO Schemes Based on the Roe Approximate Riemann Solver," AIAA-Paper AIAA-2002-2735

Gross, A., and Fasel, H.F., 2007, "Characteristic Ghost-Cell Boundary Condition," AIAA Journal, Vol. 45, No. 1, pp. 302-306

Gross, A., and Fasel, H., 2008a, "High-Order Accurate Numerical Method for Complex Flows," AIAA Journal, Vol. 46, No. 1, pp. 204-214

Gross, A., and Fasel, H., 2008b, "Numerical Investigation of Flow Separation in an Asymmetric Diffuser," AIAA-2008-671

Gross, A., and Fasel, H., 2009a, "Hybrid RANS/LES Simulations of Turbulent Channel Flow," AIAA-2009-1327

Gross, A., and Fasel, H., 2009b, "Active Flow Control for Airfoil at Low Reynolds Numbers," AIAA-Paper AIAA-2009-4275

Gross, A., and Fasel, H., 2010, "Hybrid RANS/LES Simulations of Turbulent Channel and Diffuser Flows," AIAA-Paper AIAA-2010-919, 48th AIAA Aerospace Sciences Meeting Including the New Horizons Forum and Aerospace Exposition, Orlando, Florida, Jan. 4-7, 2010

Hajjawi, M., Taylor, L., and Nichols, S., 2008, "Assessment Of Filtered-Based RANS Turbulence Model for Unsteady Separated Flow Prediction," AIAA-Paper AIAA-2008-670

Hamba, F., 2003, "A Hybrid RANS/LES Simulation of Turbulent Channel Flow," Theoretical and Computational Fluid Dynamics, Vol. 16, No. 5, pp. 387-403

Hsieh, T., and Wang, K. C., 1996, "Three-dimensional separated flow structure over a cylinder with a hemispherical cap", Journal of Fluid Mechanics, Vol. 324, pp. 83–108

Hunt, J.C.R., Wray, A.A., and Moin, P., 1988, "Eddies, stream, and convergence zones in turbulent flows," Report CTR-S88, Center For Turbulence Research, Stanford, CA

Huser, A., and Biringen, S., 1993, "Direct numerical simulation of turbulent flow in a square duct," Journal of Fluid Mechanics, Vol. 257, pp. 65-95

Huser, A., Biringen, S., and Hatay, F.F., 1994, "Direct simulation of turbulent flow in a square duct: Reynolds-stress budgets," Physics of Fluids, Vol. 6, No. 9, pp. 3144-3152

Israel, D.M., 2005, "A New Approach for Turbulent Simulations in Complex Geometries," PhD dissertation, The University of Arizona

Jacobi, R., Wernz, S., and Fasel, H.F., 2008, "Numerical Investigation of Localized Separation Induced by a Three-Dimensional Pressure Gradient", 38th AIAA Fluid Dynamics Conference and Exhibit, AIAA-Paper AIAA-2008-4056

Johansen, S.T., Wu, J., and Shyy, W., 2004, "Filter-based unsteady RANS computations," International Journal of Heat and Fluid Flow, Vol. 25, No. 1, pp. 10-21

Jones, W.P., Launder, B.E. 1972, "The Prediction of Laminarization with a Two-Equation Model of Turbulence," Int. J. of Heat and Mass Transfer, Vol. 15, pp. 301–314

Kenwright, D., and Haimes, R., 1997, "Vortex identification - applications in aerodynamics", IEEE Visualization 97

Kloker, M., Konzelmann, U., and Fasel, H.F., 1993, "Outflow Boundary Conditions for Spatial Navier-Stokes Simulations of Transition Boundary Layers", AIAA Journal, Vol. 3, No. 4, pp. 620-628

Lam, C.K.G., and Bremhorst, K.A. 1981, "Modified Form of k–ε Model for Predicting Wall Turbulence," ASME Journal of Fluids Engineering, Vol. 103, pp. 456–460

Lighthill, M. J., 1963, "Attachment and Separation in Three-Dimensional Flow", in Laminar Boundary Layers, ed. L. Rosenhead, chap. II, pp. 72–82

Madabhushi, R.K., and Vanka, S.P., 1991, "Large eddy simulation of turbulence-driven secondary flow in a square duct," Physics of Fluids A, Vol. 3, No. 11, pp. 2734-2745

Margolin, L.G., and Rider, W.J., 2002, "A rationale for implicit turbulence modeling," International Journal for Numerical Methods in Fluids, Vol. 39, pp. 821-841

Meitz, H.L., and Fasel, H.F., 2000, "A Compact-Difference Scheme for the Navier–Stokes Equations in Vorticity-Velocity Formulation," J. Comp. Phys., Vol. 157, pp. 371-403

Menter, F.R. 1992, "Influence of Freestream Values on k–ω Turbulence Model Predictions," AIAA Journal, Vol. 30, No. 6, pp. 1657–1659

Menter, F.R. 1994, "2-Equation eddy-viscosity turbulence models for engineering applications," AIAA Journal, Vol. 32, No. 8, pp. 1598-1605

Nikuradse, 1926, "Untersuchungen über die Geschwindigkeitsverteilung in turbulenten Strömungen," Dissertation Göttingen, VDI-Forschungsheft 281

Pauley, L. L., 1994, "Structure of local pressure-driven three-dimensional transient boundary-layer separation", AIAA Journal, Vol. 32, No. 5, pp. 997–1005

Perry, A., and Chong, M., 1986, "A series-expansion study of the Navier-Stokes equations with applications to three dimensional separation patterns", Journal of Fluid Mechanics, Vol. 173, pp. 207–223

Piomelli, U., Balaras, E., Pasinato, H., Squires, K.D., and Spalart, P.R., 2003, "The inner-outer layer interface in large-eddy simulations with wall-layer models", International Journal of Heat and Fluid Flow, Vol. 24, No. 4, pp. 538-550

Postl, D., 2005, "Numerical investigation of laminar separation control using vortex generator jets", PhD dissertation, University of Arizona

Rumsey, C.L., and Gatski, T.B., 2001, "Recent Turbulence Model Advances Applied to Multielement Airfoil Computations," Journal of Aircraft, Vol. 38, No. 5, pp. 904-910

Spalart, P.R., and Allmaras, S.R., 1992, "A One-Equation Turbulence Model for Aerodynamic Flows," AIAA-Paper, AIAA-92-0439

Speziale, C.G., 1997, "A Combined Large-Eddy Simulation and Time-Dependent RANS Capability for High-Speed Compressible Flows," Technical Report No. AM-97-022, Boston University

Tobak, M., and Peake, D.J., 1979, "Topology of two-dimensional and threedimensional separated flows", AIAA-Paper AIAA-79-1480

Tobak, M., and Peake, D.J., 1982, "Topology of Three-Dimensional Separated Flows," Annual Review of Fluid Mechanics, Vol. 14, pp. 61-85

von Kármán, T., 1948, "Progress in the Statistical Theory of Turbulence," Proc. Natl. Acad. Sci. USA, Vol. 34, No. 11, pp. 530-539

Wilcox, D.C., 2006, "Turbulence Modeling for CFD," Third Edition, DCW Industries.

Yee, H.C., 1987, "Upwind and Symmetric Shock-Capturing Schemes," NASA Technical Memorandum 89464, NASA Ames Research Center, Moffet Field, CA

Zhang, H.L., Bachman, C.R., and Fasel, H.F., 2000, "Application of a new methodology for simulations of complex turbulent flows," AIAA-Paper AIAA-2000-2535

Zedan, M. F., and Dalton, C, 1978, "Potential flow around axisymmetric bodies: Direct and inverse problems", AIAA Journal, Vol. 16, No. 3, 242–250

## PUBLICATIONS RESULTING FROM GRANT

Kremheller, A., and Fasel, H.F., 2010, "Water Tunnel Experiments on Three Dimensional Separation Bubbles on a Flat Plate," 40th AIAA Fluid Dynamics Conference and Exhibit, Chicago, IL, AIAA-Paper AIAA-2010-4738

Gross, A., and Fasel, H., 2010, "Hybrid RANS/LES Simulations of Turbulent Channel and Diffuser Flows," AIAA-Paper AIAA-2010-919, 48th AIAA Aerospace Sciences Meeting Including the New Horizons Forum and Aerospace Exposition, Orlando, Florida, Jan. 4-7, 2010

Jacobi, R., Gross, A., and Fasel, H.F., 2009, "Numerical Investigation of Three-Dimensional Separation in Internal and External Flows," HPCMP Users Group Conference 2009, June 15-18, 2009, San Diego, CA

Gross, A., and Fasel, H., 2009, "Hybrid RANS/LES Simulations of Turbulent Channel Flow," AIAA-Paper AIAA-2009-1327, 47th AIAA Aerospace Sciences Meeting including The New Horizons Forum and Aerospace Exposition, Orlando, Florida, Jan. 5-8, 2009

Gross, A., Jacobi, R., Wernz, S., and Fasel, H.F., 2008, "Numerical Investigation of Internal and External Three-Dimensional Flow Separation," HPCMP Users Group Conference 2008, July 14-17, 2008, Seattle, WA

Jacobi, R., Wernz, S., and Fasel, H.F., 2008, "Numerical Investigation of Localized Separation Induced by a Three-Dimensional Pressure Gradient", 38th AIAA Fluid Dynamics Conference and Exhibit, Seattle, WA, AIAA-Paper AIAA-2008-4056

Gross, A., and Fasel, H., 2008, "Numerical Investigation of Flow Separation in an Asymmetric Diffuser," AIAA-Paper AIAA-2008-671, 46th AIAA Aerospace Sciences Meeting and Exhibit, Reno, Nevada, Jan. 7-10, 2008